Conference Proceedings 2022

EPNC 2022

XXVII Symposium
Electromagnetic Phenomena
in Nonlinear Circuits

POLITECHNIKA POZNAŃSKA
POZNAN UNIVERSITY OF TECHNOLOGY

HELMUT SCHMIDT
UNIVERSITÄT
Universität der Bundeswehr Hamburg

XXVII Symposium
Electromagnetic Phenomena
in Nonlinear Circuits

June 28 – July 1, 2022
Hamburg, Germany

Editor

Univ.- Prof. Dr.-Ing. Christian Kreischer
Professorship for Electrical Machines and Drive Systems
Helmut Schmidt University/University of the Federal Armed Forces Hamburg
Holstenhofweg 85
22043 Hamburg, Germany
Email: christian.kreischer@hsu-hh.de
Website: https://epnc.put.poznan.pl

Co-Editors

Prof. Dr. hab. inż. Andrzej Demenko
Division of Mechatronics and Electrical Machines
Poznan University of Technology
3a Piotrowo street
60-965 Poznan
Email: andrzej.demenko@put.poznan.pl

Dr. hab. inż. Wojciech Pietrowski
Head of Division of Mechatronics and Electrical Machines
Poznan University of Technology
3a Piotrowo street
60-965 Poznan
Email: wojciech.pietrowski@put.poznan.pl

A team from the Poznan University of Technology and members of EPNC Editorial Board were involved in the review process of the papers.

DOI: https://doi.org/10.24405/14897

Print: Helmut Schmidt University/University of the Federal Armed Forces Hamburg, 2022

Cover photo: Elbphilharmonie und Hafencity mit Baukränen / Timo Sommer

PREFACE

Dear colleagues, authors and readers,

the 27th EPNC at the Helmut Schmidt University / University of the Federal Armed Forces in Hamburg is over and we look back on a conference with exciting contributions and discussions.

The conference was divided into 4 thematic blocks: electrical machines, applications, calculations and measurements as well as simulations and modeling.

The contributions presented can be found in this anthology. The main focus of the publications were topics on electrical machines, magnetic materials and the corresponding calculation and analysis methods. It turns out that the method of differential evolution is becoming more and more popular for optimization issues.

I hope you enjoy studying the articles and I would be happy if this results in new research ideas and a further scientific exchange.

Best regards
Christian Kreischer

P.S.: The following photo gives you an impression about the conference

Conference participants

International Steering Committee

A. Belahcen	Aalto University	Finland
G. Cieślar	Medical University of Silesia	Poland
A. Demenko, Chairman	Poznan University of Technology	Poland
H. De Gersem	Technische Universität Darmstadt	Germany
I. Doležel	Academy of Sciences of the Czech Republic	Czech Republic
S. Exnowski	University of Applied Sciences	Germany
M. Frivaldsky	University of Žilina	Slovakia
J. Gieras*	UTC Aerospace Systems	Rockford IL, USA
K. Hameyer	RWTH Aachen University	Germany
M. Kaźmierkowski*	Warsaw University of Technology	Poland
C. Kreischer	University of the Federal Armed Forces	Germany
S. Kulig	TU Dortmund University	Germany
Y. Le Menach	University of Lille	France
J.-Ph. Lecointe	Artois University	France
S. Nabeta*	University of Sao Paulo	Brazil
E. Napieralska-Juszczak	Artois University	France
A. Nicolet*	Aix-Marseille University	France
L. Nowak	Poznan University of Technology	Poland
M. Petrun	Maribor University	Slovenia
M. Repetto	Politecnico di Torino	Italy
R. Sabariego	KU Leuven	Belgium
I. Slabu	RWTH Aachen University	Germany
S. Stipetić	Zagreb University	Croatia
D. Stryczewska	Lublin University of Technology	Poland
J. Sykulski	University of Southampton	United Kingdom
A. Szucs	University of Pécs	Hungary
S. Wiak	Technical University of Lodz	Poland
M. Zagirnyak	Kremenchuk Mykhailo Ostrohradskyi National University	Ukraine
K. Zawirski*	Poznan University of Technology	Poland
W. Pietrowski, Secretary	Poznan Univ of Technology	Poland

** Corresponding member*

International Organising Committee

Christian Kreischer	Conference Chair
Johannes Liebrich	Technical and Advisory Committee
Lucas Steinacker	Technical and Advisory Committee

CONTENT

CONFERENCE CONTRIBUTIONS

ANALYSIS OF LOSSES IN THE HIGH-SPEED PMBLDC MOTOR WITH OPEN SLOT STATOR CORE MADE OF AMORPHOUS SOFT MAGNETIC MATERIAL

Marek Hreczka, Roman Kolano, Aleksandra Kolano-Burian, Wojciech Burlikowski*, Janusz Hetmanczyk*

Institute of Non-Ferrous Metals, Gliwice 44-100, Poland, e-mail: Marek.Hreczka@imn.lukasiewicz.gov.pl
*Faculty of Electrical Engineering, Silesian University of Technology, Gliwice 44-100, Poland, e-mail: wojciech.burlikowski@polsl.pl

***Abstract* – A modified structure of the stator core will be used in a PM BLDC prototype machines to compare their properties for different magnetic materials. It enables application of concentrated stator windings. The analysis is focused on comparison between core losses in machine with classical stator core made of Fe-Si and a new one made of modern METGLAS material. Both analytical and numerical (FEM) methods will be used to verify the design performance. Results will be verified experimentally in the final paper.**

I. INTRODUCTION

In the last two decades applications of amorphous soft magnetic materials (ASMMs) have been very popular in power electronics, particularly in various transducers, sensors etc. mainly because of energy savings. Its application in distribution transformers, leading to the replacement of the conventional cores made of the Si steel with the amorphous cores, resulted in the reduction of no-load losses by more than a half [1][2]. Increasing requirements on efficiency in electric motors led to their application also in this area, despite very difficult machining, confirming the benefits from using these novel materials also in the stators and rotors of the electric machines, both induction and PMBLDC [3][4][10][12].

II. STATOR STRUCTURE

A promising area of the application of the ASMMs are the permanent magnet brushless direct current (PMBLDC) motors, which are characterized by relatively simple construction, high power density, low moment of inertia, and good dynamic properties. They have smaller dimensions and simpler control systems than the induction motors and are very reliable. Because of these advantages, the PMBLDC motors are particularly suitable for application in high-speed drives [10][12] .

In the previous papers a half-open slots were used in the design of the stator core [4]. A very high rotational speed (up to 60000 rpm) of the rotor made it difficult to separate losses in the core from the overall losses. Therefore, a new design of the motor was proposed, very much different from typical designs of high speed motor [8]. The design is similar to spindle motors used in HDD [6][7]. Due to decreased mechanical speed (up to 8000 rpm) the mechanical losses are much lower and it should be easier to perform the comparison between the iron losses in the standard core made of Fe-Si steel sheets and the new one made of ASMMs as they have the same stator design (Fig.1).

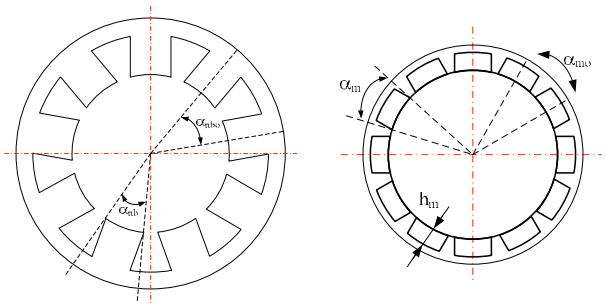

Fig.1. PMBLDC stator and rotor prototype design

The frequency of the magnetic field in the machine core is high due to six pole pairs of the rotor. In theory the losses in ASMM cores are even 10 times smaller than in Fe-Si steel cores, but due to complicated heat and mechanical treatment this ratio decreases [9]. The main aim of the paper is to verify this for the proposed prototype machine.

III. PROTOTYPE NUMERICAL TESTS

The two prototype machines have been designed. Main data are shown in Table I. The only difference between the two prototypes is the material of the stator core, ASMM or Fe-Si.

TABLE I
MACHINE DATA

DIMENSIONS	
Axial length	80 mm
Air gap length (with sleeve)	2,2 mm

STATOR	
Number of slots	9
Outer diameter	104 mm
Inner diameter	50,4 mm
Angle of the pole (α_{nb})	30°
Stator core	ASMM (Metglas) or Fe-Si
Phase resistance	13,8 [mΩ]
Turns per phase	15
Wire diameter (Cu)	3,5 [mm]

ROTOR	
Number of poles	12
Permanent magnet	Bonded NdFeB (B_r=1,244 [T], H_c=-947 [kA/m])
Outer diameter (without magnets)	40 mm
Magnet height (h_m)	3 mm
Magnet angle (α_m)	25°
Rotor yoke	Steel 45

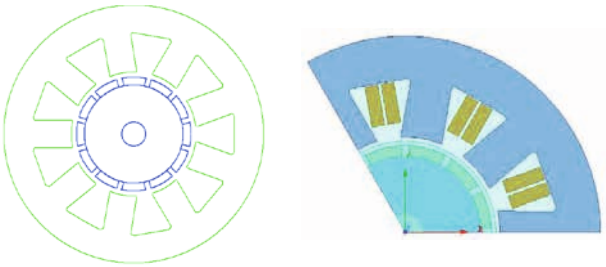

Fig.2. Simulation models in ANSYS Electronics Desktop environment (RMxpert - left, 2D FEM)

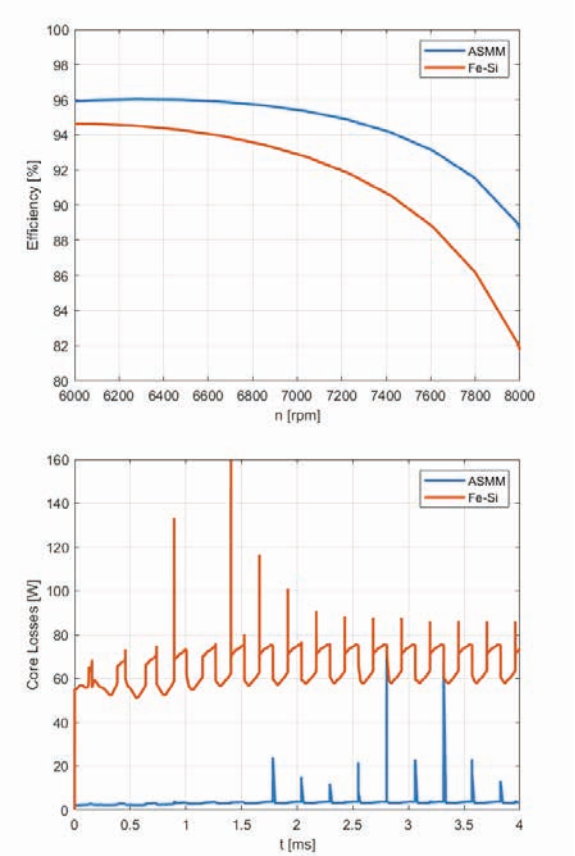

Fig.3. Results of simulation: efficiency vs. rotational speed and core losses for n=6525 [rpm]

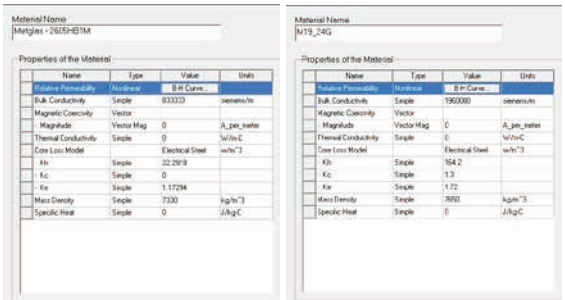

Fig.4. Materials parameters used in simulation: Metglas and Fe-Si

Initial tests have been performed using analytical (RMxpert) and 2D FEM (Maxwell) models in ANSYS Electronics Desktop shown in (Fig.2) [11]. 3D FEM (Maxwell) model has been created but due to very long computation time it has not been simulated. Both FEM models cover 1/3 of the cross section of the machine. Control algorithm of the supply is based on classical 120 degree ($2/3\pi$ rad) conduction mode with idealised lossless converter for 50 [V] DC bus voltage [5]. Results of numerical tests are shown in (Fig.3). It clearly shows the better performance of the ASMM machine compared to Fe-Si one, which was expected.

IV. CONCLUSIONS

Results obtained using analytical and FEM models prove the advantage of the stator made of METGLAS over the classical one made of Fe-Si steel sheets. It must be underlined that the models use idealised material parameters from Maxwell material library (Fig.4) [12].

In the final paper the experimental verification of the simulation results will be provided. The procedure similar to the one described in [4] will be used. Modified parameters of the magnetic materials after heat and mechanical processing will be used in simulation to verify their actual values.

REFERENCES

[1]. R. Hasegawa, "Applications of amorphous magnetic alloys," Mater. Sci. Eng., A, vols. 375-377, pp. 90-97, Jul. 2004.
[2]. R. Kolano, A. Kolano-Burian, M. Polak, and J. Szynowski, "Application of rapidly quenched soft magnetic materials in energy-saving electric equipment," IEEE Trans. Magn., vol. 50, no. 4, Apr. 2014, Art. ID 2004804.
[3]. J. M. Silveyra, P. Xu, V. Keylin, V. DeGeorge, A. Leary, and M. E. McHenry, "Amorphous and nanocomposite materials for energy-efficient electric motors," J. Electron. Mater., vol. 45, no. 1, pp. 219-225, 2015.
[4]. Kolano R., Kolano-Burian A., Krykowski K.s, Hetmanczyk J., Hreczka M., Marcin P., and Jan Szynowski J., "Amorphous Soft Magnetic Core for the Stator of the High-Speed PMBLDC Motor With Half-Open Slots," IEEE TRANSACTIONS ON MAGNETICS, VOL. 52, NO. 6, JUNE 2016.
[5]. Wach P. Dynamics and Control of Electrical Drives, Springer, 2021.
[6]. United States Patent, No. 5,804,904, Date of Patent: Sep. 8, 1998, Samsung Electronics Co., Ltd.
[7]. Dahaman Ishak, Z. Q. Zhu , and David Howe, "Permanent-Magnet Brushless Machines With Unequal Tooth Widths and Similar Slot and Pole Numbers", IEEE TRANSACTIONS ON INDUSTRY APPLICATIONS, VOL. 41, NO. 2, MARCH/APRIL 2005.
[8]. Tianran He, Ziqiang Zhu , Fred Eastham, Yu Wang, Hong Bin, Di Wu, Liming Gong and Jintao Chen, "Permanent Magnet Machines for High-Speed Applications" World Electr. Veh. J. 2022, 13, https://doi.org/10.3390/wevj13010018.
[9]. N. Ertugrul, R. Hasegawa, W. L. Soong, J. Gayler, S. Kloeden, and S. Kahourzade, "A Novel Tapered Rotating Electrical Machine Topology Utilizing Cut Amorphous Magnetic Material" IEEE Trans. Magn., (2015).
[10]. https://www.hitachi.com/rd/sc/story/amorphous/index.html
[11]. ANSYS Electromagnetics Suite 2021 R1, Manual - © ANSYS, Inc.
[12]. Yu,W.; Hua,W.; Zhang, Z. "High-Frequency Core Loss Analysis of High-Speed Flux-Switching Permanent Magnet Machines". Electronics 2021, 10, 1076. https://doi.org/10.3390/electronics10091076.

DETERMINATION OF THE LIMITS OF DIFFERENT QUASISTATIC MODELS BASED ON MULTI-DOMAINS APPLICATION

Houssein Taha[1], Yvonnick Le Menach[1], Thomas Henneron[1], Zuqi Tang[1], Jean-Pierre Ducreux[2]
[1]Univ. Lille, Arts et Metiers Institute of Technology, Centrale Lille, Junia, ULR2697-L2EP, F-59000 Lille, France
[2]EDF R&D, ERMES, 7 Boulevard Gaspard Monge, 91120 Palaiseau, France

***Abstract*—The electro-quasistatic (EQS) model is widely used to study the coupled resistive-capacitive effects while the magneto-quasistatic (MQS) model is used to describe the coupled resistive-inductive effects at low frequencies. However, in the intermediate frequency range, the Darwin model is preferred. In this work, we are interested in specifying the limits of these models by considering an academic example.**

***Index Terms*—Capacitive-inductive-resistive effects, electromagnetic fields, quasistatic models.**

I. Introduction

A magnetic field computation starts with an a priori choice of simplifying assumptions in order to use suitable formulations. The choice of low and high frequencies is quite simple, but it is not obvious when the increase in frequencies generates coupled phenomena (RL, RC or RLC), the skin effect, and wave propagation. Under these conditions, it is necessary to establish a classification of the different quasi-static models based mainly on theoretical considerations [1]. From the size of the domain and the conductors, and according to the frequency, it is possible to define criteria [2] which will guide the user in choosing the appropriate formulation to model the problem. The motivation of our work is to investigate the limits of the different quasistatic models by considering a simple academic example.

II. Quasistatic Models

In the following, the different quasistatic models, namely, EQS, MQS, and Darwin models are briefly presented.

A. Electro-quasistatic model

For an EQS problem, the induced current density represented by the term $j\omega\mathbf{B}$ is neglected. Then, the electric field $\mathbf{E}$ is a curl-free field. Consequently, an electric scalar potential (ESP) φ such $\mathbf{E} = -\mathbf{grad}\ \varphi$ is introduced. In the frequency domain, the potential formulation to be solved for the EQS reads

$$\text{div}\ (\sigma\mathbf{grad}\ \varphi + j\omega\varepsilon\mathbf{grad}\ \varphi) = 0 \tag{1}$$

where σ is the electric conductivity, and ε is the electric permittivity.

B. Magneto-quasistatic model

For a MQS problem, the displacement current represented by the term $j\omega\mathbf{D}$ is neglected. Then, the $\mathbf{A}/\varphi$ potential formulation of MQS model without entering the gauge conditions reads

$$\mathbf{curl}\,(\nu\mathbf{curl}\,\mathbf{A}) + \sigma(j\omega\mathbf{A} + \mathbf{grad}\,\varphi) = \mathbf{0}, \tag{2}$$

$$\text{div}\ (\sigma(j\omega\mathbf{A} + \mathbf{grad}\,\varphi)) = 0 \tag{3}$$

where $\mathbf{A}$ is the magnetic vector potenial (MVP) and ν is the magnetic reluctivity.

C. Darwin model

For the Darwin model, the assumption of a quasistatic electromagnetic field model enables the elimination of the rotational parts of the displacement currents, $\omega^2\varepsilon\mathbf{A}$, in Ampère's law. In particular, this term is responsible for the radiation effects. Then, the classical $\mathbf{A}/\varphi$ potential formulation for the Darwin model [3] reads

$$\mathbf{curl}\,(\nu\mathbf{curl}\,\mathbf{A}) + \sigma(j\omega\mathbf{A} + \mathbf{grad}\,\varphi) + j\omega\varepsilon\mathbf{grad}\,\varphi = \mathbf{0}, \tag{4}$$

$$\text{div}\ (\sigma(j\omega\mathbf{A} + \mathbf{grad}\,\varphi) + j\omega\varepsilon\mathbf{grad}\,\varphi) = 0. \tag{5}$$

It should be mentioned here that the ESP φ is defined in the whole domain. Applying the FE method, the MVP $\mathbf{A}$ is discretized with the edge elements and the ESP φ with the nodal elements which introduce an asymmetric matrix. In addition, the resultant matrix is not gauged. The uniqueness of $\mathbf{A}$ can be ensured by adding the Coulomb gauge or the tree gauge.

III. Definition of Criteria for Choice Model

The physical phenomena presented in an electromagnetic system are of three types: resistive, inductive, and capacitive. Also, the choice is dictated by the presence or not as well as the preponderance over others of these phenomena in the device considered. As reported in [2], it is possible to define three parameters and choose our model according to them:

$$k_1 = \left(\frac{\lambda}{L}\right)^2,\ k_2 = \left(\frac{\delta}{L}\right)^2 \text{and}\ k_3 = \left(\frac{\lambda}{\delta}\right)^2 \tag{6}$$

with δ the skin thickness, L the domain size, and λ the wavelength. The term k_1 allows us to specify if the propagation effects are dominant or negligible, k_2 allows to determine if the size of the system allows the current to flow with or without skin effect and k_3 allows to know which one of conduction or displacement currents is negligible, or equivalent, with respect to each other.

shape is considered in Fig. 1 which is made of aluminum, having a section of 3.14 mm^2 and a length of 100 mm, and an airbox encloses the electric cable. To model the capacitive effects in this application, a ground plane is fixed below the conductor.

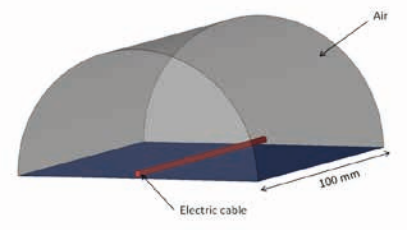

Fig. 1: The geometry of the electric cable.

To take into account the skin effects in the conductor for high frequencies, the geometry is spatially discretized by a tetrahedral mesh composed of 1 453 084 elements including 246 180 nodes and 1 700 862 edges. A sinusoidal voltage is applied between the terminals of the winding marked in red as shown in Fig. 1. The problem is solved in the frequency domain for 1 Hz - 1 GHz. For the EQS model, the number of DoFs is 245 330 and the computational time for one frequency takes about 1.5 minutes for each frequency, while it takes in MQS model about 20 minutes for 1 908 095 DoFs. The computational time using Darwin formulation takes about 30 minutes for 1 941 395 DoFs.

A. Evolution of the impedance vs frequency

The evolution of the impedance as a function of the frequency is presented in Fig. 2. For all models, Z corresponds to the DC resistance of the conductor with $R_{DC} = 0.32\ \Omega$ when the frequency tends to zero. When the frequency increases, due

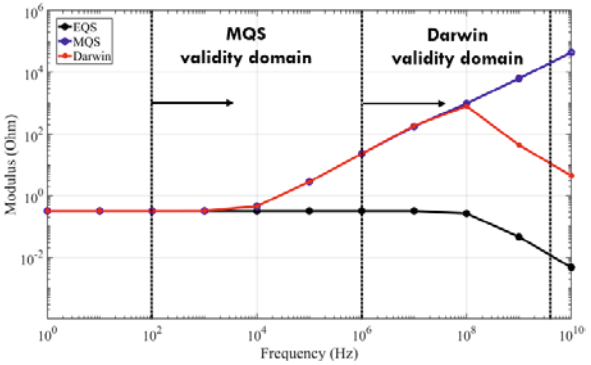

Fig. 2: Modulus of impedance vs frequency.

to the skin effect appearing in the conductor, the value of the resistance of the conductor increases. This effect is not taken into account with the EQS model. For $f < 10$ MHz, when the capacitive effect is negligible, the MQS and Darwin models give a similar evolution of the impedance. For $f > 10$ MHz, the influence of the capacitive effects appears on the evolution of the impedance for both the EQS and Darwin models.

by the previous application, a diagram specifies the various electromagnetic domains, namely, static, quasistatic, and *Full-wave* as shown in Fig. 3.

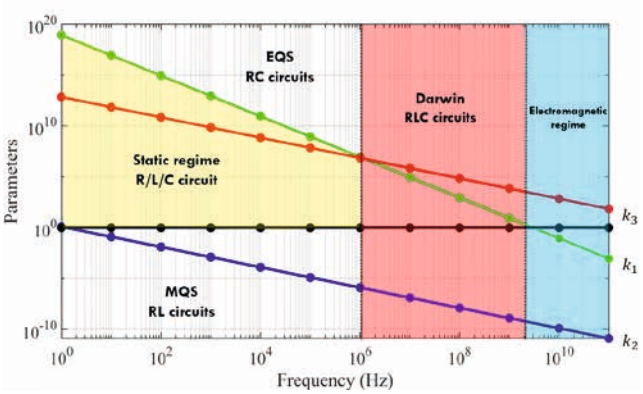

Fig. 3: Diagram specifying the different electromagnetic models.

The electric and magnetic fields are decoupled for $k_1 >> 1$. In this zone, the electrokinetic, electrostatic, and magnetostatic models can be used to compute the resistance R, capacitance C, and inductance L, respectively. On the other hand, the k_2 and k_3 indicators which determine the necessity to use the MQS and EQS models, show an almost parallel variation, indicating that when k_2 moves away from 1, the MQS model cannot be adopted, and when k_3 approaches to 1, the EQS model can be adopted. Besides, as seen in Fig. 2, by comparing the impedance obtained by EQS and Darwin models, the Darwin model should be applied when $k_1 \sim k_3$. In addition, around 3 GHz, the Darwin model reaches its limit. In this case, the study of the full Maxwell model is necessary since the wave propagation should be taken into account.

V. Conclusion

In the intermediate frequency range, in particular, around the resonant frequency, the Darwin model should be adopted to handle the coupled capacitive-inductive effects. Furthermore, the EQS model can be used as an indicator to know when the Darwin model should be applied since the computational time with EQS model is much faster than the others. However, the limit of the Darwin is not trivial to determine in the case of complex applications.

References

[1] F. Rapetti and G. Rousseaux, "On quasi-static models hidden in maxwell's equations," *Applied Numerical Mathematics*, vol. 79, pp. 92–106, 2014. Workshop on Numerical Electromagnetics and Industrial Applications (NELIA 2011).

[2] C. Geuzaine, "Numerical techniques for forward modelling," 2012.

[3] S. Koch, H. Schneider, and T. Weiland, "A low-frequency approximation to the Maxwell equations simultaneously considering inductive and capacitive phenomena," *IEEE Transactions on Magnetics*, vol. 48, pp. 511–514, Feb. 2012.

PARAMETER IDENTIFICATION OF A NONLINEAR D-Q DYNAMIC MODEL OF A IPMSM BY USING A FEM MODE

Mitja Garmut and Martin Petrun

University of Maribor, FERI, Institute of Power Engineering
Koroška cesta 46, SI-2000 Maribor, Slovenia, e-mail: mitja.garmut@um.si, martin.petrun@um.si

***Abstract* – Small highly saturated IPMSM show a very nonlinear behaviour. This kind of machines are mostly controlled with a closed loop cascade control, which requires a d-q two-axis dynamic model with constant concentrated parameters to calculate the control parameters. This paper presents the identification of a complete current- and rotor position-dependent d-q dynamic model, which is derived by using a FEM simulation. The machine's constant parameters are determined by reduction of the model's complexity step by step, furthermore the effect of different terms is presented.**

I. INTRODUCTION

Small Interior Permanent Magnet Synchronous Machines (IPMSM) with high power to wight ratios behave very nonlinear, due to the slotting effect, permanent magnets, cross coupling, cross saturation, and very saturated magnetically nonlinear iron core [1]. As this kind of machines are generally controlled by using linear closed loop cascade control, which is based on the constant concentrated parameter d-q dynamic model, such parameters have to be identified [2]. Different complexity levels with different dependencies of the d-q models were evaluated by [3, 4].

The discussed effects can be simulated by using a Finite Element Method (FEM) model, which is the basis for developing a complete current- and position-dependent nonlinear d-q dynamic model. This model is composed of various terms and dependencies, which model different nonlinear effects. By evaluating each of those effects, we analysed which of the terms and dependencies have a significant influence on the machine's behaviour.

The aim of this paper is a systematic analysis of discussed influences through step-by-step reduction of the complexity of the dynamic model. This gives a deeper understanding of the behaviour of the machine and highlights the effects that are important to consider for the given task. The paper gives a guide how to determine adequate constant concentrated parameters of the d-q dynamic model which are needed for the control development.

II. IPMSM D-Q DYNAMIC MODEL

The complete current- and position-dependent d-q dynamic model is presented in this section. The motion is described by (1):

$$J\frac{\mathrm{d}^2\theta_\mathrm{m}}{\mathrm{d}t^2} = t_\mathrm{e} - t_\mathrm{l} - k_\mathrm{f}\frac{\mathrm{d}\theta_\mathrm{m}}{\mathrm{d}t} - k_\mathrm{C}\left(\frac{\mathrm{d}\theta_\mathrm{m}}{\mathrm{d}t}\right)^2, \qquad (1)$$

where J is the moment of inertia, k_f is the viscous friction coefficient, k_C is the ventilation coefficient, t_e is the electromagnetic torque and t_l is the load torque. The electrical position (angle) is $\theta = p\,\theta_\mathrm{m}$, where p is the number of pole pairs and θ_m is the mechanical rotor position. The voltage-balance equation in the d-q reference frame is given by (2):

$$\begin{bmatrix} u_\mathrm{d} \\ u_\mathrm{q} \end{bmatrix} = R\begin{bmatrix} i_\mathrm{d} \\ i_\mathrm{q} \end{bmatrix} + \left[\boldsymbol{L}_\mathrm{i}\right]\frac{\mathrm{d}}{\mathrm{d}t}\begin{bmatrix} i_\mathrm{d} \\ i_\mathrm{q} \end{bmatrix} + \frac{\mathrm{d}\theta}{\mathrm{d}t}\left(\left[\frac{\partial\boldsymbol{\Psi}}{\partial\theta}\right] + \left[\boldsymbol{L}_\mathrm{a}\right]\begin{bmatrix} i_\mathrm{d} \\ i_\mathrm{q} \end{bmatrix} + \begin{bmatrix} 0 \\ \Psi_\mathrm{md} \end{bmatrix}\right),$$

$$\left[\boldsymbol{L}_\mathrm{i}\right] = \begin{bmatrix} L_\mathrm{d,i} & L_\mathrm{dq,i} \\ L_\mathrm{qd,i} & L_\mathrm{q,i} \end{bmatrix} = \begin{bmatrix} \frac{\partial\Psi_\mathrm{d}}{\partial i_\mathrm{d}} & \frac{\partial\Psi_\mathrm{d}}{\partial i_\mathrm{q}} \\ \frac{\partial\Psi_\mathrm{q}}{\partial i_\mathrm{d}} & \frac{\partial\Psi_\mathrm{q}}{\partial i_\mathrm{q}} \end{bmatrix}, \qquad (2)$$

$$\left[\boldsymbol{L}_\mathrm{a}\right] = \begin{bmatrix} 0 & -L_\mathrm{q,a} \\ L_\mathrm{d,a} & 0 \end{bmatrix} = \begin{bmatrix} 0 & \frac{-\Psi_\mathrm{q}}{i_\mathrm{q}} \\ \frac{\Psi_\mathrm{d}}{i_\mathrm{d}} & 0 \end{bmatrix}, \left[\frac{\partial\boldsymbol{\Psi}}{\partial\theta}\right] = \begin{bmatrix} \frac{\partial\Psi_\mathrm{d}}{\partial\theta} \\ \frac{\partial\Psi_\mathrm{q}}{\partial\theta} \end{bmatrix},$$

where i_d, i_q and u_d, u_q are the d-q reference frame voltages and currents, R is the resistance and Ψ_q is the flux linkage in the q-axis due to the current excitation. The total flux linkage in the d-axis is defined as $\Psi_\mathrm{d}^* = \Psi_\mathrm{d} + \Psi_\mathrm{md}$, where Ψ_d is the flux linkage in the d-axis due to the current excitation and Ψ_md is the flux linkage in the d - axis due to the permanent magnet. $L_\mathrm{d,i}$, $L_\mathrm{dq,i}$, $L_\mathrm{qd,i}$, $L_\mathrm{q,i}$ are the incremental inductances, as denoted by the subscript i, where $L_\mathrm{d,a}$, $L_\mathrm{q,a}$ are the apparent inductances denoted by subscript a.

A. Parameter identification

Three different parameter dependencies were constructed. Firstly, the dependencies of Ψ_d^*, Ψ_q and t_e from the position θ and the currents i_d, i_q were obtained by using an automated process. A MATLAB-script was used to simulate different i_d and i_q combinations in a 2D transient FEM model using Ansys Maxwell 2D. The torque was defined as t_e (i_d, i_q, θ) and stored in a LookUp Table (LUT). The data was processed, and the matrices of incremental inductances $\boldsymbol{L}_\mathrm{i}$ (i_d, i_q, θ), apparent inductances $\boldsymbol{L}_\mathrm{a}$ (i_d, i_q, θ), and position derivatives of the flux linkages $\frac{\partial\boldsymbol{\Psi}}{\partial\theta}$ (i_d, i_q, θ) were calculated. Figure 1 shows $L_\mathrm{d,i}$ (i_d, i_q, θ), where i_q is 1.5 p.u. In the 2nd step the average values of Ψ_d^* and Ψ_q and t_e in respect to θ were considered to calculate current dependent incremental inductances $\boldsymbol{L}_\mathrm{i}$ (i_d, i_q), and apparent inductances $\boldsymbol{L}_\mathrm{a}$ (i_d, i_q). The torque was defined as t_e (i_d, i_q,). With this data 2D and 3D LUTs were generated. In the 3rd approach $\boldsymbol{L}_\mathrm{i}$ and $\boldsymbol{L}_\mathrm{a}$ were considered current and position independent, whereas t_e was calculated according to (3):

$$t_\mathrm{e} = \frac{3}{2}p\left(\Psi_\mathrm{md}i_\mathrm{q} + i_\mathrm{d}i_\mathrm{q}\left(L_\mathrm{d,i} - L_\mathrm{q,i}\right)\right). \qquad (3)$$

All other input values as R, J, k_f, k_C, p and Ψ_md were assumed constant. A time stepping simulation was constructed in Simulink, by using (1), (2) (in the 3rd approach (3) was used) and LUTs with the inputs u_d, u_q, t_l. The outputs were i_d, i_q, t_e, θ and the phase currents i_a, i_b, i_c.

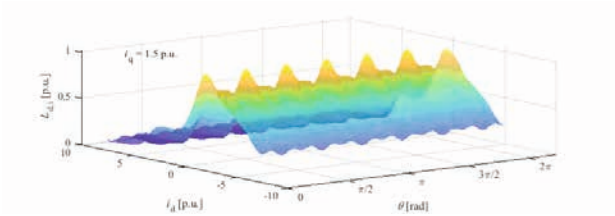

Fig. 1: The incremental inductance $L_{d,i}(i_d, i_q, \theta)$ in dependence from the electrical position θ and the d-axis current i_d, when $i_q = 1.5$ p.u.

B. Overview of reduced models

Table 1 shows all 5 models that were considered and their specific features, terms, and dependencies.

Table 1: Model complexity reduction from model 1 to model 5

Model	Model features
M1	Defined by (1) and (2), parameters are dependent from θ, i_d and i_q. Torque LUT - t_e (i_d, i_q, θ).
M2	M1 neglecting cross-coupling terms, i.e. $L_{dq,i}$ (i_d, i_q, θ). and $L_{qd,i}$ (i_d, i_q, θ).
M3	M2 neglecting term $\frac{\partial \Psi}{\partial \theta}$ (i_d, i_q, θ).
M4	M3 neglecting θ dependence. Torque LUT - t_e (i_d, i_q,).
M5	M4 with constant parameters (no dependencies included) that are operation point specific. Torque is defined by (3).

To evaluate the parameters of M5 the motion equation (1) of the models was neglected and the electrical speed $\omega = \frac{d\theta}{dt}$ was chosen as an input for all 5 models. A representative operation point (OP) was defined by u_d, u_q and ω, referred to as OP1. All models were analysed in this OP. The constant parameters for M5 were obtained by using the steady-state i_d and i_q of M4.

III. RESULTS

A comparison of the 5 models is presented first. Figure 2 shows one period of the current in phase a i_a, corresponding rms and total harmonic distortion (THD) value in steady state, compared to the FEM calculated i_a. Table 2 shows the relative difference of t_e compared to FEM calculated t_e for all models.

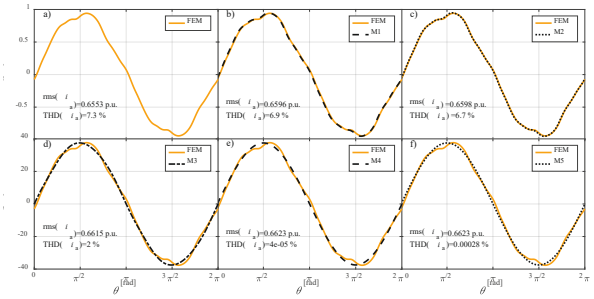

Fig. 2:Phase currents i_a, corresponding rms and THD values in steady state for all 5 models and the FEM model at a OP1 defined by u_d, u_q and ω

Table 2: Relative difference between avg(t_e) from FEM and avg(t_e) for all models at a OP1 defined by u_d, u_q and ω

$\frac{t_{e,M} - t_{e,FEM}}{t_{e,FEM}}$ [%]	FEM	M1	M2	M3	M4	M5
	0	.32	.27	.52	.68	4.1

When comparing i_a and t_e of M1 to the FEM simulation, we observed a very good agreement. The significant change happened when reducing M2 to M3, which is presented in Fig. 2 c) and d) and in Table 2. The values of rms(i_a) and THD(i_a) in Fig. 2 e) and f) show that M4 and M5 give almost identical outputs. The reason is that the steady-state i_d, i_q of M4 is used for obtaining the parameters of M5. The t_e in M4 and M5 presented in Table 2 were different, as in M4 the 2D LUT is used and in M5 equation (3) to calculate the t_e.

Further, the dynamic behaviour of the M1 and M5 were compared. The OPs were defined by u_d, u_q, t_l and the load torque t_l, that was changed from 1 p.u. to 1.4 p.u. at time 0.4 ms. The dynamic behaviour of the i_d, i_q, t_e and ω were analysed, as show in figure 3.

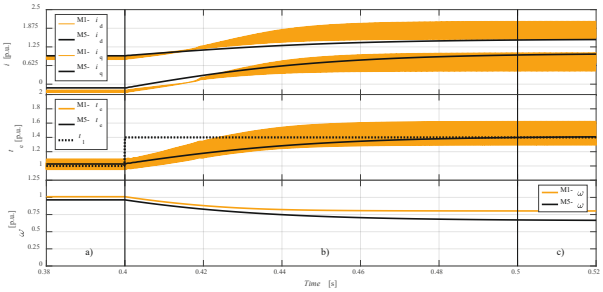

Fig. 3: Dynamic behaviour of M1 and M5 shown by change of i_d, i_q, t_e and ω

Fig.3 a) shows the 1st steady-state OP, with the values i_d, i_q, t_e and ω of M1 and M5 that settle at comparable values, as the first OP was close to OP1. When changing t_l the models show comparable dynamic behaviour, as presented in Fig.3 b). The observed values in the 2nd steady-state OP, shown in Fig.3 c) show a bigger deviation between the models. As the operation moves away from OP1, the difference gets bigger, as all the nonlinear behaviour of M1 cannot be captured by the constant parameters of M5.

IV. CONCLUSIONS

It was shown how to construct complete d-q dynamic model of the machine, which includes all nonlinear effects. Different models with varying complexities were developed, which can be used for different types of applications, that require different levels of accuracy, for example control strategy testing. M1 behaved very similar to the FEM simulation. M4 and M5 showed the biggest deviation from the FEM simulation at OP1. When the machine is not operating in OP1 the deviation between M1 and M5 is getting bigger, but the overall behaviour of M5 resembles the dynamic behaviour of M1. It can be concluded that M5 can be used for control development when adequate OP is chosen for the identification of model's parameters. In the extended paper the model development will be presented in more detail and the results will include a detailed comparison between the models.

REFERENCES

[1] M. Hadžiselimović, G. Štumberger, B. Štumberger, and I. Zagradišnik, "Magnetically nonlinear dynamic model of synchronous motor with permanent magnets," *Journal of Magnetism and Magnetic Materials,* vol. 316, no. 2, pp. e257-e260, 2007-09-01 2007,

[2] M. S. Rafaq and J.-W. Jung, "A Comprehensive Review of State-of-the-Art Parameter Estimation Techniques for Permanent Magnet Synchronous Motors in Wide Speed Range," *IEEE Transactions on Industrial Informatics,* vol. 16, no. 7, pp. 4747-4758, 2020-07-01 2020,

[3] A. Pouramin, R. Dutta, M. F. Rahman, and D. Xiao, "Inductances of a fractional-slot concentrated-winding interior PM synchronous machine considering effects of saturation and cross magnetization," *IEEE Energy Conversion Congress and Exposition (ECCE)*, 2015-09-01 2015: IEEE

[4] B. Stumberger, G. Stumberger, D. Dolinar, A. Hamler, and M. Trlep, "Evaluation of saturation and cross-magnetization effects in interior permanent-magnet synchronous motor," *IEEE Transactions on Industry Applications,* vol. 39, no. 5, pp. 1264-1271, 2003.

NONLINEAR CONDUCTIVITY APPLICATION TO ELECTRIC FIELD GRADING IN THE REINFORCED INSULATION OF CABLE JOINTS

Nebojsa Raicevic, Ana Vuckovic, Mirjana Peric, Svetlana Raicevic*

University of Nis, Faculty of Electronic Engineering, Department of Theoretical Electrical Engineering
Aleksandra Medvedeva 14, 18000 Nis, Serbia, e-mail: nebojsa.raicevic@elfak.ni.ac.rs

*Post of Serbia, Information technologies, Electronic communications and development
Vozda Karadjordja 13, 18101 Nis, Serbia, e-mail: cecarai@icloud.com

Abstract **- The Intensity of the electric field and the connection temperature of two power cables are important parameters that affect the performance and reliability of the cable network. Non-uniform distributions lead to rapid aging of cable accessories.**
In order to accurately detect the local temperature, temperature rise of the cable joint and to overcome the shortcomings of traditional methods of electric and thermal circuit, HBEM (Hybrid Boundary Elements Method) was applied.
The distribution of electro-thermal fields in power cable joints, using HBEM is presented in this paper. Temperature dependent insulation is selected.

I. THEORETICAL BACKGROUND

The places where cables are connected are called cable joints. The power cable joint is the weakest component and it prone to overheating and burning. The joint internal temperature is about 90 °C with normal load, while the temperature can reach 250 °C if the cable is maximally loaded. Increasing the temperature of the cable insulation affects the increase of the tangential component of the electric field in the so-called "hot spot", which leads to easier breakdown of the dielectric. It is necessary to calculate them because 78% of breakdowns happen in these places.

The basic idea of the theory is that an arbitrary shaped boundary between two media, having different thermal conductivities, can be replaced by finite system of equivalent volumetric heat sources (EHS). The EHS are located at the boundary between the two areas. It is possible, using condition that the heat flux density on boundary is continuous, to form a system of linear equations, where heat sources on segments are unknown. By solving this system, the unknown sources can be determined.

A similar procedure can be applied to the calculation of the electric field [1, 2]. The problem must be solved with coupled thermal and electrical equations [3] by using HBEM (Hybrid Boundary Elements Method), developed at our department.

Coupling relationship and analogies between electro-magnetic and thermal field can be applied. The steady-state heat conduction equations of cable joints can be described as:

$$\nabla\cdot(\lambda\nabla T)+Q_v=0;\ -\lambda\frac{\partial T}{\partial n}\Big|I_1=(h-h_r)(T_f-T_a);\ -\lambda\frac{\partial T}{\partial n}\Big|I_2=0,\ (1)$$

where n represents the boundary normal vectors, λ is the thermal conductivity, T is the temperature, Q_v is the heat source per unit volume, h is the coefficient of convective heat transfer, h_r is the coefficient of radiation heat transfer.

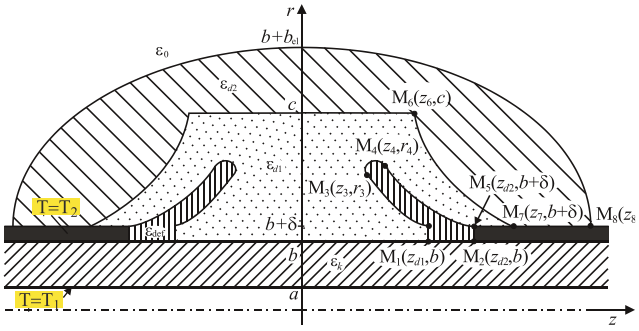

Fig.1. Axial cross – section of modelled cable joint

Axial cross–section of modelled cable joint is shown in Fig. 1. T_1 and T_2 are the inner and the outer conductor temperatures. The temperature distribution will be symmetrical around the joint centre. The calculations were done in 2D axial symmetry mode.

If it is presumed that such temperature distribution (T) is also in the surroundings of the cable break (Fig. 1), and:

$$g(C,L_u)=L_u+\sqrt{C^2+L_u^2}\ ; \qquad (2)$$

$$A^2=r^2+a^2-2ar\cos\theta';\ B^2=r^2+b^2-2br\cos\theta',\qquad (3)$$

where r,θ and z are cylindrical coordinates, the approximate expression for relative temperature is:

$$(T-T_2)_{\text{apr}}(r,z)=\frac{T_1-T_2}{2\pi\ln\frac{b}{a}}\int_0^{\pi}\ln\left(\frac{g(B,\,L_2-z)\,g(A,\,z-L_1)}{A^2}\right)\mathrm{d}\,\theta'.(4)$$

If equivalent toroidal heat sources (Q_n) are included in the calculation, the temperature is:

$$T-T_2=(T-T_2)_{\text{apr}}+\sum_{n=1}^{N_1+N_2}\frac{Q_n}{2\pi^2\lambda_2}\frac{K\left(\frac{\pi}{2},p\right)}{\sqrt{(r+a)^2+(z-z_n)^2}}\qquad (5)$$

where $K\left(\frac{\pi}{2},p\right)=\int_0^{\pi/2}\frac{d\alpha}{\sqrt{1-p\sin^2(\alpha)}}$ is complete elliptic integral of the first kind with modulus p.

II. NUMERICAL RESULTS

After theoretical introduction, one example illustrating HBEM application is presented. 35 kV cable (XHE 49-A, $1x150/25\,\text{mm}^2, 20/35$) is considered (Fig.1). Radius of inner conductor is $a = 7.62\,\text{mm}$, outer radius is $b = 17.5\,\text{mm}$, and $E_0 = \frac{U}{a} = 4.58\,\text{MV/m}$. For applying electrical conductivity in the electro-thermal model the known exponential equation of electrical conductivity is applied (Formula 1 in [3]).

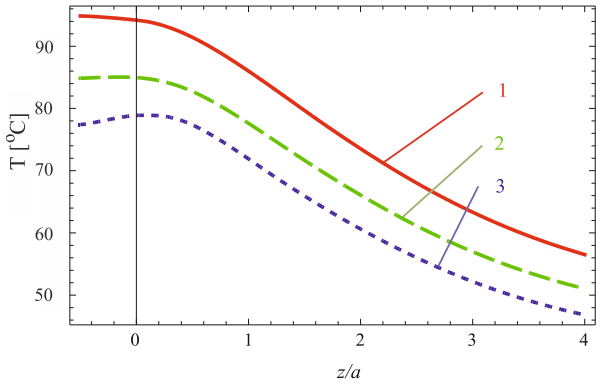

Fig.2. Temperature distribution at outer conductor (1), dielectrics boundary (2) and deflector (3)

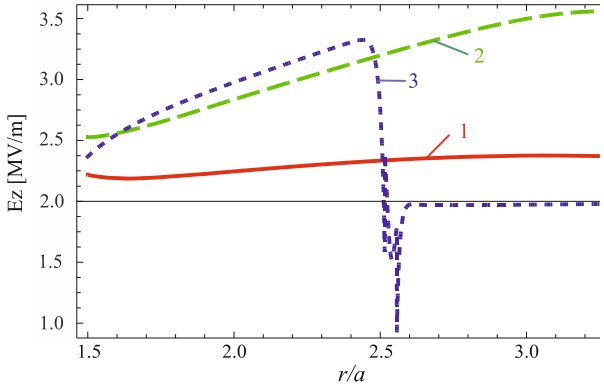

Fig.3. Tangential componente of electric field distribution at outer conductor (1), dielectrics boundary (2) and deflector (3)

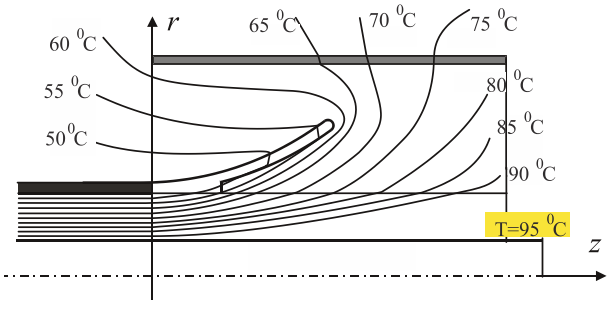

Fig.4. Distribution of isotherms for left side of modelled cable joint

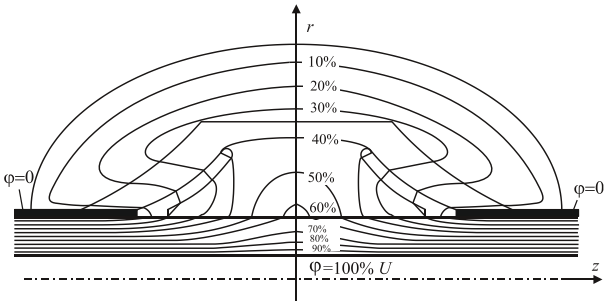

Fig.5. Equipotential curves for modelled cable joint

Temperature distribution at outer conductor (1), dielectrics boundary (2) and deflector (3) is shown in Fig.2.

Axial component of electric field distribution, E_z, in radial direction, r/a for $z/a = 0.5$ (curve 1), $z/a = 2.0$ (curve 2), $z/a = 10.0$ (curve 3), is shown in Fig. 3.

Axial cross-section of isotherms (Fig.4) and equipotential surfaces (Fig.5) for cable joint, where deflector's cones is geometrically modelled, are shown. It is necessary to emphasize that during the determination of the temperature and electric field, the nonlinear electrical conductivity of the cable joint`s insulation was taken into account, which is a function of the temperature and strength of the electric field.

Table I shows the convergence of values for temperature, axial and normal components of the electric field with increasing number of equivalent heat sources. N_1 is number of inner conductor's segments, N_2 is number of outer conductor's segments. The temperatures and electric field calculated by the proposed HBEM method is in a good agreement with those obtained by FEM.

TABLE I
CONVERGENCE OF RESULTS WITH INCREASING NUMBER OF EHS

N_1	N_2	T[°C]	$\frac{E_z}{E_0}$	$\frac{E_r}{E_0}$
4	6	75.67834	2.09086753	1.175434
50	70	77.90091	2.22989081	1.197383
100	150	78.00237	2.23324591	1.245638
500	700	78.01983	2.23887870	1.270499
FEM		78.13982	2.24119879	1.271229

REFERENCES

[1] N. Raicevic, S. Aleksic and S. Ilic, "One numerical method to determine improved cable terminations", *Electric Power Systems Research, Elsevier*, vol. 81, No. 4, pp. 942-948, 2011.

[2] A. Vuckovic, M. Peric, S. Ilic, N. Raicevic and D. Vuckovic, "Interaction magnetic force of cuboidal permanent magnet and soft magnetic bar using hybrid boundary element method", *ACES Journal, The Applied Computational Electromagnetic Society, Mississippi,* vol. 36, No. 11, pp. 1492-1498, 2021.

[3] M. Baferani, T. Shahsavarian, C. Li, M Tefferi, I. Jovanovic and Y. Cao, "Electric field tailoring in HVDC cable joints utilizing electro-thermal simulation: Effect of field grading materials", *Proc. of the 2020 IEEE Electrical Insulation Conference (EIC)*, Knoxville, USA, pp. 400–404, 2020.

SYSTEM PROPOSAL FOR IDENTIFICATION OF THE EQUIVALENT ELECTRICAL CIRCUIT OF LI- BATTRIES

Michal Frivaldsky, Marek Simcak

University of Zilina, Faculty of electrical engineering and information technologies
Univerzitna 1, 010 26, Zilina, Slovakia, e-mail: michal.frivaldsky@feit.uniza.sk

Abstract -
The paper presents a possible system proposal for identification of the components of equivalent RR2C2 electrical circuit of $LiFePO_4$ traction cells required for design of electrical simulation models. Description of determination algorithm with system arrangement are being presented together with description of achieved results, which are based on the comparisons between measurements on real components with developed simulation models.

I. INTRODUCTION

The development of new chemicals, the battery management system or the maximization of battery safety open the wide door for work in this area. The production of batteries is experiencing a significant boom. Many manufacturers are trying to supply new types of batteries, new packaging technologies, or parameter improvements. Development of energy storage systems (ESS) on the other side requires parameters of the batteries, which are not commonly defined or declared by the manufacturers themselves. Therefore, for the purposes of design and development of ESS a system that can detect these parameters is required. In this paper, a concept of the system, which enables to identify parameters of electrical equivalent circuit of the electro-chemical cells, is presented briefly. Evaluation of the accuracy of achieved results are presented as well.

II. EXPERIMENTAL SET-UP

The main components of the system consist of the laboratory programmable load and a programmable power supply. As a control system LabView environment is being proposed, which consists the setting for defining required charging and discharging process and parameters as well (voltage, current, power). At the same time, the cell temperature is monitored and in case of high temperature it is being disconnected from the system. The principle of organization of the experimental set-up is shown in Fig. 1.

Based on the values of measured battery current, the algorithm can directly recalculate what amout of the battery capacity has been charged / discharged. The system is adapted to be able to log measured values during charging, discharging but also during idle state of the battery. The algorithm defines resting periods during charging / discharging process, while these intervals are important for determinaton of the values of RR2C2 electrical equivalent battery circuit [1].

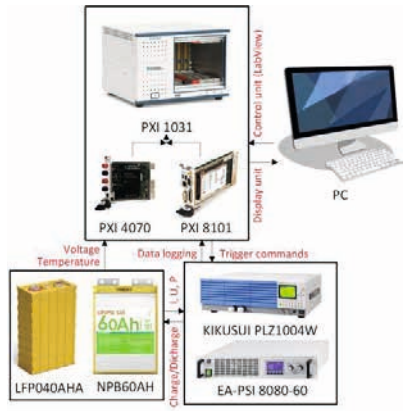

Fig.1. Principle organization of the laboratory set-up for electro-chemical cells identification

III. INDENTIFICATION PROCEDURE

The measured data consists of 4 variables, which are logged every second. The measured variables are the current flowing through the cell, the cell voltage and power which is calculated based on voltage and current variables. The last parameter (battery capacity) is calculated by the algorithm. These 4 variables are updated and recorded every second. All required parameters for equivalent electrical circuit (Fig. 2) of the cell are calculated from mentioned variables, while crucial role plays identification of voltage characteristic (Fig. 3), with indicated pause intervals. More details related to the extraction of the parameter of equivalent schematic are listed in [2] – [4].

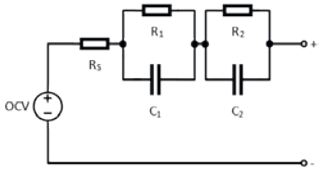

Fig.2. Equivalent electrical circuit of electro-chemical cell

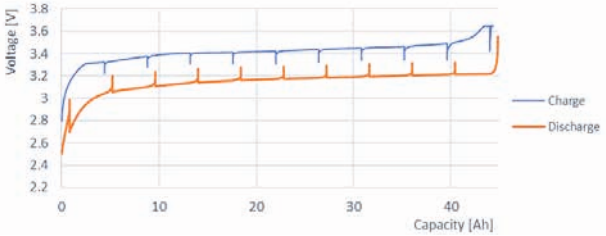

Fig.3. Voltage characteristic of identified cell for purposes of RR2C2 components determination

Based on the voltage characteristic, which was recorded after application of special identification algorithm, the dependencies of parameters of RR2C2 of the equivalent electrical circuit have been identified in dependency on state of the charge (SOC) of identified cell (Fig. 4, Fig. 5).

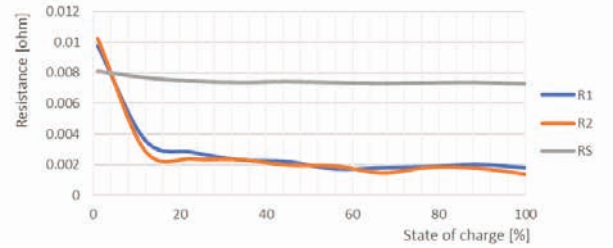

Fig.4. Waveform of dependency of resistance values on SOC

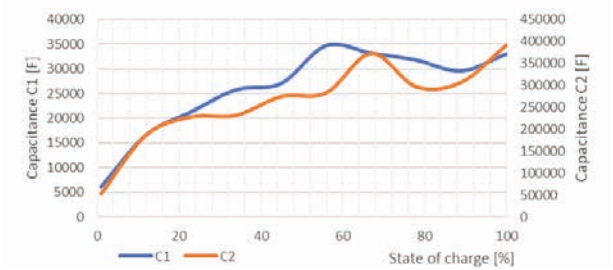

Fig.5. Waveform of dependency of capacitance values on SOC

IV. SIMULATION MODEL OF BATTERY FOR TIME-DOMAIN

Based on received measurements, a simulation model of identified battery was realized (fig. 6). This simulation model is divided into 2 basic parts, the power part (electrical) and the computational part. The power part consists of a controlled DC power supply, passive elements R_S R_1 R_2 C_1 and C_2 and terminals + and -. This part represents the electrical parameters of the cell simulation model. The calculation part consists of the SOC calculation of the cell from the current flowing through the cell. Depending on the current SOC value (Fig. 4, Fig. 5), the elements of the equivalent replacement scheme are calculated.

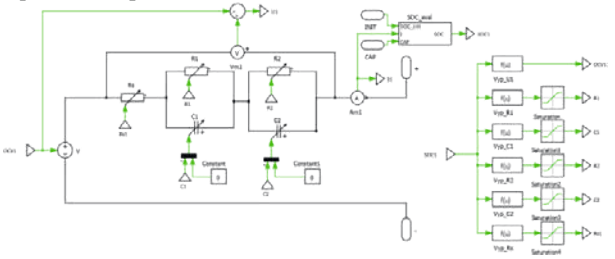

Fig.6. Simulation model of battery for time domain simulation experiments

V. COMPARISON OF THE SIMULATION RESULTS WITH EXPERIMENTS

In the first case, pulse charging procedure of the identified cell is displayed. These waveforms are shown in figure 7. The red waveform represents the real measured values, and the blue cell represents simulation result. It is clear from the figure that identified equivalent electrical circuit for the purposes of design of simulation model, represent accurate system and can be used for design and development of complex energy storage system, where initial simulation analyses are required. Within the total charging process, the relative error varied from 0% to max. 6%. Mostly average error maintains at 1%. Regarding discharging process (Fig. 8) the results are the same as for charging.

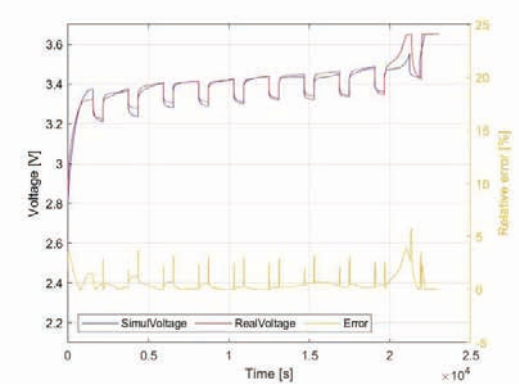

Fig.7. Comparison of the results from experimental measurement and simulation analysis (charging procedure)

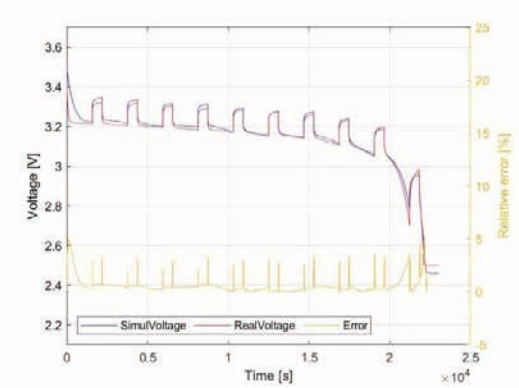

Fig.8. Comparison of the results from experimental measurement and simulation analysis (discharging procedure)

ACKNOWNLEDGEMENT

Authors would like to thank also to national grant agency Vega for project funding Vega-1/0063/21

REFERENCES

[1] Cheng Zhang, Walid Allafi, Quang Dinh, Pedro Ascencio, James Marco, Online estimation of battery equivalent circuit model parameters and state of charge using decoupled least squares technique, Energy, Volume 142, 2018, Pages 678-688, ISSN 0360-5442, https://doi.org/10.1016/j.energy.2017.10.043

[2] Thakkar, R. R. , 2021, 'Electrical Equivalent Circuit Models of Lithium-ion Battery', in K. E. Okedu (ed.), Management and Applications of Energy Storage Devices [Working Title], IntechOpen, London. 10.5772/intechopen.99851

[3] W J Chen et al 2017 IOP Conf. Ser.: Earth Environ. Sci. 73 012024 Eltoumi, F., Badji, A., Becherif, M. and Ramadan, H. S.. "Experimental Identification using Equivalent Circuit Model for Lithium-Ion Battery" International Journal of Emerging Electric Power Systems, vol. 19, no. 3, 2018, pp. 20170210. https://doi.org/10.1515/ijeeps-2017-0210

[4] T. Mesbahi, N. Rizoug, P. Bartholomeüs, R. Sadoun, F. Khenfri and P. Le Moigne, "Dynamic Model of Li-Ion Batteries Incorporating Electrothermal and Ageing Aspects for Electric Vehicle Applications," in IEEE Transactions on Industrial Electronics, vol. 65, no. 2, pp. 1298-1305, Feb. 2018, doi: 10.1109/TIE.2017.2714118

APPLYING THE MODIFIED APPROACH OF FINITE ELEMENT METHOD FOR ANALYSIS NONLINEAR MAGNETIC CIRCUITS

Wojciech Ludowicz and Rafał M. Wojciechowski

Poznań University of Technology, Institute of Electrical Engineering and Electronics,
ul. Piotrowo 3a, 61-138 Poznań, Poland, email: wojciech.r.ludowicz@doctorate.put.poznan.pl

Abstract – **In the paper the modified approach for the Finite Element Method has been presented. Using the combined method of Fixed-Point Method and Harmonic Balance Method the Authors have elaborated the axisymmetric field model of electromagnetic converter that enables to analyze the distribution of both eddy and displacement currents. The converter has been supplied from the voltage source and the analysis has been conducted for saturation state of the core.**

I. INTRODUCTION

Studying the trends in modern electrical engineering, the growing interest in field analysis software could be observed. The field analysis is especially suitable and helpful in the case of nonlinear objects. Equations describing these elements are often quite complex, and it is necessary to use specialized software. The core's nonlinearity level is directly connected with the saturation stage and impacts the electromagnetic field distribution in the whole analyzed object. Besides the saturation effect, in the discussed inductor, some other phenomena also occur, i.e., induction of eddy currents and dielectric displacement currents. Comparing the eddy current effect and displacement current effect, it can be concluded that displacement currents reach noticeable values only for high frequencies. For this reason, the impact of the displacement currents on the distribution of electromagnetic fields is very often neglected in the open literature. Moreover, in the available commercial software, analyzing this phenomenon is also limited.

The main point of the work is to find and implement new and effective numerical methods for field analysis of areas with an electromagnetic field. Presented and discussed algorithm includes the eddy and displacement current effects as well as the saturation of the core in electromagnetic field distribution. In the paper, the multistage approach for the Finite Element Method combined with the Fixed-Point Method and Harmonic Balance Method has been discussed [1]–[3]. In order to verify the obtained results, the comparative analysis by a chosen commercial software has been proceeded.

II. MODIFIED APPROACH

Elaborated numerical algorithm has been developed on the basis of multistage approach to the Finite Element Method [4]. The analysis has been proceeded on 2D axisymmetric inductor model that has been shown in Figure 1. Presented magnetic field distribution analysis concerns the core region of the converter. Authors have chosen the axisymmetric model due to large simplification of calculations and good convergence level in relation to full 3D model.

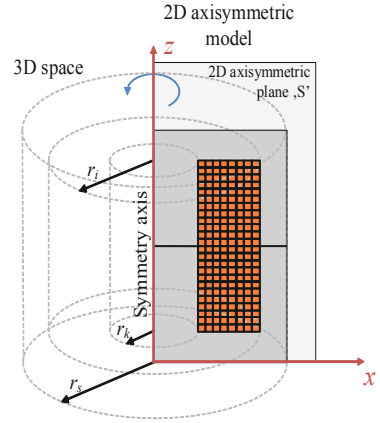

Figure 1. The axisymmetric model of the inductor

The fundamental equation system (1) of the numerical method has been presented below.

$$\begin{bmatrix} \boldsymbol{R}_{\mu o}\left(\nu_{FP}^{k}\right)+j\omega\boldsymbol{G} & -\boldsymbol{c}_o^T\boldsymbol{N}\boldsymbol{z} \\ j\omega\boldsymbol{z}^T\boldsymbol{N}^T\boldsymbol{c}_o & R_c \end{bmatrix}\cdot\begin{bmatrix} \underline{\boldsymbol{\varphi}}_m^{k+1} \\ \underline{i}_{c,m}^{k+1} \end{bmatrix}=FFT\left\{\begin{bmatrix} -\boldsymbol{R}_{\mu o}\left(\nu^k-\nu_{FP}^k\right)\cdot\boldsymbol{\varphi}^k(t)-C\dfrac{\partial^2}{\partial t^2}\boldsymbol{\varphi}^k(t) \\ u_z(t) \end{bmatrix}\right\}_m \quad (1)$$

where: ω is the electrical pulsation of the fundamental harmonic of the supply voltage waveform, m is the order of the considered harmonic, k constitutes the actual iteration step of the calculation process, $\boldsymbol{c}_o$ and $\boldsymbol{c}_o^T$ are appropriate loop matrixes, the $R_{\mu o}$ is the loop reluctance matrix [4], $\boldsymbol{N}$ is the matrix that transposes the values in loops around edges to the values in loops that are ordered to centres of the element faces, vector $\boldsymbol{z}$ represent the number of coil turns arrange in the edge element space-matrix, $\boldsymbol{G}$ and $\boldsymbol{C}$ constitute the matrix of the branch conductances and the matrix of the branch capacitances of elaborated network model, u_z is the supply voltage of the primary winding, R_c is the primary resistance values.

In order to better understand of the Harmonic Balance Method, the right side of the equation system (1) has been reduced to the $\underline{\boldsymbol{S}}$ matrix. In (1) the Harmonic Balance Method as well as the Fixed-Point Method have been already applied [5], [6]. The simplified block diagram illustrating the calculations flow has been shown in Figure 2.

Using the starting values of magnetic permeability ν, fixed-point parameter ν_{FP} and $\underline{\boldsymbol{S}}$ matrix the magnetic flux matrix $\underline{\boldsymbol{\varphi}}_m^{k+1}$ and current matrix $\underline{i}_{c,m}^{k+1}$ can be calculated. On the basis of magnetic induction $\underline{\boldsymbol{B}}$ for individual elements calculated from obtained valued of magnetic fluxes, the new values of magnetic permeability ν for elements could be determined [4]. After applying these values to the equation (1) the calculation of $\boldsymbol{S}_{k+1}(t)$ should be proceeded and then the Fast

Fourier Transform (FFT) should be used in order to transform the matrix $\boldsymbol{S}_{k+1}(t)$ into the complex form $\underline{\boldsymbol{S}}$. This procedure will be repeated until the Singular Value Decomposition ratio (SVD) for input current waveforms $i_c(t)$ is lower than the assumed one.

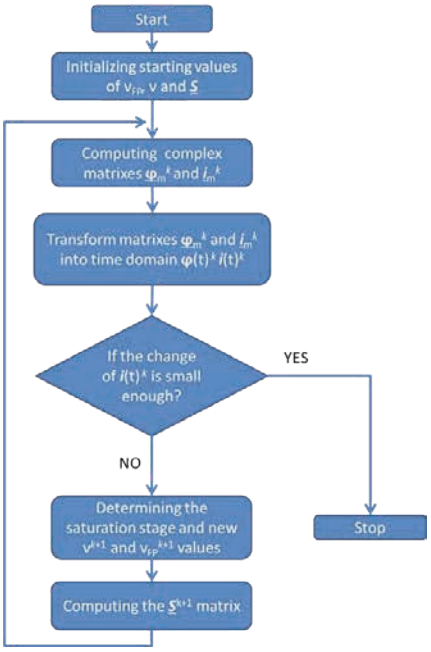

Fig. 2 Block diagram of the proposed method.

III. OBTAINED RESULTS

The output of discussed research is the axisymmetric field model of the inductor. The converter has been supplied by the sinusoidal voltage with 10V of amplitude and 1kHz of frequency. In order to verify the results of conducted calculation the comparison between elaborated field model and one obtained in Comsol Multiphysics has been proceeded. In Fig. 3 and Fig. 4 the waveform of input current and displacement current distribution have been shown respectively.

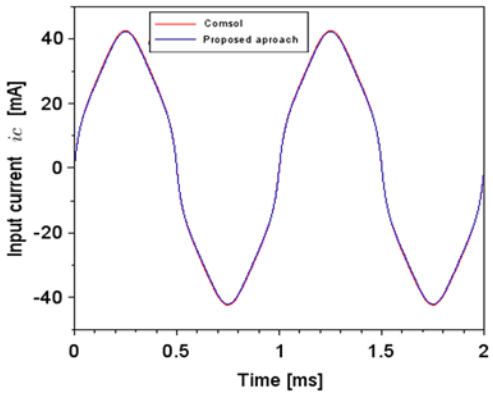

Figure 3. Inductor current i_c waveforms

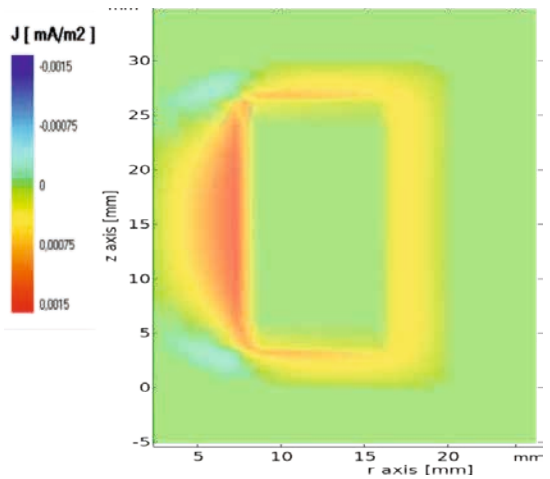

Figure 4. Distribution of displacement current density in ferrite core at time of t = 0.92ms obtained by proposed approach

In Figures 3 and 4 the waveforms and distribution are convergent. The levels of distortion in relation to Comsol's waveforms has been calculated by means of SVD ratio and is equalled to 0.00614.

IV. CONCLUSION

In the work the new and effective method for analysis areas with the electromagnetic field and with contribution of induced eddy and dielectric displacement currents has been presented. The proposed approach has been briefly discussed and explained in form of simplified block diagram. Obtained results have been verified by means of commercial software Comsol Multiphysiscs.

REFERENCES

[1] A. Demenko and J. K. Sykulski, 'Network equivalents of nodal and edge elements in electromagnetics', *IEEE Trans. Magn.*, vol. 38, no. 2, pp. 1305–1308, Mar. 2002, doi: 10.1109/20.996333.

[2] A. Demenko, 'Eddy Current Computation in 3-Dimensional Models for Electrical Machine Applications', in *2006 12th International Power Electronics and Motion Control Conference*, Portoroz, Aug. 2006, pp. 1931–1936. doi: 10.1109/EPEPEMC.2006.4778688.

[3] R. M. Wojciechowski, C. Jedryczka, W. Szelag, and A. Demenko, 'Description of multiply connected regions with induced currents using T-T0 method', *PIER B*, vol. 43, pp. 279–294, 2012, doi: 10.2528/PIERB12061202.

[4] W. Ludowicz and R. M. Wojciechowski, 'Analysis of the Distributions of Displacement and Eddy Currents in the Ferrite Core of an Electromagnetic Transducer Using the 2D Approach of the Edge Element Method and the Harmonic Balance Method', *Energies*, vol. 14, no. 13, Art. no. 13, Jan. 2021, doi: 10.3390/en14133980.

[5] J. Lu, 'Harmonic Balance Finite Element Method: Applications in Nonlinear Electromagnetics and Power Systems', p. 290.

[6] S. Ausserhofer, O. Biro, and K. Preis, 'An Efficient Harmonic Balance Method for Nonlinear Eddy-Current Problems', *IEEE Transactions on Magnetics*, vol. 43, no. 4, pp. 1229–1232, Apr. 2007, doi: 10.1109/TMAG.2006.890961.

AN AUGMENTED MULTIPHASE RAIL LAUNCHER WITH A MODULAR DESIGN: DEVELOPMENT AND CONSTRUCTION

F. Zellmer[1,2,3], M. J. Loeffler[2], M. Schneider[1], C. Kreischer[3]

[1]French-German Research Institute Saint Louis, Electromagnetic Acceleration Group (ERG), 5 rue du Général Cassagnou, F-68301 Saint Louis, France

[2]High Voltage and Pulsed Power Laboratory, Westfälische Hochschule, Gelsenkirchen Bocholt Recklinghausen, Neidenburger Str. 43, D-45897 Gelsenkirchen, Germany

[3]Chair of Electrical Machines and Drive Systems, Helmut Schmidt University, Holstenhofweg 85, D-22043 Hamburg, Germany

***Abstract* – In this paper, a new method to operate a rail launcher is described. The idea to use multiphase alternating current instead of direct current to drive a rail launcher has been brought up quite a while ago [1]. An interesting but not obvious feature of such an approach is that a constant acceleration force can be realized.**
However, in comparison to conventional launchers, the whole system has to be re-designed. The setup is more complex as more than two rails are required and an appropriate power supply has to be developed.

I. GENERAL INFORMATION

Electromagnetic rail launchers are used for the acceleration of macroscopic objects to high speeds. To that end, a sliding electric contact, named the armature, is placed between two conductive rails. If the rails are connected to an electrical power source, a current begins to flow from the source to the first rail, through the armature to the second rail and back to the source. Due to the current flow in the rails, a magnetic field builds up behind the armature. The interaction of this field with the current passing the armature leads to an accelerating Lorentz force. Usually, a payload is placed in front of the armature and therefore pushed towards the muzzle. A rail launcher for military applications is called railgun and uses direct current with amplitudes up to several MA corresponding to a GW power range. That allows for reaching output speeds of some km/s results for relatively short acceleration lengths. Typically, capacitor banks are used as power supplies. However, other applications have also been suggested such as space launch. In that context, a multiphase alternating current setup could be of interest.

II. THEORY

In order to theoretically describe a multiphase rail launcher, it is assumed that the driving currents are sinusoidal, have a constant effective value and a fixed phase angle to each other. In order to describe the system, it is convenient to use the complex notation for n phases

$$i_k = \hat{\imath} * \sin(\omega * t + \varphi_k) = \hat{\imath} * \sin\left(\omega * t + \frac{k-1}{n} * 2\pi\right) \quad (1)$$

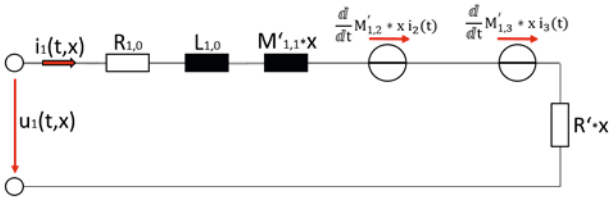

Fig. 1: Schematic single phase diagram (exemplary for L1) of of a three phase rail launcher system.

Fig. 1 shows the equivalent circuit of one phase of a three phase multiphase railgun. Using Kirchhoff's second circuit law, an equation for the terminal voltage u_k in general results:

$$u_k(t,x) = R_{k,0}\, i_k + R'\, x\, i_k + \frac{d}{dt} L_{k,0}\, i_k + \frac{d}{dt} \sum_{l=1}^{n} M_{k,l}(x)\, i_l \quad (2)$$

Here and in Fig. 1, x represents the relative position of the armature. $R_{k,0}$ and $L_{k,0}$ represent the resistance and the inductance of the involved static conductors. The non-linearity of the system is due to the movement of the armature. The corresponding terms contain the resistance gradient of the rails R' (similarly M') and the sum of the induced voltages.
Note that since a constant effective value of the currents (eq.1) is assumed, the voltage u_k has to increase because x is monotonously increasing and therefore the same holds for the associated impedances.

Although sinusodial alternating current is able to generate a ~$\sin^2$ propulsion force, multiphase current causes a stationary force [1]. The following example demonstrates this for a three phase setup:

$$\begin{aligned} F &= \sum_{k=1}^{3} \frac{1}{2}(L' - M')\, i_k^2[t] \\ &= \frac{1}{2}(L' - M') \sum_{k=1}^{3} (\hat{\imath} \sin[\omega\, t + (k-1)120°])^2 \end{aligned} \quad (3)$$

One can rewrite (3):

$$F = \frac{3}{2} L'\, \hat{\imath}^2 = 3\, \bar{F}_k \quad (4)$$

III. TECHNICAL INFORMATION

In this contribution, the development of a multiphase launcher prototype working at low power levels is described. If up-scaled, a potential application could be the launch of satellites because in contrast to military applications, a compact design would not be required. On the other hand, the launch of satellites may require high initial speeds. Therefore, a modular setup allowing for more than one acceleration stage is considered. Indeed, the analysis of the electric behavior of a multiphase launcher does also lead to the conclusion that a modular setup is to be preferred (see terminal voltage eq. 2).
Unlike in the case of a dc rail launcher (C-shaped), the armature of a three phase launcher would be Y-shaped. For such a structure, the centre of the driving force rotates on a circle [1]. By using extra rails for the returning conductors on both sides of one leg of the Y, this problem can be solved. The force now acts on the center of the armature.
With regard to the power supply, it is planned to connect the launcher to the public power grid. Originally, the use of a converter e.g. a transformer to enable current multiplication was considered. The following picture shows a 2-D sectional view of of the current density in such a construction, based on a FEM-simulation:

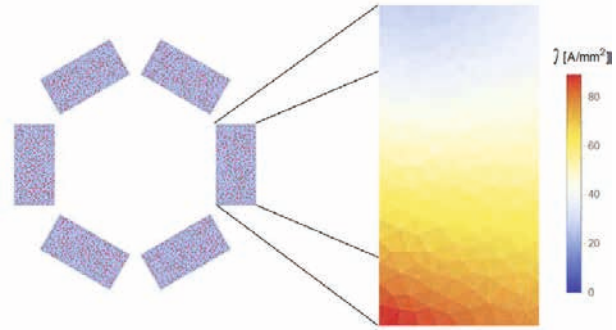

Fig. 2: Current density in a launcher with six rectangular rails

The inhomogeneous current density distribution inside the rails (see Fig. 2, right side) is a negative aspect of that layout. It is caused by the rotary magnetic field due to the phase angles of the currents. To get rid of this effect by using other rail geometries proved to be difficult. However, it turned out that using an „augmented railgun" design can improve the current distribution. Note that the use of extra windings in an augmented setup helps to reduce the effect of the non-linear part of the system, because the overall impedance is less sensitive to x (eq. 2).
The augmented setup design is characterized by using many extra windings (20-40) which are connected in series to the terminal clamps of the accelerator and are located in parallel to the rails in order to increase the magnetic field between them [3]. With a suitable dimensioning, it is possible to connect such an accelerator directly to the power grid. An additional device (e.g. a high-current-transformer) is no longer required.
Instead of current multiplication the launcher works with force multiplication provided by the augmented field [2].
To develop a first experimental setup the mechanical forces caused by the magnetic field have to be estimated. The law of Biot and Savart helps to lay out the components and a CAD-program is used to simulate the mechanical stresses acting on the components. For the optimization of the geometry, the method of the variation of the parameters was used. In this way, the most optimal structure for a maximum output speed can be determined using commonly available materials.
The first experimental augmented multiphase rail launcher called „Trinity 1" is constructed as a module. It is possible to connect multiple modules behind each other. The following figure shows that first module and its projectile:

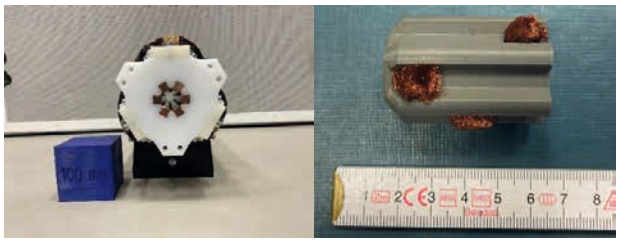

Fig. 3: Front view of the initial module "Trinity 1" with the flange connection (left) and a projectile (right)

That device uses a flange connection to connect more modules. Each one has its own arrangement of rails, independent extra windings and terminal clamps. The armature itself is the payload for a minimum weight of 25 g. It is made out of PLA plastics printed with a 3D-printer to save mass. The sliding contacts are made out of copper brushes in order to ensure both a low friction and a good electrical contact.
This accelerator is designed for direct operation at the 230 V 50 Hz power grid and for consuming a maximum power of approx 450 kVA. Note that specific care has to be taken to protect the public grid against possible experimental failures.
The first experiments were successful. The shot does not damage the armature or the rails and the measurement data are within the expected parameters. The speed reached is above 30 m/s at a 0.5 m long length of the active part of the accelerator.

IV. CONCLUSIONS AND OUTLOOK

As theoretical considerations presented here show, it is possible to generate a constant acceleration force using multiphase alternating current railgun. The use of augmenting static field coils allows to connect the launcher directly to the power grid. This is because the field augmentation reduces non-linear effects and also allows to decrease the amplitude of the driving current. After leaving the launcher an arc discharge forms behind the armature. A lower current amplitude helps to avoid damages. The theoretical models are confirmed by the experimental results. The deviations from the expected speed, taking friction into account, are less than 5 %.
Trinity 1 is the first module of a series of three. The goal is to explore the system performance of a multi-modular setup. Currently, the focus is set on the transfer section between two modules. The full paper will contain experimental results obtained with one stage and supporting the theoretical considerations made above.

REFERENCES

[1] S. K: Murthy, W.F: Weldon, *Multiphase Railgun Systems: A New Concept*, Center for Electromechanics, University of Texas, Austin, 1993

[2] J. Gallant, P. Lehmann, *Experiments with brush projectiles in a parallel augmented railgun*, Royal Military Academy Brussels and French-German Research Institute of Saint-Louis, 2004

[3] Y. He, Y. Guan, S. Song, *Design of a Multi-Turn Railgun for Accelerating Massive Load to High Speed,* China Academy of Engineering Physics, Mianyang, China, 2019

THE DETERMINATION OF THE NONLINEAR DEPENDENCE OF ELECTRIC MACHINE MAGNETIZATION CIRCUIT INDUCTANCE BY ENERGY METHOD

Mykhaylo Zagirnyak, Dmytro Rodkin, Volodymyr Chenchevoi, Olha Chencheva

Kremenchuk Mykhailo Ostrohradskyi National University,
Pershotravneva Str., 20, 39600, Kremenchuk, Ukraine, e-mail: mzagirn@kdu.edu.ua

Abstract **– The paper proposes an analytical method for determining the nonlinear dependence of the inductance of the magnetization circuit of electric machines on the current. The method is based on the equations of power balance, which makes it possible to more correctly take into account the physical phenomena occurring in an electric machine. The accuracy of the method proposed in the digest was assessed by the example of calculating the inductor magnetization curve.**

I. INTRODUCTION

The electric machines (EM) wear and repair result in a deterioration in their operation characteristics. The thermal state of EM is one of the main factors influencing its reliability. It, in turn, is determined by a number of physical processes in the magnetic circuit, which causes changes in EM parameters.

Until now, as a rule, the saturation of EM electrical steel has been taken into account by indirect methods based on the mathematical description of the steel magnetization curve, which is normalized by the manufacturer. However, after EM repair, the use of this method is incorrect, as during operation the properties of electrical steel change. Changing the steel magnetization curve and the nonlinearity of the inductive resistance of the magnetization circuit because of EM long-term operation and repair is one of the issues that requires additional analysis and mathematical description [1, 2].

Therefore, the purpose of the paper consists in the development of an analytical method for determining the nonlinear dependence of the inductance of the magnetization circuit on the current using an energy approach.

II. THEORETICAL PROVISIONS

Consider the following method of refined calculation of inductance dependence on current based on the known voltage and current signals.

Let us assume the dependences of voltage $u(t)$, current $i(t)$ and power $p(t)$ in the following form, respectively:

$$u(t)=\sum_{n=1}^{\infty}\left(U_{na}\cos(n\omega t)+U_{nb}\sin(n\omega t)\right), \quad (1)$$

$$i(t)=\sum_{m=1}^{\infty}\left(I_{ma}\cos(m\omega t)+I_{mb}\sin(m\omega t)\right), \quad (2)$$

$$p(t)=P_0+\sum_{k=1}^{\infty}\left(P_{ka}\cos(k\omega t)+P_{kb}\sin(k\omega t)\right), \quad (3)$$

where index 0 means the constant component of the signal, index a – the cosine component, index b – the sine component, indices n, m, k – the numbers of the harmonics of voltage, current and power, respectively.

The formula for inductance can be represented as follows:

$$L(t)=L_0+L_{tr}(t), \quad (4)$$

where L_0 – inductance in the unsaturated state; $L_{tr}(t)$ – the dependence of the inductance variable component on time.

Since the variable component of the inductance at the initial moment of time ($t = 0$) must be equal to zero, it can be represented by a trigonometric polynomial of the following type:

$$L_{tr}(t)=-\sum_{p=1}^{\infty}L_{pa}+\sum_{p=1}^{\infty}\left[L_{pa}\cos(2p\omega t)+L_{pb}\sin(2p\omega t)\right], \quad (5)$$

where p – inductance harmonic number, L_{pa} and L_{pb} – the amplitude values of inductance for the p-th harmonic of the cosine and sine components, respectively.

When considering processes with nonlinear elements by traditional methods, in particular, using Kirchhoff's law, the number of unknowns requiring determination exceeds the number of possible voltage balance equations [3]. Therefore, to determine the required parameters, it is advisable to use the equations of power balance.

For the easiness of reasoning, consider the simplest equivalent circuit (Fig. 1), which consists of a voltage source $u(t)$, resistance r, constant L_0 and variable $L_{tr}(t)$ components of inductance.

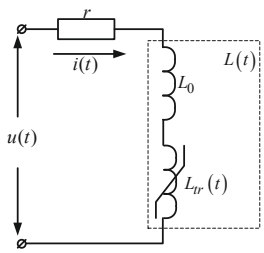

Fig. 1. Induction coil equivalent circuit

The instantaneous power of the circuit elements equals, respectively:

–voltage source:

$$p_i(t)=u(t)i(t)=P_{0i}+P_{kai}\cos(k\omega t)+P_{kbi}\sin(k\omega t); \quad (6)$$

–resistance:

$$p_r(t)=i^2(t)r=P_{0r}+P_{kar}\cos(k\omega t)+P_{kbr}\sin(k\omega t); \quad (7)$$

–the power of the constant component of inductance:

$$\Delta p_L(t) = L_0 \frac{di(t)}{dt} i(t) = \\ = \Delta P_{kaL} \cos(k\omega t) + \Delta P_{kbL} \sin(k\omega t); \quad (8)$$

–the power of the variable component of inductance:

$$p_L(t) = i(t)\left\{ i(t) \frac{dL_{tr}(t)}{dt} + L_{tr}(t) \frac{di(t)}{dt} \right\} = \\ = P_{kaL} \cos(k\omega t) + P_{kbL} \sin(k\omega t). \quad (9)$$

where P_{i0}, P_{0r}, ΔP_{0L}, P_{0L} – the constant components of instantaneous power, and P_{ika}, P_{ikb}, P_{kar}, P_{kbr}, ΔP_{kaL}, ΔP_{kbL}, P_{kaL}, P_{kbL} – the cosine and sine amplitude components of the *k*-th harmonic of the power function respectively of the source, resistance, constant and variable component of the inductance.

According to [3] the equation of power balance for the circuit (Fig. 1) can be presented as follows:

$$p_i(t) - p_r(t) - \Delta p_L(t) = p_L(t). \quad (10)$$

Taking into account expressions (2), (5), based on expression (10) we create a system of equations for finding the harmonic components of the variable inductance $L_{tr}(t)$ based on the following provisions. The constant component of power consists of the terms of expression (10), which have no multiplier cos or sin. The cosine component consists of the terms of expression (10) with factor cos when the frequencies of the right and left are equal: $k = |2m \pm 2p|$, $k = 2m$, $k = 2p$. The sinusoidal component consists of the terms of expression (10) with factor sin when the frequencies of the right and left are equal $k = |2m \pm 2p|$, $k = 2m$, $k = 2p$.

In general, the system of equations has the form:

$$\begin{cases} P_{0i} - P_{0r} - \Delta P_{0L} = P_{0L}; \\ P_{1ai} - P_{2ar} - \Delta P_{2aL} = P_{2aL}; \\ P_{1bi} - P_{2br} - \Delta P_{2bL} = P_{2bL}; \\ \text{----------} \\ P_{kai} - P_{kar} - \Delta P_{kaL} = P_{kaL}; \\ P_{kbi} - P_{kbr} - \Delta P_{kbL} = P_{kbL}; \end{cases} \quad (11)$$

The solution to this system of equations is the coefficients of harmonic components $L_{tr}(t)$, which makes it possible to determine $L(t)$ according to (4).

III. MODELING RESULTS AND CALCULATIONS

As an example for a simple electric circuit containing an inductor with resistance $r = 0.312$ Ohm and inductance in the unsaturated state L_0=0.0874 Gn, we calculate the nonlinear characteristic *L(t)*.

The correctness of the method is verified by the coincidence of the calculated nonlinear dependence $L(t)$ with the given one $L'(t)$.

We set an arbitrary nonlinear dependence $L(i)$ by a power polynomial of the form:

$$L'(i) = a_0 + a_1 i^2 + a_2 i^4 + a_3 i^6 + a_4 i^8 + a_5 i^{10}, \quad (12)$$

where $a_0 - a_5$ – the approximation coefficients equal to: $a_0 = 0.0874$; $a_1 = -9{,}5 \cdot 10^4$; $a_2 = 1{,}4 \cdot 10^{-5}$, $a_3 = 6{,}6 \cdot 10^{-7}$; $a_4 = -7{,}1 \cdot 10^{-9}$; $a_5 = 2{,}5 \cdot 10^{-11}$.

Substituting $i(t)$ instead of i in expression (10), we obtain time dependence $L'(t)$ (Fig. 2, curve 1):

$$L'(t) = a_0 + a_1 i^2(t) + a_2 i^4(t) + a_3 i^6(t) + a_4 i^8(t) + a_5 i^{10}(t). \quad (13)$$

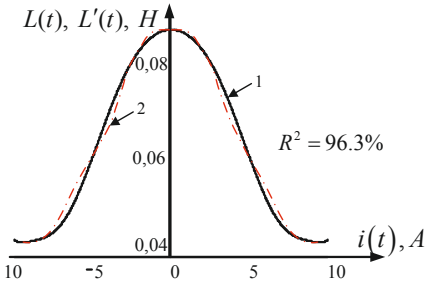

Fig. 2. Inductance dependence on current: 1 - set arbitrary dependence; 2 - calculated dependence, as a result of solving the system of equations

Also, for a given voltage value $u(t) = \sqrt{2} \cdot 80 \cos(\omega t)$, we calculate the current flowing through the circuit with the coil. At the same time there is a distortion of the form of the current signal sinusoid. We perform a return operation – finding the magnetization inductance dependence $L(t)$ on current based on the set dependence of a voltage signal and the received current signal. According to (10), we compose a system of equations for finding the amplitude values of the inductance harmonics of expression (5) taking into account the current harmonics of the largest amplitude ($I_1 = 6.872$, $I_3 = 1.442$, $I_5 = 0.331$, $I_7 = 0.154$, $I_9 = 0.227$).

The assessment of determination coefficient R^2 was used to verify the adequacy. For the given inductance dependence $L(t)$ on current $R^2 = 96{,}3\ \%$ (Fig. 2), which confirms the correctness of the offered method for calculating inductance dependence on current.

IV. CONCLUSIONS

A method for determining the dependence of the inductance of the magnetization circuit on current, based on the power balance equation, has been proposed. Its feature consists in taking into account the current harmonic components that appear in the circuit due to the presence of a nonlinear element. The proposed method makes it possible to accurately determine the nonlinear dependence of the magnetization curve of the magnetic circuit steel through the time dependences of the circuit voltage and current and to assess the state of the magnetic system of electric machines with a long service life.

REFERENCES

[1] P. Andrada, E. Martinez, J. I. Perat, J. A. Sanchez, M. Torrent, "Experimental Determination of Magnetic Characteristics of Electrical Machines", *Conference Record of the 2000 IEEE Industry Applications Conference. Thirty-Fifth IAS Annual Meeting and World Conference on Industrial Applications of Electrical Energy*, 2000, *(Cat. No.00CH37129)*, Rome, Italy, 2000, pp. 263-268 vol.1, doi: 10.1109/IAS.2000.881114.

[2] A. V. Stanković, E. L. Benedict, V. John, and T. Lipo, "A novel method for measuring induction machine magnetizing inductance," *Industry Applications*, *IEEE Transactions on*, vol. 39, pp. 1257-1263, 2003.

[3] M. Zagirnyak, D. Mosiundz, D. Rodkin, "Use of power method for identification of nonlinearity parameters", *Technical Electrodynamics*, no. 1, pp. 3–9, 2017.

COMPARING TWO TOPOLOGY TRANSFORMER HYSTERESIS MODELS DERIVED FROM DC HYSTERESIS MEASUREMENTS

D. Albert[1], L. Domenig[2], P. Schachinger[1], K. Roppert[2], and H. Renner[1]
[1] Institute of Electrical Power Systems, Graz University of Technology, Graz, Austria, dennis.albert@tugraz.at
[2] Institute of Fundamentals and Theory in Electrical Engineering, Graz University of Technology, Graz, Austria, lukas.domenig@tugraz.at

***Abstract* - This paper presents two low-frequency topological transformer models of a three-limb 50 kVA transformer, manufactured with grain-oriented electrical steel sheets. One model is based on the inductance-reluctance analogy and the second models uses the capacitance-permeance analogy. A special saturation measurement with AC and DC is used to parameterize the rate-dependent Jiles-Atherton (JA) hysteresis model, used in the inductance-reluctance analogy model. The rate-dependent hysteresis model (ReCap) in the capacitance-permeance analogy model is implemented by using voltage controlled voltage and current sources. The hysteresis model parameters are identified by means of an optimization problem for the special saturation test. The derived models are validated with the standard no-load test.**

I. Introduction

Electromagnetic power transformer models are used to study the transformer interaction with the connected grid and the transformer transient behaviour. However, the technical challenge of power transformer modelling is the quality and availability of the transformer data. We present a modelling approach including the transformer hysteresis, based on a supplement DC hysteresis measurement. The approach is tested with two transformer topology models, using the capacitance-permeance [1], [2] and the inductance-reluctance (principle of duality) [3] analogy. Both topology models are validated with standard no-load measurements and a saturation test on a three-limb 50 kVA power transformer. The data from the standard transformer factory acceptance test (FAT) are used to parameterize the topology models. The supplement AC saturation test [4] is used to validate the transformer model during saturation.

II. Transformer Equivalent Circuit Models

The representation of electric and magnetic circuits in the electrical domain, is frequently used to analyze the circuit in one simulation environment. An equivalent circuit can be derived by applying the capacitance-permeance analogy (section II-A) or the reluctance-inductance analogy (section II-B).

A. Capacitance - Permeance Analogy

In the capacitance-permeance analogy, the electric and magnetic domain are linked with a gyrator. This component is governed by

$$I_1 = GV_2 \;\&\; I_2 = GV_1, \tag{1}$$

where G is the reciprocal of the number of turns per winding, I and V the corresponding currents and voltages. Using the analogies from Tab. I, an electric equivalent circuit of the magnetic circuit can be derived and interfaced with the gyrator [1]. The hysteresis of the core paths is modeled as nonlinear capacitance with the following relation:

$$\dot{\phi} = \mathcal{P}(\mathcal{F})\frac{\mathrm{d}\mathcal{F}}{\mathrm{d}t} \longrightarrow \phi = \mathcal{P}(\mathcal{F})\mathcal{F}, \tag{2}$$

where ϕ is the magnetic flux, $\dot{\phi}$ is the flux rate, $\mathcal{F}$ is the magneto motive force (mmf) and $\mathcal{P}$ is the permeance. Dissipating losses are modeled as a resistance according to Eq. 3.

$$P_{\mathrm{loss}} = \dot{\phi}^2 R_{\mathrm{m}}. \tag{3}$$

TABLE I: Capacitance-permeance analogy between electric and magnetic circuits

Magnetic Circuit			Electric Circuit		
mmf	$\mathcal{F}$	A	Voltage	v	V
Flux rate	$\dot{\Phi}$	V	Current	i	A
Permeance	$\mathcal{P} = 1/\mathcal{R}$	H	Capacitance	C	F
Flux	$\Phi = \int \dot{\Phi}\mathrm{d}t$	Wb	Charge	$q = \int i\mathrm{d}t$	C
Power	$P = F\dot{\Phi}$	W	Power	$P = vi$	W

B. Inductance - Reluctance Analogy

Magnetic and electric networks are transformed into the respective other domain using corresponding dualities given in Tab. II. The transmission ratio of a transformer can be considered using an ideal transformer with different number of turns. This analogy can be applied to planar networks. This holds true if the transformer under investigation has not more than three windings per limb, if all flux paths are considered [3].

III. DC Hysteresis and AC Saturation Test

The terminals voltage and current response of three-phase three- and five-limb power transformer differ from single-phase transformers. The reason is the mutual coupling of the three phases. The mutual coupling between the phases can be reduced to a minimum, using the measurement setup depicted in Fig. 1a. Exciting the transformer via the terminal connections 1U and 1W results in the flux paths indicated in blue and red in Fig. 1a. The flux in the middle limb vanishes and the mutual

TABLE II: Inductance - reluctance analogies between electric and magnetic circuits

Magnetic Circuit			Electric Circuit		
mmf	$\mathcal{F}$	A	Voltage	v	V
Flux rate	$\dot{\Phi}$	V	Current	i	A
Reluctance	$\mathcal{R}$	H^{-1}	Inductance	L	H
Power	$P = F\dot{\Phi}$	W	Power	$P = vi$	W

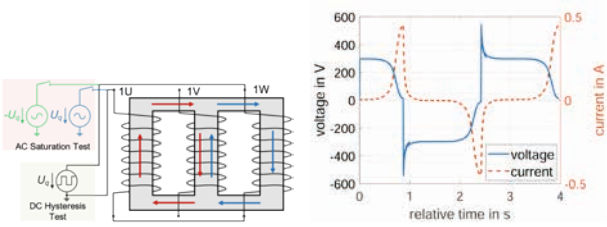

(a) Schematic of AC saturation (red box) and DC hysteresis (green box) test

(b) Current and voltage waveform during DC hysteresis test

Fig. 1: Measurement setups and measured waveforms

coupling between the phases is reduced to a minimum. This setup assumes a homogeneous flux density in the yokes and limbs, which is an acceptable assumption if the flux density in the transformer under investigation is below 1.95 T. This flux density level was evaluated using the validated models presented in [5].

A. DC Hysteresis Measurement

For the DC hysteresis test, three voltage steps with reversal polarity are applied to the transformer terminals (Fig. 1b), whereas the current is limited to a predefined value. The measured terminal current and voltage waveforms are recalculated to a Ψ-I characteristic or Φ-I characteristic.

B. AC Saturation Test

For the AC saturation test, the windings on the outer two limbs of the three-limb transformer are energized with a 50 Hz sinusoidal voltage. The voltage on terminals 1U and 1W are 180° phase-shifted. The voltage amplitude was chosen to be 111 % (415 V_{peak}/phase) of the maximum rated phase voltage. The corresponding measured current waveforms are presented in Fig. 2b.

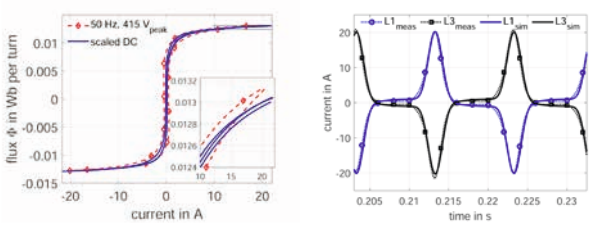

(a) Φ-I from saturation test (red) and scaled Φ-I from DC hysteresis test

(b) Simulated and measured phase currents from the AC saturation test [5]

Fig. 2: Hysteresis characteristics and saturation test waveforms

IV. Model Validation

The measured current waveforms from the AC saturation were successfully used in [5] for the parameter identification of two transformer models, including the transformer core hysteresis. Nevertheless, the AC saturation test can rarely be conducted on large power transformers. To bridge that gap, the DC hysteresis is used to measure the transformer core characteristic for the parameter identification of the transformer core hysteresis model. Two hysteresis models, the JA and the ReCap model, are compared using the current waveforms and the fundamental active and reactive power demand from laboratory measurements as reference. As depicted in Fig. 2a (blue characteristic) the measured current of the DC major loop can be scaled with the rated frequency (50/60 Hz) as scaling factor to its 50 Hz-equivalent. The existing deviation between the scaled DC hysteresis and AC hysteresis characteristic could be caused by the winding capacitance, turning the hysteresis characteristic counterclockwise. It should be noted that the eddy current and excess losses can not be captured by the DC hysteresis test. The losses can be fit to the no-load losses with two model parameters.

V. Conclusion

In conclusion, two topology-corrected electric transformer models have been parameterized to a 50 kVA three-limb power transformer with data from the standardized transformer FAT. To include the hysteresis of the transformer core material, an AC saturation test was successfully used for the hysteresis parameter identification. This approach was further developed using a DC hysteresis test. The DC hysteresis characteristic can be measured with a portable transformer test device. This enables utility owners and manufacturers to study the interaction between the transformer and the surrounding grid, without the need of complex and time consuming models. Further research will focus on the application of the modeling approach in other transformer core types and on the application range of the derived models.

References

[1] R. W. Buntenbach, "Improved circuit models for inductors wound on dissipative magnetic cores." [Online]. Available: https://www.osti.gov/biblio/4832990,journal=

[2] D. C. Hamill, "Lumped equivalent circuits of magnetic components: the gyrator-capacitor approach," *IEEE Transactions on Power Electronics*, vol. 8, no. 2, pp. 97–103, 1993.

[3] E. C. Cherry, "The duality between interlinked electric and magnetic circuits and the formation of transformer equivalent circuits," *Proceedings of the Physical Society. Section B*, vol. 62, no. 2, p. 101, 1949.

[4] D. Albert, D. Maletic, and H. Renner, "Measurement based transformer modelling approach," in *ETG Congress 2021*, 2021, pp. 1–6.

[5] D. Albert, L. Domenig, D. Maletic, A. Reinbacher-Köstinger, K. Roppert, and H. Renner, "Comparing Two Topology Transformer Hysteresis Models with Power Transformer Measurements - Preprint," in *2021 23rd Conference on the Computation of Electromagnetic Fields COMPUMAG*, 2021.

CONTINUUM MODELS AND ANALYTICAL SOLUTIONS FOR FOIL WINDINGS

Jonas Bundschuh[1,2], Herbert De Gersem[1,2], Yvonne Späck-Leigsnering[1,2]
[1]Institut für Teilchenbeschleunigung und Elektromagnetische Felder, Technische Universität Darmstadt, Germany;
[2]Graduate School Computational Engineering, Technische Universität Darmstadt, Germany;
jonas.bundschuh@tu-darmstadt.de

***Abstract*—This paper formulates a continuum model for foil windings with thin foils and develops analytical solutions therefor.**

I. Introduction

Foil windings are used in inductors [1, 2], magnet systems and transformers [3, 4] (Fig. 1a). They are preferred over wire windings or Litz-wire windings because of their better thermal properties, higher fill factor, lower resistance and easier construction [5]. Many analytical models have been developed for foil windings. General approximate formulae for eddy currents in wire windings apply in certain cases [6]. Mostly, however, specialized analytical models are due [1, 7].

Standard finite-element (FE) simulators can deal with massive conductors (bars) and filamentary wire windings. A fully correct FE model for foil windings, however, requires the individual turns to be treated as bars, which requires them to be resolved by the FE mesh (Fig. 1b). For models with several foil windings, each having dozens of turns, this would lead to unmanageably large FE meshes. In [8], as an alternative, a continuum model for foil windings with thin foils and an according FE solver have been proposed. Until now, analytical solutions for this continuum model do not exist, although they may be extremely valuable for fast prototyping of foil windings that exhibit a substantial eddy-current redistribution in the foil's plane directions.

II. Continuum Model

The continuum model is valid when the foil thickness is smaller than the skin depth. Consider a cylindrical foil winding with N_foil turns, a radial and axial extend $(r, z) \in [r_1, r_1 + a] \times [0, b]$, excited by a current i_foil with angular frequency $\omega = 2\pi f$ and frequency f. The magnetic field is described by the magnetic vector potential $\vec{A} = A_\varphi(r, z)\vec{e}_\varphi$ solved from the partial differential equation (PDE)

$$\frac{\partial}{\partial r}\left(\frac{1}{r}\frac{\partial (rA_\varphi)}{\partial r}\right) + \frac{\partial^2 A_\varphi}{\partial z^2} - \xi^2\left(A_\varphi - \frac{1}{b}\int_0^b A_\varphi \,\mathrm{d}z\right) = -\frac{\mu N_\mathrm{foil}}{ab} i_\mathrm{foil}\,, \quad (1)$$

with μ the constant permeability, σ the constant conductivity and $\xi = \sqrt{\jmath\omega\sigma\mu}$ the Helmholtz constant, related to the skin depth $\delta = \sqrt{\frac{2}{\omega\sigma\mu}}$ by $\xi = (1 + \jmath)/\delta$.

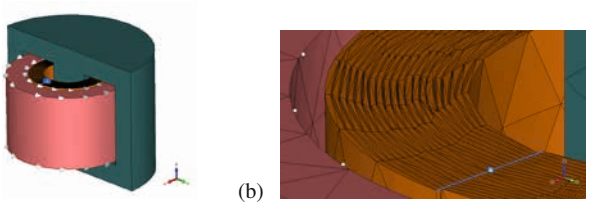

(a) (b)

Figure 1: (a) Geometry and (b) FE mesh of a pot transformer with a wire winding (red, outer coil, high-voltage side) and foil winding (orange, inner coil, low-voltage side).

III. Analytical Solution

Here, only the analytical solution for the axisymmetric case is sketched. The PDE is solved by separation of variables, giving rise to two families of solutions, being products of harmonic functions in one and hyperbolic functions in the other direction. Along r, Bessel functions of first order arise. Along z, a Fredholm integrodifferential equation of second kind appears and lead to function sets which are particular for the foil-winding case. For the example of magnetic and electric boundary conditions (BCs) at $z = 0$ and $z = b$, respectively, an orthogonal set of harmonic functions of the form

$$\frac{\cos(g_m z) - \cos(g_m b)}{1 - \cos(g_m b)} \quad (2)$$

is found. The factors g_m are found numerically as solutions of the transcendental equation

$$\frac{\tan(g_m b)}{g_m b} = 1 + \frac{g_m^2}{\xi^2}\,. \quad (3)$$

The separation constants are $k_m^2 = g_m^2 + \xi^2$. The hyperbolic solutions of the Fredholm integrodifferential equation with a magnetic BCs at $z = 0$ read

$$\cosh(g_m z) + \frac{\xi^2}{k_m^2}\frac{\sinh(g_m b)}{g_m b}\,. \quad (4)$$

The coefficients of the obtained series are determined by enforcing the boundary and interface conditions by the weighted residual method, exploiting the orthogonality of the constructed function sets.

IV. Examples and Conclusions

The new analytical modelling technique is used to study three examples. All results have been verified against FE simulation results exploiting the method presented in [8].

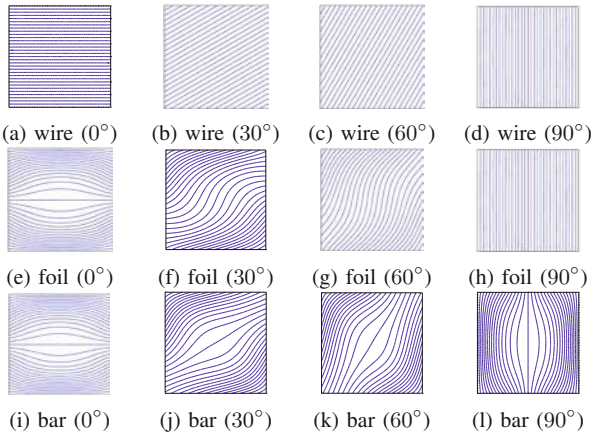

Figure 2: Magnetic flux lines in the xy-plane of a wire winding, foil winding (wound in x-direction) and massive bar submersed in an external magnetic field $\vec{B} = B_{\text{hom}}(\cos\alpha, \sin\alpha, 0)$, $\alpha \in \{0°, 30°, 60°, 90°\}$.

1) The solution for a *cartesian foil winding* with square cross section wound in x-direction, *submersed in a homogeneous magnetic field* $\vec{B} = B_{\text{hom}}(\cos\alpha, \sin\alpha, 0)$ and without current ($i_{\text{foil}} = 0$) is compared to the solutions for a wire winding and a massive bar in Fig. 2. The magnetic flux is not affected by the presence of the wire winding. The massive bar expels the flux in all directions. The foil winding expels the flux in y-direction and allows penetration thereof in x-direction.
2) The impedances of four *cylindrical* winding configurations, *mounted in an infinitely permeable slot*, open at $z = b$, are compared in Fig. 3. The orientation of the foil (Fig. 4) causes the tube- or disk-type foil winding to behave as a massive bar or wire winding, respectively.
3) The magnetic flux lines for *cylindrical coils mounted in a pot inductor with air gap* [9] are compared in Fig. 5. For this model, series expansions are set up for the air-gap domain and the upper and lower coil domains, and are coupled by interface conditions. This is particularly challenging for the tube-type foil winding case, where currents migrate between the upper and lower domains.

The analytical solution of the continuum model for foil windings necessitates the construction of specific function sets. The analytical models allow to study foil windings, e.g., at elevated frequencies and within particular configurations.

References

[1] P. Wallmeier, "Improved analytical modeling of conductive losses in gapped high-frequency inductors," *IEEE Trans. Ind. Appl.*, vol. 37, no. 4, pp. 1045–1054, 2001-07.
[2] X. Mao, W. Chen, and Y. Li, "Winding loss mechanism analysis and design for new structure high-frequency gapped inductor," *IEEE Trans. Magn.*, vol. 41, no. 10, pp. 4036–4038, 2005-10.
[3] G. Diaz and E. Mombello, "Semianalytic integral method for fast solution of current distribution in foil winding transformers," *IEEE Trans. Power Electron.*, vol. 51, no. 9, p. 8401209, 2015-09.
[4] E. L. Barrios, U. Andoni, A. Ursúa, L. Marroyo, and P. Sanchis, "High-frequency power transformers with foil windings: maximum interleaving and optimal design," *IEEE Trans. Power Electron.*, vol. 30, no. 10, pp. 5712–5723, 2015-10.

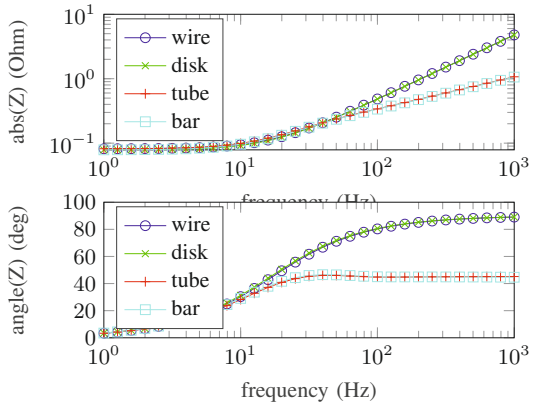

Figure 3: Impedances of a massive bar, wire winding, tube- and disk-type foil winding within a infinitely permeable slot.

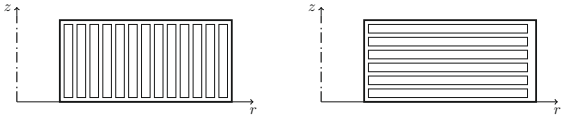

(a) tube-type foil winding (b) disk-type foil winding

Figure 4: Cylindrical foil-winding types.

[5] D. Leuenberger and J. Biela, "Semi-numerical method for loss-calculation in foil-windings exposed to an air-gap field," in *Int. Power Electron. Conf.*, 2014, pp. 868–875.
[6] R. P. Wojda and M. K. Kazimierczuk, "Magnetic field distribution and analytical optimization of foil windings conducting sinusoidal current," *IEEE Magn. Lett.*, vol. 4, p. 0500204, 2013.
[7] M. K. Kazimierczuk and R. P. Wojda, "Foil winding resistance and power loss in individual layers of inductors," *Int. J. Electron. Telecomm.*, vol. 56, no. 3, pp. 237–246, 2010-09.
[8] H. De Gersem and K. Hameyer, "A finite element model for foil winding simulation," *IEEE Trans. Magn.*, vol. 37, no. 5, pp. 3472–3432, 2001-09.
[9] J. D. Pollock and C. R. Sullivan, "Gapped-inductor foil windings with low AC and DC resistance," in *IEEE Ind. Appl. Conf.*, 2004, pp. 552–557.

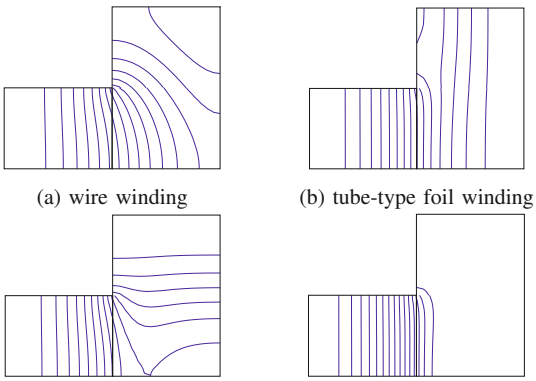

(a) wire winding (b) tube-type foil winding
(c) disk-type foil winding (d) massive bar

Figure 5: Magnetic flux lines for four different coils mounted within a pot inductor with air gap (left domain), coil (right domain), axis (most left line), highly permeable yoke (top and right boundaries) and symmetry plane (bottom).

CONSIDERATION OF SATURATION IN A MULTIPLE COUPLED CIRCUIT MODEL FOR INDUCTION MOTORS WITH PARAMETER IDENTIFICATION

Moritz Benninger, Marcus Liebschner, Christian Kreischer*

University of Applied Sciences Aalen, Faculty of Electronics and Computer Science
Beethovenstr. 1, 73430 Aalen, Germany, e-mail: moritz.benninger@hs-aalen.de

*Helmut-Schmidt-University, Department of Electrical Machines and Drive Systems
Holstenhofweg 85, 22043 Hamburg, Germany, e-mail: christian.kreischer@hsu-hh.de

***Abstract* – This paper presents a novel approach for considering saturation effects within a multiple coupled circuit model for induction motors. The nonlinear effects of saturation are integrated into the modeling by means of a saturation curve depending on individual currents. A method for determining the parameters of the saturation curve is presented, which is mainly based on its practical suitability for industrial applications. The approach uses the differential evolution algorithm in combination with measurement data from the start-up process of an induction motor.**

I. INTRODUCTION

Monitoring and early diagnosis of faults in electrical drives are important tasks in industry to ensure smooth and reliable operation of machines. In the context of fault monitoring, the modeling of electrical machines in different fault conditions plays a major role. Analytical model approaches are usually chosen for this purpose, since numerical simulations using the finite element method (FEM) justify their high cost only for special machines. An analytical approach, on the other hand, is both flexible and transferable, making it ideally suited for practical applications in industry. However, analytical models often fail to consider the effects of magnetic saturation due to simplifying assumptions. Yet, consideration of saturation is necessary to model fault cases, since fault conditions are characterized by nonlinear, dynamic effects.

II. STATE OF THE ART

A classical model approach for the calculation of fault cases in induction motors is the multiple coupled circuit model [1]. This model is based on electrical as well as magnetic parameters and enables the dynamic simulation of electrical machines. The calculation of electrical faults in the stator (e.g. winding short circuit) and in the rotor (e.g. broken bar) is possible [2]. Thereby, using the Winding Function Method (WFM) with knowledge of the basic geometry as well as the winding distribution, the self and mutual inductances M can be calculated in an analytical way [3]. An extension called Modified Winding Function Method (MWFM) allows the consideration of a variable air gap thickness and thus the calculation of mechanical faults such as eccentricities or bearing faults [4].

In the classic version of this modeling, saturation is not considered, it is a strictly linear model. Different approaches exist to include nonlinearity in the multiple coupled circuit model. One possibility is to use a constant factor that scales the inductances at the current operating point according to the saturation [5]. However, this only equals a linearization around a certain operating point and does not reproduce nonlinearity. An alternative approach is to model the influence of saturation by a fictitious increase of the air gap [6-7]. For this purpose, a third harmonic component is added to the existing air gap in the modeling, which reflects the local distribution of the magnetic flux density. Despite the nonlinear consideration, this approach has the disadvantage that the flux distribution only is valid in the case of the healthy state and not in fault cases such as short circuits. Another approach is to separate the inductances $M(\varphi,\mathrm{i})$, which in reality are current- and angle-dependent, into angle-dependent inductances $M(\varphi)$ and current-dependent saturation functions $\mu_{\mathrm{eff}}(\mathrm{i})$ [8]. In general, such a saturation function describes an effective magnetic permeability as a function of the current and is considered as a characteristic curve.

III. GENERAL APPROACH

In our approach, the multiple coupled circuit model serves as the basis for the simulation of the induction motors and is extended with an adjusted concept of the saturation curve. For practical applicability, the method determines the saturation curves based on the optimization algorithm differential evolution using measurement data from the start-up process and the multiple coupled circuit model. The algorithm derives and optimizes the parameters of the saturation curves by a large number of simulations of the model in an iterative process.

A. Modeling of basic machine

For the description of the electrical behavior of the induction motor with the multiple coupled circuit model, the respective resistances R, leakage inductances L and self and mutual inductances $M(\varphi)$ of the stator and rotor circuits are significant:

$$\begin{bmatrix}[U_\mathrm{S}]\\ [U_\mathrm{R}]\end{bmatrix} = \begin{bmatrix}[R_\mathrm{S}] & 0\\ 0 & [R_\mathrm{R}]\end{bmatrix}\begin{bmatrix}[i_\mathrm{S}]\\ [i_\mathrm{R}]\end{bmatrix} + \frac{\mathrm{d}}{\mathrm{d}t}\left(\begin{bmatrix}[L_\mathrm{S}] & 0\\ 0 & [L_\mathrm{R}]\end{bmatrix}\begin{bmatrix}[i_\mathrm{S}]\\ [i_\mathrm{R}]\end{bmatrix}\right) + \frac{\mathrm{d}}{\mathrm{d}t}\left(\begin{bmatrix}[M_{\mathrm{SS}}(\varphi)] & [M_{\mathrm{SR}}(\varphi)]\\ [M_{\mathrm{RS}}(\varphi)] & [M_{\mathrm{RR}}(\varphi)]\end{bmatrix}\begin{bmatrix}[i_\mathrm{S}]\\ [i_\mathrm{R}]\end{bmatrix}\right) \quad (1)$$

In this basic model, the assumption is that the self and mutual inductances $M(\varphi)$ depend only on the rotation angle φ. The inductances are calculated via the Winding Function Method.

B. Modeling of saturation effects

So far, the modeling does not include the influence of nonlinearity. Using the saturation curve, a practicable way is provided to implement the nonlinear saturation behavior into the modeling. While in [8] the saturation curves are calculated by extensive FEM analyses for the individual circuits, in this

method a further simplification is introduced. Overall, the saturation is represented by only two saturation curves, one for the currents in the stator and one for the currents in the rotor. Due to the comparable magnetic conditions, the saturation behavior is assumed to be approximately identical for all stator circuits, as well as for all rotor circuits among each other.

An analytical description of the saturation curve is essential. This is the only way to integrate it into the modeling and to determine the associated parameters in the optimization process. As can be seen in Fig. 1, the saturation curve is assumed equivalent to the behavior of a low-pass filter like in [8]. It is described by the following equation, which is valid for stator and rotor with the magnetic permeability in the unsaturated state $\mu_{\mathrm{eff},0}$ and the delay constant κ. In principle, this equation is applicable to all types of electrical machines:

$$\mu_{\mathrm{eff}}(i) = \frac{\mu_{\mathrm{eff},0}}{\sqrt{1+\left(\frac{i}{\kappa}\right)^2}} \tag{2}$$

By introducing the current-dependent saturation curve $\mu_{\mathrm{eff}}(i)$, the inductance matrix from equation 1 is extended:

$$[\mu_{\mathrm{eff}}(i)\cdot M(\varphi)] = \begin{bmatrix} [\mu_{\mathrm{eff,S}}(i)\cdot M_{\mathrm{SS}}(\varphi)] & [\mu_{\mathrm{eff,R}}(i)\cdot M_{\mathrm{SR}}(\varphi)] \\ [\mu_{\mathrm{eff,S}}(i)\cdot M_{\mathrm{RS}}(\varphi)] & [\mu_{\mathrm{eff,R}}(i)\cdot M_{\mathrm{RR}}(\varphi)] \end{bmatrix} \tag{3}$$

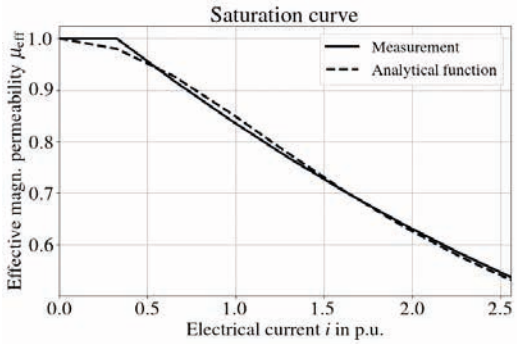

Fig.1. Possible shape for the effective magnetic permeability from measurement (solid) and analytical function (dashed)

C. Parameter identification with differential evolution

The differential evolution algorithm enables the identification of the parameters for the saturation curve. It is a metaheuristic with a small number of hyperparameters, which makes the algorithm very robust and transferable to many applications. Parameter optimization of nonlinear and non-derivable problems is possible [9]. The quantities to be optimized are the magnetic permeability in the unsaturated state $\mu_{\mathrm{eff},0}$ and the delay constant κ, separately for stator and rotor. The mean squared error (MSE) between the measured and simulated stator currents serves as fitness function for the algorithm. The data is obtained from a measurement of the start-up process, which contains the necessary information about the nonlinear saturation behavior. The standard hyperparameters of the algorithm are the differential weight ($F = 0.95$) as the amount of variation of individuals from the population and the crossover probability ($CR = 0.7$) by which individuals are varied or persist. The size of the population is 25 and the number of iterations is 100. In Fig. 2 the simulated courses for the stator currents from the linear modeling and the nonlinear, optimized modeling are compared with the measurement data. The agreement between the real behavior and the optimized model for the startup-current in stator phase A is high with a MSE of 4.76, while the linear modeling cannot reproduce the nonlinear behavior with a MSE of 5.82.

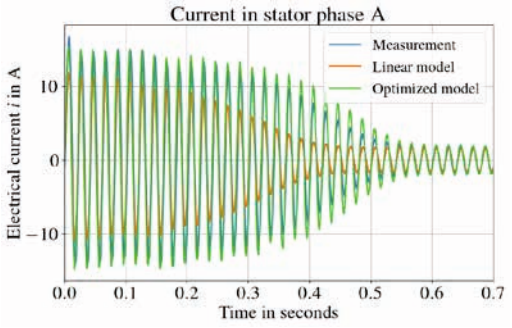

Fig.2. Stator current in phase A of the start-up process for measurement (blue), optimized model (orange) and linear model (green).

IV. CONCLUSION

By extending the multiple coupled circuit modeling of the induction motor with an adjusted concept of the saturation curve, the influence of nonlinearity can be reproduced. For the parameterization of this characteristic curve, measurement data from the start-up of a motor are successfully used in combination with the differential evolution algorithm. With very low effort, the nonlinear behavior of the machine can be modeled very well. This approach is advantageous over FEM simulations or additional measurements for parameterization, which take up a lot of time and effort. Especially in the context of fault monitoring and diagnosis, this approach is well suited to take into account nonlinear effects.

REFERENCES

[1] H. Toliyat, T. Lipo, and J. White, “Analysis of a concentrated winding induction machine for adjustable speed drive applications. i. motor analysis,” *IEEE Trans. on En. Conv.*, vol. 6, pp. 679–683, 1991.

[2] H. Toliyat and T. Lipo, “Transient analysis of cage induction machines under stator, rotor bar and end ring faults,” *IEEE Trans. on En. Conv.*, vol. 10, pp. 241–247, 1995.

[3] X. Luo, Y. Liao, H. Toliyat, A. El-Antably, and T. Lipo, “Multiple coupled circuit modelling of induction machines,” *IEEE Transactions on Industry Applications*, vol. 31, pp. 311–318, 1995.

[4] N. Al-Nuaim and H. Toliyat, “A novel method for modeling dynamic air-gap eccentricity in synchronous machines based on modified winding function theory,” *IEEE Trans. on En. Conv.*, vol. 13, pp. 156–162, 1998.

[5] J. Tang, J. Chen, K. Dong, Y. Yang, H. Lv, and Z. Liu, “Modeling and Evaluation of Stator and Rotor Faults for Induction Motors,” *Energies*, vol. 13, no. 1, p. 133, Dec. 2019.

[6] J. Moreira and T. Lipo, “Modeling of saturated AC machines including air gap flux harmonic components,” *IEEE Transactions on Industry Applications*, vol. 28, no. 2, pp. 343–349, 1992.

[7] S. Nandi, “A detailed model of induction machines with saturation extendable for fault analysis,” *IEEE Transactions on Industry Applications*, vol. 40, pp. 1302–1309, 2004.

[8] J. Rosendahl, Ursachen und Auswirkungen von Windungs- und Phasenschlüssen im Stator großer Synchronmaschinen. Aachen: Shaker, 2010.

[9] Storn, R., Price, K., “Differential Evolution – A Simple and Efficient Heuristic for global Optimization over Continuous Spaces,” *Journal of Global Optimization*, vol. 11, pp. 341–359, 1997.

NEW METHOD BASED ON VARIATIONAL AUTO-ENCODER AND LINEAR DISCRIMINANT ANALYSIS FOR DEMAGNETIZATION IN A PERMANENT MAGNET SYNCHRONOUS MACHINE

Pedram Quseiri Darbandeh, Christian Kreischer*

Helmut Schmidt University, Department of Electrical Machines and drive systems,
Hamburg 22043, Germany, email: quseiri@hsu-hh.de, * email: christian.kreischer@hsu-hh.de.

***Abstract* - This paper proposes a novel method using a vibration signal to detect demagnetization based on Variational Autoencoder (VAE) and Linear Discriminant Analysis (LDA). According to the extracted results from the confusion matrix, it is determined that this method has a valuable ability to detect demagnetization with different severity. Besides, this method, unlike the techniques presented in the past, retains its ability to detect at different speeds and loads. It has a better training time and classification accuracy than machine learning methods, especially in big data.**

I. INTRODUCTION

Demagnetization is one of the non-linear defects in permanent magnet machines causing the reduction in the linkage flux of machines and non-uniform magnetic force. The excessive heat of the machine, improper ventilation, and high current passing through the windings of the electric machine are some of the reasons for demagnetization happening in electric machines. Fig.1 shows the B-H curve of a permanent magnet. As shown in Fig.1, when the machine's operation point (a) changes because of changing machine's load, it is possible that the operation point of the magnet moves below the knee point (b), and does not return back. Therefore, irreversible demagnetization happens.

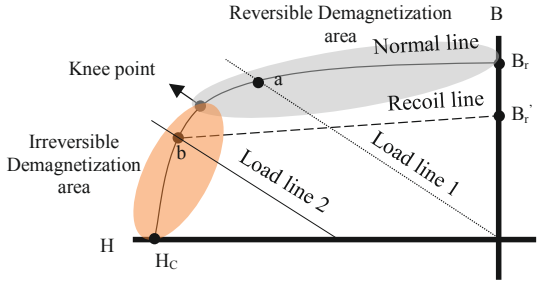

Fig.1. Demagnetization curve by changing the working point of the machine

Techniques such as Fast Fourier Transform (FFT), Short-time Fourier Transform (STFT), and Wavelet are among the processes that each have drawbacks in diagnosis [1]. FFT has no outstanding ability in the non-stationary state where the variance and mean of data change. STFT has a better performance than FFT, but it has some drawbacks, such as finding a proper window for different signals in different conditions. Wavelet uses translating and scaling functions on the mother wavelet to apply real-time signals to extract the crucial features. However, this method has various drawbacks, such as finding a proper mother wavelet for analysis and finding the appropriate decomposition level is hard.

Motor Current Signature Analysis (MCSA) is one of the essential industrial methods to detect partial demagnetization [2]. However, this method is not efficient in detecting uniform demagnetization due to the symmetrical feature of this fault. Uniform demagnetization is when all the permanent magnets of the machine are demagnetized equally. Also, the methods based on investigating the distribution of energy in a time-frequency frame are proposed. A method such as Winger-Ville Distribution is a standard method presented in this domain [3]. However, the most significant drawbacks of this method are the duplication and confusion of data in the distribution. Also, the Empirical Mode Decomposition (EMD) is proposed to compensate for the problem of the Hilbert transform, which does not have a good ability in the stationary signal. This method has two significant drawbacks as final effect and combinations of scenarios in screening [4]. In this research work, a new approach based on deep learning neural networks is proposed to get better classification accuracy than the previous methods and allowing analysis of a high amount of data.

II. METHOD

Variational Autoencoder (VAE) is a method that reduces data dimensionality and reconstructs data again. Also, this method is accounted as the generative methods such as Generative Adversarial Networks (GANs) because of producing new data in its structure.

This method has three critical parts; encoding, hidden layer, and decoding sections. Fig.2 shows the construction of VAE entirely. In the encoder section, the data is entered into the network then, using successive layers, the dimension is reduced. According to each new data coming to the last layer of the encoding network, new data is estimated based on Gaussian distribution in the hidden layer. The estimated data is reconstructed using successive layers. Then, the error is calculated, and the network coefficients are updated according to the difference between input and reconstructed data. Consequently, the bias and weights coefficients are updated using the ADAM optimizer, and backpropagation method. In the structure of VAE, there is a softmax classifier for evaluating the performance of the network in classifying data.

The loss function for variational auto-encoder is defined as follows:

$$\text{Loss} = \|x - \hat{x}\|^2 \qquad (1)$$

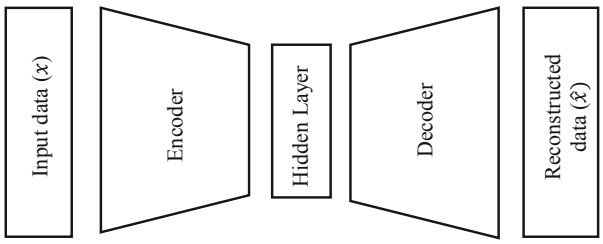

Fig.2. Variational Auto-Encoder scheme

In equation 1, x and $\hat{x}$ are the input data and reconstructed data, respectively. To find the best features for enhancing the separability of classes, Linear Discernment Analysis (LDA) is used. The main goal of LDA is finding the best situation to separate when the mean of each class is located as far as possible, and their distributions are as small as possible. This objective function can be proposed for two classes as follows:

$$J(w) = \frac{|\widetilde{\mu_1} - \widetilde{\mu_2}|^2}{S_1^2 + S_2^2} \qquad (2)$$

In equation (2), μ_1 and μ_2 are means of classes, and also S_1, S_2 are the scatter matrices of classes. In this research work, a 1 kW permanent magnet synchronous machine is used for implementing faults in different states as shown in Fig.3. Besides, a data acquisition system is used to record vibration data. The GRID V100-8Q Graphical Process Unit (GPU) card is used to analyze data in this project. The different scenarios are considered to evaluate this method's ability to use vibration signals. The various fault severity is simulated and implemented in the experimental test with replacing different magnet. In this research, the 12 demagnetization fault classes and one normal class are considered. In this research work, the data is divided into 70% train and 30% test dataset. Besides, the collecting data is done with a 16 kHz sampling rate over 5s.

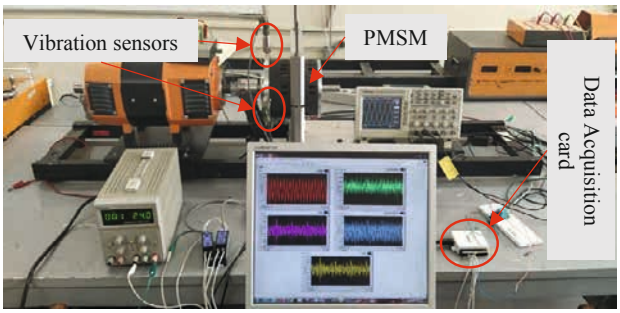

Fig.3. Experimental setup

II. RESULTS

This section shows the results of implementing VAE and LDA on extracted data. The best way to show the ability of this method to separate different classes is a confusion matrix to show the ability of the proposed method in detecting different classes. As illustrated in Fig 4, the confusion matrix of the vibration signal has a 94.15% average accuracy. The training time for 1,040,000 data samples is 00:37.1". It can be seen the method has the improper performance to detect the faults in classes 3 and 10.

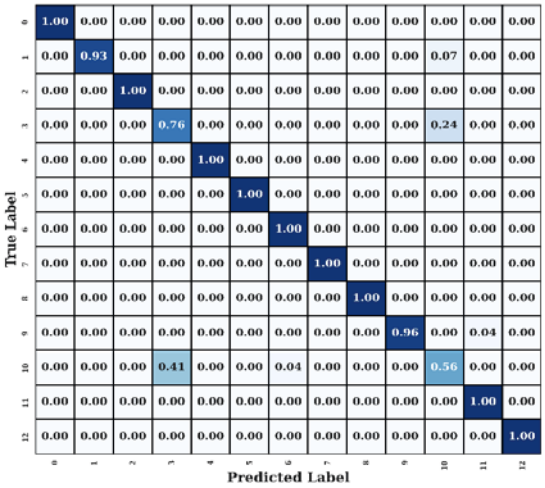

Fig.4. Confusion matrix for vibration sensor

However, when the LDA is used, the confusion matrix has the valuable ability, and the network can detect all classes with **100% classification accuracy**. It can be helpful to denote that the network has a **slower training time with 01':25.2"** compared to the VAE without pre-processing. Also, in this research, the combination of VAE and LDA is implemented for different speeds and loads. The results show that this method has an outstanding performance with **98% average accuracy** for the combination of speed from 20% to 120% and from no load to 120% load. Therefore, **this method can be applicable for a wide range of speeds and loads.**

It is found that the combination of VAE and LDA has an excellent capacity compared to machine learning methods such as the K-Nearest Neighbors (KNN) algorithm, Naïve Bayes (NB), decision tree, and Random Forest (RF) **in the accuracy index**. However, machine learning methods have a better performance than the proposed method **in training time for small-size data**. Also, when the data size starts to grow, the training time and accuracy of the proposed method are better than machine learning methods.

REFERENCES

[1] Quseiri Darbandeh, Pedram, Mohammad Ardebili, and Mahdi Aliyari Shoorehdeli. "Demagnetized Magnet Diagnosis in a Double-Layer Winding Permanent Magnet Synchronous Machine using Wavelet Packet Transform." Computational Intelligence in Electrical Engineering (2021).

[2] Faiz, Jawad, and Ehsan Mazaheri-Tehrani. "Demagnetization modeling and fault diagnosing techniques in permanent magnet machines under stationary and non-stationary conditions: An overview." *IEEE Transactions on Industry Applications* 53.3 (2016): 2772-2785..

[3] V. Climente-Alarcon, J. A. Antonino-Daviu, M. Riera-Guasp, and M. Vlcek, "Induction motor diagnosis by advanced notch FIR filters and the Wigner–Ville distribution," IEEE Transactions on Industrial Electronics, vol. 61, no. 8, pp. 4217-4227, 2013.

[4] Chen, Yong, et al. "Faults and diagnosis methods of permanent magnet synchronous motors: A review." *Applied Sciences* 9.10 (2019): 2116.

ELECTRIC FIELD ANALYSIS OF HIGH VOLTAGE DISCONNECTORS AT COMPOSITE VOLTAGE WITH FINITE ELEMENT METHOD

Mirac Yazici*, Özcan Kalenderli, Mehmet Murat Ispirli

*Istanbul Technical University, Electrical Engineering Department
Maslak, 34469 Istanbul, Turkey, e-mails: yazicimirac1@gmail.com , kalenderli@itu.edu.tr

Marmara University, Electrical-Electronic Engineering Department,
Maltepe, 34584, Istanbul, Turkey, e-mail: mispirli@marmara.edu.tr

***Abstract* – In this study, the effects in terms of electric stress of composite voltages on high voltage disconnectors were investigated. As the disconnector model, a single-phase center-break disconnector was considered. In order to examine the effects of composite voltages on high voltage disconnectors, a model is defined in the COMSOL Multiphysics program. After the application of composite voltage to the disconnector, electrical potential and electric field distributions were obtained. It has been observed that the maximum electrical potential and the maximum electric field strength values on the disconnector are higher when composite voltage is applied to the disconnector.**

I. INTRODUCTION

High voltage systems are needed for the efficient use of electrical energy. Various devices and equipment are required for the safe operation of high voltage systems. It is essential that such devices and equipment can be used conveniently and safely in high voltage systems [1]. For this reason, the conditions that the devices and equipment will be exposed to must be determined in advance and tested, whether they can withstand these conditions. However, sometimes these tests cannot include every condition faced at the real application. One of these conditions is that high voltage disconnectors are exposed to composite voltage and how they will behave under these voltages.

Composite voltages are the voltage form obtained by the combination of different voltages [2]. Composite voltages can occur spontaneously in nature. For example, composite voltage is a voltage form that occurs with applying a lightning impulse to a device works under operating voltage.

High voltage disconnectors are devices that can open and close when the circuit is unloaded in high voltage systems and provide the required isolation distance [3]. In this study, a 170 kV single-phase center-break disconnector model was considered. Center-break disconnectors are the disconnector model in which both contacts of both poles are movable and these contacts meet at the midpoint of isolation distance of the disconnector. The single-phase center-break disconnectors consist of two terminals such as all switches.

In this study, electric field analysis of high voltage disconnectors under composite voltage was obtained using the Finite Element Method (FEM). It was evaluated what kind of effects the conditions that occurred in practice but outside the type tests had on the disconnectors by these analyses. In order to examine the effects of composite voltages on the disconnectors, a model is created in the COMSOL program. In order to understand the effects of the composite voltage on the disconnector, the lightning impulse voltage and the AC (50 Hz) voltage were applied to the disconnector separately. Then, electric field analysis was obtained under composite voltage by applying these voltages together. All of these analyzes were applied separately for both open and closed positions of the disconnector. The electrical potential and the electric field distributions obtained after the application of voltages are given for certain moments. In addition, a point has been determined on the contact and terminal surface, which is the most important parts of the disconnector, and the electrical potential and the electric field graphics of these points are given.

II. EFFECTS OF COMPOSITE VOLTAGES ON HIGH VOLTAGE DISCONNECTOR

A closed region is needed to realize the solution with the finite element method. For this reason, the disconnector model was modelled in a rectangular prism. After that, the model has been discretized into finite elements. The created FEM models for different positions of the disconnector are shown in Fig. 1. The analysis contains two working positions which are open and closed of the disconnector.

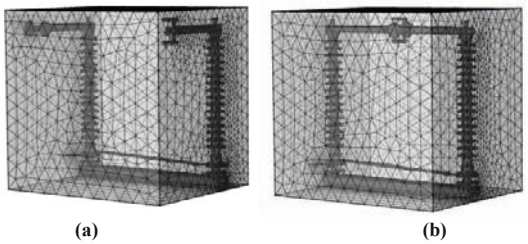

Fig. 1. The created FEM models for different positions of the disconnector: **a)** Open position; **b)** Closed position.

A. Application of composite voltage across the isolation distance when the disconnector is open

The disconnector performance is evaluated in case of lightning impulse voltage reaching in the disconnector in addition to the operating voltage when the disconnector is open position. According to the IEC 62271-1 across the isolation distance, the lightning impulse test voltage is 860 kV for 170 kV rated voltage disconnectors [4]. 170 kV voltage level is the effective value of the highest allowable voltage level between phases.

$$u(t) = 98.15 \cdot 10^3\sqrt{2} \cdot sin\omega t = 138.8 \cdot 10^3 \cdot 2\pi f t \quad (1)$$

$$V(t) = -860 \cdot 10^3 (e^{-1.49 \cdot 10^4 t} - e^{-1.63 \cdot 10^6 t}) \quad (2)$$

When considered in terms of operating conditions of a single-phase disconnector effective value of voltage is approximately 98.15 kV. The equations of power frequency operating voltage and the lightning impulse voltage are given in Eq. (1) and Eq. (2), respectively. When the application of a composite voltage across the isolation distance Eq. (1) and Eq. (2) had been used together. In Eq. (1), the frequency (f) of operating voltage is taken as 50 Hz.

For the open position of the disconnector, the electric potential and electric field distributions at 10. µs after applied composite voltage are given in Fig. 2 and Fig. 3, respectively. Lightning impulse voltage and power frequency operating voltage were applied simultaneously to the terminals of the disconnector in the open position. While these voltages are applied to the disconnector, lightning impulse voltage is applied to the one terminal and power frequency operating voltage is applied to the other terminal. In order to observe the most disadvantages situation, the lightning impulse voltage was applied when the power frequency operating voltage was maximum. The negative pole lightning impulse voltage is adjusted to coincide with the positive pole of the power frequency operating voltage. In this case, it is aimed that the potential difference between the terminals is maximum. Thus, electric field strength can reach maximum.

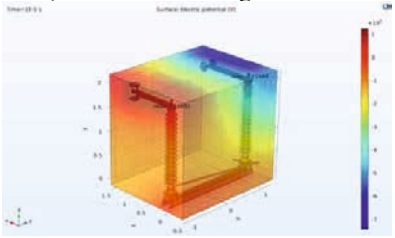

Fig. 2. Electric potential distribution at 10. µs after applied composite voltage

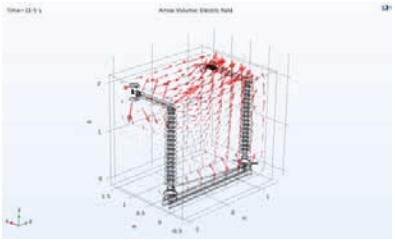

Fig. 3. Electric field distribution at 10. µs after applied composite voltage

B. Application of composite voltage phase to earth when the disconnector is closed

The disconnector performance is evaluated in case of lightning impulse voltage reaching in the disconnector in addition to the operating voltage when the disconnector is closed position. According to the IEC 62271-1 phase to earth, the lightning impulse test voltage is 750 kV for 170 kV rated voltage disconnectors [4].

$$V(t) = 750 \cdot 10^3 (e^{-1.49 \cdot 10^4 t} - e^{-1.63 \cdot 10^6 t}) \quad (3)$$

The equation of lightning impulse voltage is given in Eq. (3) for phase to earth test voltage in 170 kV rated voltage disconnectors. When the application of composite voltage phase to earth Eq. (1) and Eq. (3) had been used together. For the closed position of the disconnector, the electric potential and electric field distributions at 10. µs after applied composite voltage are given in Fig. 4 and Fig. 5, respectively. Lightning impulse voltage and power frequency operating voltage were applied simultaneously to the disconnector in the closed position. While these voltages are applied to the disconnector, lightning impulse voltage is applied to the one terminal and power frequency operating voltage is applied to the other terminal. In order to observe the most disadvantages situation, the lightning impulse voltage was applied when the power frequency operating voltage was maximum. The positive lightning impulse voltage is adjusted to coincide with the positive of the power frequency operating voltage. In this case, it is aimed that the potential difference between the terminals and the chassis is maximum. So, electric field stress can reach maximum in the closed position of the disconnector.

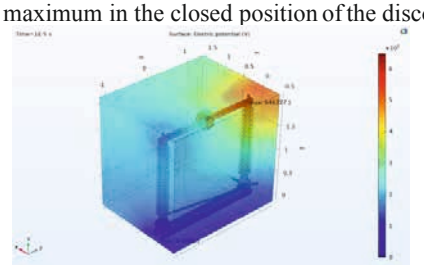

Fig. 4. Electric potential distribution at 10. µs after applied composite voltage

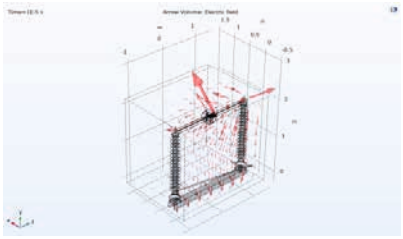

Fig. 5. Electric field distribution at 10. µs after applied composite voltage

III. CONCLUSION

The composite voltage that is obtained from combined the lightning impulse voltage and the power frequency operating voltage, causes more forces on the disconnector.

The result of this study shows that although IEC standards for the disconnectors already determine the type test conditions for the most challenging conditions, more durable system and product modeling can be made as a result of the examinations to be made by the country authorities for their own work areas. In this way, systems that are both safe and durable can be established.

REFERENCES

[1] M.S. Naidu, V. Kamaraju, *High voltage engineering*. New Delhi, McGraw-Hill, 1994.
[2] O. Kalenderli, E. Onal, "Design of composite high voltage generation circuits", *National Conference on Electrical, Electronics and Biomedical Engineering., pp. 363-367.*
[3] IEC 62271-102: High voltage switchgear and controlgear-Part 102: Alternating current disconnectors and earthing switches, Switching devices, 2017.
[4] IEC 62271-1: High voltage switchgear and controlgear-Part 1: Common specifications for alternating current switchgear and controlgear, General terms and definitions, 2017.

STUDY OF CONVERGENCE OF NEWTON METHOD BY FE SIMULATION WITH VECTOR HYSTERESIS STOP MODEL

Xiao Xiao, Fabian Müller, Martin Nell, Kay Hameyer

RWTH Aachen University, Institute of Electrical Machines (IEM)
D-52062 Aachen, Germany, E-Mail: xiao.xiao@iem.rwth-aachen.de

Abstract – **Incorporating a hysteretic material model, such as the vector stop model, into the Finite Element (FE) Analysis requires an iterative process to resolve the non-linearity. The Newton Method is a preferred approach, due to its quadratic convergence close to the solution. However, this approach is very sensitive regarding the starting point and states distinct requirements to the non-linear function in terms of monotony and smoothness. Particularly for hysteretic problems, these conditions have to be guaranteed. In this paper the differentiation of the vector stop model, utilized to evaluate the Jacobian matrix, is studied. The Newton Method is analysed to ensure reliable and stable FE simulations.**

I. INTRODUCTION

Hysteresis models in a dual representation of the magnetic field are particularly well-suited models to analyze soft magnetic materials in the magnetic vector potential formulation, which is employed in the FE Analysis. The vector stop model belongs to this family of hysteresis models and is very accurate in resolving the anisotropy and hysteresis of ferromagnetic materials. The vector material model should be able to provide the continuous derivative in the form of differential reluctivity tensor $\boldsymbol{\nu_d}$ and the $\boldsymbol{\nu_d}$ should be positive definite. This evaluation is difficult or even impossible, as the material model may not be continuously differentiable [1]. To overcome this problem, an equivalent representation of the differentiation is implemented and discussed in [2]. As the Newton Method is sensitive to the derivative, the insufficient $\boldsymbol{\nu_d}$ may lead to divergence [3]. Furthermore, the initial guess point of the Newton iteration should be close to the solution point, otherwise the approach may be not stable and fail to converge.

The vector hysteresis stop model presented in this work, is constructed with stop operators. Each of the stop operators has two magnetization states according to the input magnetic flux density and the threshold value of the operator. Therefore, the derivative of $\boldsymbol{H}(\boldsymbol{B})$ is discontinuous, as the operator jumps between the two states. The Newton Method is not suited to solve this problem as previously presented, but Fujiwara et al. [4] presented an optimal relaxation method to prevent the Newton steps from divergence. This method based on residual monotonicity test is used in previous work [5] to deal with the Jiles Atherton's model. In this work another relaxation method based on natural monotonicity test [6] is used to solve the magnetic field problem with a vector hysteresis stop model.

II. CONVERGENCE BEHAVIOR OF THE NEWTON METHOD WITH VECTOR HYSTERISIS STOP MODEL

The n^{th} stop operator of a vector hysteresis stop model can be written as [7]:

$$\boldsymbol{S}_n = \boldsymbol{B}_{\text{re}}{}^{t} = \begin{cases} \boldsymbol{\Omega}_n & if \left| \boldsymbol{R}_{\text{temp\_}n}{}^{-1} \boldsymbol{\Omega}_n \right| < 1 \\ \boldsymbol{R}_{\text{temp\_}n} \dfrac{\boldsymbol{\Omega}_n}{|\boldsymbol{\Omega}_n|} & if \left| \boldsymbol{R}_{\text{temp\_}n}{}^{-1} \boldsymbol{\Omega}_n \right| \geq 1 \end{cases}, \tag{1}$$

where $\boldsymbol{\Omega}_n = \mathrm{d}\boldsymbol{B} + \boldsymbol{S}_n{}^{t-1}$, $\mathrm{d}\boldsymbol{B} = \boldsymbol{B}^t - \boldsymbol{B}^{t-1}$ and $\boldsymbol{R}_{\text{temp\_n}}$ is the threshold diagonal matrix. $\boldsymbol{R}_{\text{temp\_n}}$ describes the threshold values in x and y directions of the n-th stop operator.

To demonstrate the differentiation of the stop model, an alternating excitation from -1.6 T to $+1.6$ T in 30 ° is applied to the model. The vector hysteresis stop model is calculated with the weight w_n for the n$^{\text{th}}$ operator and the values interpolated from the anhysteretic surfaces $\boldsymbol{H}_{\text{anhys}}(\boldsymbol{B})$:

$$\boldsymbol{H}(\boldsymbol{B}) = \Sigma_{n=1}^{N} w_n \, \boldsymbol{H}_{\text{anhys}}(\boldsymbol{S}_n) \,. \tag{2}$$

A graphical illustration of the interpolated values $\boldsymbol{H}_{\text{anhys}}(S_{nx})$ in x direction of n$^{\text{th}}$ stop operator with constant threshold values is shown in Figure 1 a). As long as the excitation, which evaluated as $\boldsymbol{\Omega}_n$ from the time step t, is smaller than the threshold value $\boldsymbol{R}_{\text{temp\_}n}$, the $\boldsymbol{S}_n$ keeps updating with the value of $\boldsymbol{\Omega}_n$. This leads to the left and right curves in Figure 1 a). Until the input $\boldsymbol{\Omega}_n$ exceeds the threshold value, the $\boldsymbol{S}_n$ suddenly remains on the value of $\boldsymbol{R}_{\text{temp\_}n}$. This activation of the operator results in the upper and lower horizontal lines as shown in Figure 1 a). The differential reluctivity tensor in equation (3) is calculated by automatic differentiation.

$$\boldsymbol{\nu}_{\mathbf{d}} = \frac{\partial \boldsymbol{H}}{\partial \boldsymbol{B}} = \begin{bmatrix} \frac{\partial H_x}{\partial B_x} & \frac{\partial H_x}{\partial B_y} \\ \frac{\partial H_y}{\partial B_x} & \frac{\partial H_y}{\partial B_y} \end{bmatrix} \tag{3}$$

Thus, $\boldsymbol{\nu_d}$ results in a jump as the operator activated, which can be seen in Figure 1 b).

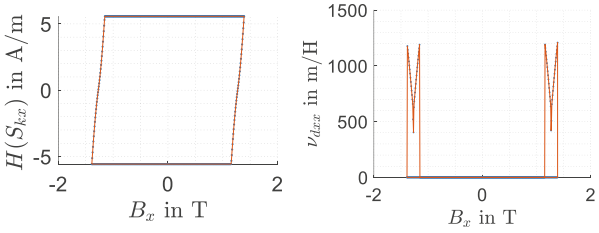

a) b)

Figure 1. a) The x component of the interpolated anhysteretic surfaces stop operator $\boldsymbol{H}_{anhys}(\boldsymbol{S}_{kx})$ b) Evaluated differential reluctivity tensor in x direction $\boldsymbol{\nu}_{dxx} = \frac{\partial \boldsymbol{H}_{anhys}(\boldsymbol{S}_{kx})}{\partial B_x}$.

The $\boldsymbol{H}(\boldsymbol{B})$ is constructed with parallel connections of the stop operators. The differential reluctivity tensor $\boldsymbol{\nu_{dxx}}$ of the stop model under one periodic alternating excitation in 30° is exhibited in Figure 2. In the subfigure Figure 2 b), the jump from the stop operator can be observed in the $\boldsymbol{\nu_{dxx}}$ of the vector hysteresis stop model.

For higher excitations, the anhysteretic surfaces and the corresponding $\boldsymbol{\nu_d}$ surfaces are extrapolated values for high saturation with a constant reluctivity value of the air. This will be presented in the extended paper.

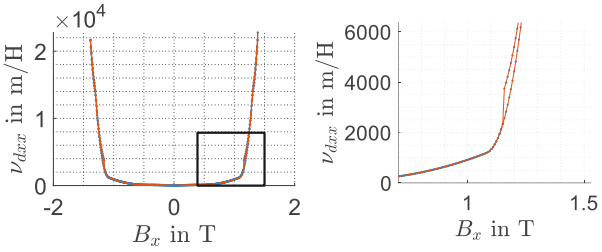

a) b)

Figure 2. a) Differential reluctivity tensor $\boldsymbol{\nu_{dxx}}$ of the stop model. b) Enlarged in the range of the $\boldsymbol{\nu_{dxx}}$, where the jump occurs.

III. NEWTON RELAXATION TECHNIQUE FOR FIELD PROBLEMS WITH VECTOR HYSTERESIS STOP MODEL

Applying the relaxation factor α to the Newton Method, the range of convergence is extended. In this way, the calculation with vector stop model is stabilized. With the Newton Method, ΔA_k of k[th] iteration is solved with the Jacobian matrix $J(A_k)$ and the residual $R(A_k)$:

$$J(A_k)\Delta A_k = -R(A_k) \tag{4}$$

The damped method with relaxation factor α in k[th] Newton iteration is formed as:

$$A_{k+1} = A_k + \alpha_k \Delta A_k, \quad \alpha_k \in (0,1]. \tag{5}$$

The natural monotonicity test is error oriented and the error $\|A_{k+1} - A_s\|$ is expected to fall monotonically (6)

$$\|A_{k+1} - A_s\| \leq \theta \|A_k - A_s\|, \tag{6}$$

where $\theta < 1$, A_s is the solution. The error $\|A_k - A_s\|$ can be approximatly calculated with the term:

$$\|J(A_k)^{-1}(R(A_k) - R(A_s))\| = \|J(A_k)^{-1}R(A_k)\|. \tag{7}$$

The θ is chosen as $1 - \frac{\alpha_k}{2}$. Thus, equation (6) can be rewritten as (8) by using equation (5) and (7):

$$\left\|J(A_k)^{-1}R\left(A_k + \alpha_k^i \Delta A_k\right)\right\| \leq \left(1 - \frac{\alpha_k^i}{2}\right)\|J(A_k)^{-1}R(A_k)\| \tag{8}$$

For the i[th] damped step, if the monotonicity test (8) fulfills, the damped process is stopped and α_k^i is set into (5) to calculate the A_{k+1}. For the next Newton iteration, the damped factor starts with $\min\{\alpha_{k+1}^1 = \alpha_k^i \times 2, 1\}$ in order to accelerate the convergence. If (8) fails, α is updated further with (9):

$$\alpha_k^{i+1} = \frac{\alpha_k^i}{2} \tag{9}$$

In order to illustrate the convergence process of damped Newton by simulation with vector hysteresis stop model, the error $\|A_k - A_s\|$ is considered as object function and the residual of the linear equation system is calculated in each damped step. The development of the object function against the α is shown in . The maximum number of damped steps is set to 20. With the monotonicity test (6), the optimal α can be found at 4th step. With this optimum the error $\|A_k - A_s\|$ is minimized as well as the norm of the residual.

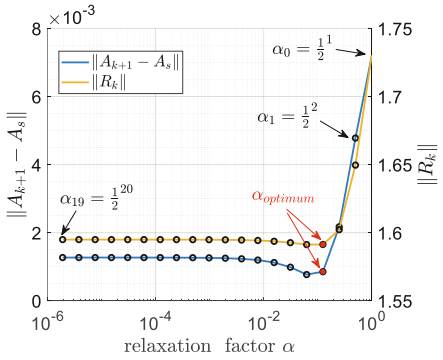

Figure 3. The development of the error and the $\|R_k\|$ against the relaxation factor α by a second time step and 6[th] Newton iteration. The found optimal relaxation factor is 0.125 at 4[th] damped iteration.

Another line search method based on the Wolfe Powell conditions is also used to solve the field problem with consideration of anisotropic vector hysteresis effects, which will be illustrated in the full paper detailed.

IV. CONCLUSIONS

In this paper a relaxation method is proposed in combination with an improved differentiation of the vector stop model to ensure convergence. The presented approach stabilizes the Newton Method on a global scale and presents a further step into accurate consideration of ferromagnetic hysteresis effects in the magnetic analysis of e.g. electrical machines.

V. ACKNOWLEDGMENT

Thanks to Dr. Klaus Kuhnen of Robert Bosch GmbH for sharing his experiences in hysteresis modeling. The German Research Foundation (DFG) supported this work within the research project number 373150943 “Vector hysteresis modeling of ferromagnetic materials”.

REFERENCES

[1] A. Chama, S. Gerber and R. Wang, “Newton–Raphson Solver for Finite Element Methods Featuring Nonlinear Hysteresis Models,” *IEEE Transactions on Magnetics,* vol. 54, no. 1, pp. 1-8, January 2018.

[2] R. Mitsuoka, T. Mifune, T. Matsuo and C. Kaido, “A Vector Play Model for Finite-Element Eddy-Current Analysis Using the Newton-Raphson Method,” *IEEE Transactions on Magnetics,* vol. 49, no. 5, pp. 1689-1692, May 2013.

[3] E. Dlala, A. Belahcen and A. Arkkio, “A Fast Fixed-Point Method for Solving Magnetic Field Problems in Media of Hysteresis,” *IEEE Transactions on Magnetics,* pp. 1214-1217, 2008.

[4] K. Fujiwara, T. Nakata, N. Okamoto and K. Muramatsu, “Method for determining relaxation factor for modified Newton-Raphson method.,” *IEEE Transactions on Magnetics,* vol. 29, no. 2, p. 1962–1965, 1993.

[5] C. Guérin, K. Jacques, R. V. Sabariego, P. Dular, C. Geuzaine and J. Gyselinck, “Using a Jiles-Atherton vector hysteresis model for isotropic magnetic materials with the finite element method, Newton-Raphson method, and relaxation procedure.,” *The International Journal of Numerical Modelling,* vol. 30, no. 5, 2017.

[6] D. Peter, Systems of Equations: Global Newton Methods. In: Newton Methods for Nonlinear Problems. Springer Series in Computational Mathematics, v. 35., Ed., Springer, Berlin, Heidelberg., 2011.

[7] J. V. Leite, N. Sadowski, P. Kuo-Peng and J. P. A. Bastos, “a new anisotropic vector hysteresis model based on stop hysterons,” *IEEE Transaction on magnetics,* vol. 41, no. 5, pp. 1500-1503, May 2005.

EFFICIENT HIGH-RESOLUTION ELECTRIC FIELD SIMULATIONS INSIDE THE HUMAN BODY IN THE VICINITY OF WIRELESS POWER TRANSFER SYSTEMS WITH VARYING MODELS

Norman Haussmann, Robin Mease, Martin Zang, Hendrik Hensel, Steven Stroka, Markus Clemens

University of Wuppertal, Chair of Electromagnetic Theory
Gaußstraße 20, 42119 Wuppertal, Germany, e-mail: haussmann@uni-wuppertal.de

***Abstract* – Monolithic electromagnetic exposure simulations of human models in the vicinity of inductive charging systems for electrically powered vehicles can be computationally expensive, especially if the body of the vehicle has to be considered as well. To overcome this problem, the Scaled-Frequency Finite Difference Time Domain (SF-FDTD) scheme can be used. To facilitate simulations with several exposed bodies in different postures the Co-Simulation Scalar Potential Finite Difference scheme can be utilized. This scheme can be applied to extract the magnetic fields from a monolithic SF-FDTD simulation. This allows not only faster simulation times, but also an increased automatization with a decreased simulation time.**

I. INTRODUCTION

To simplify the charging process of batteries of electrically powered vehicles wireless power transfer (WPT) systems can be utilized. WPT systems are driven by low-frequency currents in the primary coil emanating low-frequency magnetic fields. These fields are guided by ferrite stripes and shielded by aluminum plates. However, stray magnetic fields escape from the WPT systems and are additionally influenced by the car body. These fields can potentially be harmful to humans close to the WPT system. Limits given by the International Commission on Non-Ionizing Radiation Protection (ICNIRP) [1] on the induced electric field strength into the human body cannot be measured directly but require numerical simulations. These simulations can be computationally expensive as they contain the WPT system, the car body and human models. A two-step approach called the Co-Simulation Scalar Potential Finite Difference scheme (Co-Sim. SPFD) [2] can be used to disentangle the simulation of the magnetic field in the simulation space from the exposure of the human body since its low electric conductivity has a negligible attenuating effect on the magnetic source field.

This work efficiently combines monolithic Scaled-Frequency Finite Difference Time-Domain (SF-FDTD) [3] simulations with exposure simulations of several human models in different postures and positions to decrease simulation time, memory requirement and user workload.

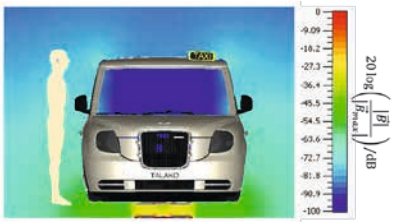

Fig.1. Example of a person exposed to a stray magnetic field from a WPT system in the TALAKO project (https://talako.uni-due.de/)

II. APPROACH

To determine the induced electric field strengths in human bodies in a monolithic simulation containing the WPT system, the vehicle and human models in different postures is computationally expensive. The WPT system and the shielding vehicle body require a fine resolution to get a good approximation of the expected magnetic fields. Including human voxel models with a resolution of 2x2x2 mm^3, according to the ICNIRP guidelines, in all necessary postures and positions to evaluate the exposure from a WPT system results in billions of mesh cells that quickly become unmanageable in monolithic simulations. Additionally, in monolithic simulations it is often not possible within commercial simulation packages to use several different human models in identical positions.

A. First Simulation Step

WPT systems are usually driven in a frequency range of tens of kHz leading to long simulation times with CST Microwave Studio [4]. To overcome this problem, the SF-FDTD scheme is used to perform monolithic simulations in the MHz frequency range. To obtain an equivalent magnetic field distribution the penetration depth of the fields must be identical at the original f and scaled frequency f': $\delta(f',\sigma') = \delta(f,\sigma)$ and the electrical conductivity is to be scaled accordingly $\sigma' \sim f / f'$.

The body internal electric field $\vec{E}_{body}$ needs to be scaled after the simulation finished to retrieve the electric fields at the original frequency

$$\vec{E}_{body}(f) = \frac{f}{f'} \cdot \frac{\sigma(f')}{\sigma(f)} \cdot \vec{E}_{body}(f'). \tag{1}$$

This work proposes a second simulation step to utilize the Co-Sim. SPFD scheme, that can be much faster, more convenient to use and resource-saving. A monolithic simulation with CST Microwave Studio at a higher scaled-frequency containing high resolution models of the WPT system and the vehicle body is performed without human models. The simulation space can be expanded to cover a volume that encloses all possible exposure positions while reducing the mesh-cell resolution in the surrounding space. Besides, as no human model is inside the simulation space the electric field values do not need to be stored.

From the monolithic simulation the magnetic field values can be exported to determine the body-internal electric field values at each position for any model and posture in the simulation space.

B. Second Simulation Step

The discrete Poisson system of linear equations of the SPFD scheme [5][6] using the notation of the finite integration technique FIT [7] is written as

$$G^T M_\sigma G \underline{\Psi} = -G^T M_\sigma \underline{\hat{a}} \tag{2}$$

with the discrete gradient operator G, the material matrix M_σ including the electrical conductivities, the vector of time integrals of the electric nodal potentials $\underline{\Psi}$ and the discrete vector of line integrals of the magnetic vector potentials $\underline{\hat{a}}$ derived from the discrete vector of magnetic facet fluxes

$$\underline{\hat{\hat{b}}} = C \underline{\hat{a}} \tag{3}$$

via the discrete curl operator C and the tree-cotree gauging technique [8]. By solving equation system (2) for $\underline{\Psi}$ the vector of electric grid voltages $\underline{\hat{e}}$ and therefore the voxel averaged electric field strength can be calculated

$$\underline{\hat{e}} = -j\omega \left[\underline{\hat{a}} + G \underline{\Psi} \right]. \tag{4}$$

Modern Graphics Processing Units (GPUs) offer sufficient memory and computing power to rapidly determine electric field strengths for high resolution body models. The magnetic field at the required position can be extracted from the monolithic SF-FDTD simulation for one model, body posture and position after another with an automated script; for this the user just needs to specify where the model is located in the simulation space.

TABLE I
RESULTS OF MONOLITHIC SF-FDTD SIMULATIONS

	Disk Space / GB	**Simulation Time / min**
Scenario	SF-FDTD	
1	**87.5**	**438**
2	**96.3**	**320**
3	**94.9**	**255**
4	**99**	**431**
Scenario	Co-Sim. SPFD	
1,2,3,4	**~2**	**<1**

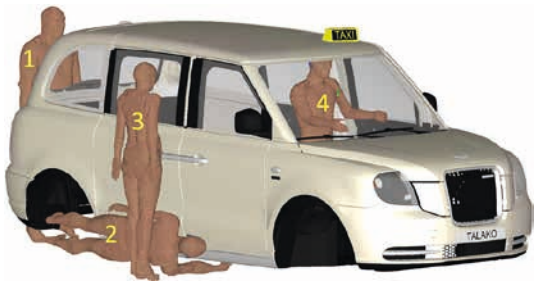

Fig.2. Different human body models in varying positions and postures labelled with the corresponding scenario number from Table 1.

III. RESULTS

Different exposure scenarios with several human body models in varying positions and postures are investigated (as visualized in Fig. 2.).

The goal is to determine the efficiency of the Co-Sim. SPFD scheme considering disk memory and simulation time. The results of monolithic SF-FDTD simulations including a single model are given in Table 1.

In contrast to the SF-FDTD scheme the Co-Sim. SPFD scheme requires approximately 2 GB of disk space to store the magnetic field data and less than a minute on modern GPUs to derive the body-internal electric field strengths. The monolithic SF-FDTD simulation for the exposure scenarios without the human models requires about 80 GB of disk space and 196 minutes of simulation time.

All simulations were performed on a high-performance computer with 8 NVIDIA Tesla V100 GPUs.

IV. CONCLUSION

Utilizing the Co-Sim. SPFD scheme showed a significant improvement in the required simulation time and disk space for varying exposure scenarios over monolithic simulations.

All magnetic field values could be extracted automatically, but sequentially from a SF-FDTD simulation using CST Microwave Studio with a Visual Basic script. This script proved to be beneficial for automatization, but also a bottleneck as the export of the magnetic field values took hours.

ACKNOWLEDGEMENTS

This work is supported by the German Federal Ministry for Economic Affairs and Climate Action (BMWK) under grants no. 01MZ19002B and 01MV21020A.

REFERENCES

[1] International Commission on Non-Ionizing Radiation Protection, "Guidelines for limiting exposure to time-varying electric and magnetic fields (1 Hz to 100 kHz)", *Health Phys.*, vol. 99, no. 6, pp. 818–836, 2010.

[2] M. Zang, et al., "A Co-Simulation Scalar-Potential Finite Difference Method for the Numerical Analysis of Human Exposure to Magneto-Quasi-Static Fields", *IEEE Tr. Magn.*, vol. 53, no. 6, pp. 1-4, 2017.

[3] O. P. Gandhi, J.-Y. Chen, "Numerical Dosimetry at Power-Line Frequencies Using Anatomically-Based Models," *Bioelectromagnetics Suppl. I*, pp. 43-60, 1992.

[4] CST Microwave Studio, Dassault Systèmes, Vélizy-Villacoublay Cedex, France.

[5] T. W. Dawson, et al., "Comparison of Magnetically Induced ELF Fields in Humans Computed by FDTD and Scalar Potential FD Codes", *ACES Journal*, vol. 11, pp. 63-71, 1996.

[6] T. W. Dawson, M. A. Stuchly, "Analytic Validation of a Three-dimensional Scalar-Potential Finite-Difference Code for Low-Frequency Magnetic Induction", *ACES Journal*, vol. 11, pp. 72–81, 1996.

[7] A Barchanski, et al., "Using domain decomposition techniques for the calculation of low-frequency electric current densities in high-resolution 3D human anatomy models", *COMPEL*, vol. 24, no. 2, pp. 458-467, 2005.

[8] R. Albanese, G. Rubinacci, "Magnetostatic field computations in terms of two-component vector potentials", *International Journal for Numerical Methods in Engineering*, vol. 29, no. 3, pp. 515-532, 1990.

INFLUENCE OF THE GEOMETRIC PARAMETERS OF A VERTICAL ROTATIONAL SINGLE SHEET TESTER ON SAMPLE FIELD HOMOGENEITY

Guilherme C. A. Tolentino*, Guillaume Parent*, Olivier Ninet*,
Mathieu Rossi*, Jean V. Leite† and Jonathan Blaszkowski‡

*Univ. Artois, UR 4025, Laboratoire Systèmes Électrotechniques et Environment (LSEE), F-62400, Béthune, France
†Universidade Federal de Santa Catarina, GRUCAD, Florianópolis, Santa Catarina, CEP: 88040-970, Brasil
‡Thyssenkrupp Electrical Steel, F-62330 Isbergues, France

***Abstract*—The horizontal Rotational Single Sheet Tester (RSST) suffers from weaknesses such as the reduced size of test samples, measurement disturbances due to magnetic flux leakage and non-homogeneity of field in the measurement area. Although the vertical RSST allows to overcome the first two aforementioned drawbacks, the heterogeneity of the field in the test sample remains an issue. Additionally, there is still a lack of device standardization to ensure test repeatability, as already is well established with the Epstein frame. In this paper, a finite element model of this device is developed in order to investigate the influence of several parameters on the field homogeneity in the test sample, such as the geometrical dimensions of the yokes and the presence of holes drilled for B-coil placement. It is expected that this study will contribute to the optimization and standardization these devices.**

I. INTRODUCTION

The vertical RSST has been introduced in the early 90s [1] but is still under consideration in recent publications [2]–[4]. According to the literature, the advantages of this setup compared to the horizontal RSSTintroduced in the 80s are numerous [5]. Firstly, its ease of implementation due to similarities to the standardized Single Sheet Tester (SST). Secondly, a better homogeneity of both magnetic field **H** and magnetic flux density **B** at the center of the test sample is expected [6]. Thirdly, higher flux density levels can be reached in the test sample than with the horizontal SST [2]. It has to be noted that each publication related to that device brings its own setup in terms of numbers and dimensions of the yokes as well as on dimensions of the sensors [7], [8], denoting the lack of standardization of structure and measurement system. Nevertheless, the trend emerging from all those publications is that the larger the width of the yokes the better. Indeed, in [9] the authors evaluate the accuracy of miniature SSTs dedicated to the characterization of small size test samples and highlight that the difference with the results obtained using an Epstein frame can be up to 5 %. The same trend is highlighted on vertical RSSTs in [7], [8]. Moreover, large yokes allow to "eliminate the influence of the demagnetizing field" [10], leading to a better characterization of large test samples [1]. However, the standard relative to the regular SST allows the use of yokes of any size "as long as the relevance of the results is ensured" [11]. To the authors' knowledge, almost no quantitative study of the influence of those parameters on the field homogeneity in the measurement area has been published except in [7], [8] in which the focus is made on the deflection of the mean value at the center of the test sample only. Above all, in all of the aforementioned studies, no link is made between the field non-homogeneity in the test sample and the actual field values that would be measured with actual sensors, which is after all the key point when characterizing a material. In particular, none of those works takes into account that the sensors employed to evaluate **H** and **B** are not of the same dimensions nor do they account for the fact that the more often **B** is evaluated by means of a coil requiring to drill the test sample. Yet, there is no doubt those holes have a great influence on field homogeneity.

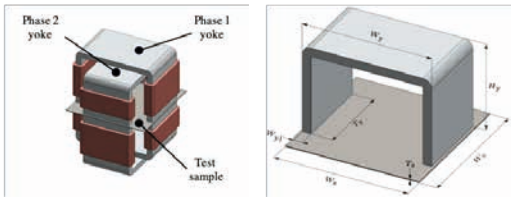

(a) Topology of the studied vertical RSST

(b) Dimensions of the test sample and a half of a yoke

Fig. 1. Studied vertical RSST

II. TOPOLOGY OF THE STUDIED VERTICAL RSST AND FINITE ELEMENT MODEL

An overview of the topology of the studied vertical RSST is presented in Fig. 1a. It is composed of two magnetic yokes, i.e. one per phase. Each yoke consists of two C-shape cores (see Fig. 1b) arranged along each side of the test sample. Due to geometrical constraints and for the sake of magnetic balance between the two yokes, the two cores share every dimensions W_{yl}, W_y and T_y but the height H_y. The test sample is square with side and thickness denoted W_s and T_s respectively. All dimensions are summarized in table I.

The finite element simulations are conducted using the softwares GMSH and GetDP. The model is fully 3D and the problem is solved by means of the magnetostatic scalar potential formulation. Moreover, the nonlinear behavior of the test sample is taken into account by means of its first magnetization curve.

III. SOME RESULTS

In the following, the test sample is made of M260 electrical steel whose first magnetization curve is presented in Fig. 2. Moreover, for the sake of relevance of the analysis, only the worst case in terms of field homogeneity in the test sample,

TABLE I
DIMENSIONS OF THE VERTICAL RSST

Name	Value
W_s	300 mm
T_s	0.35 mm
W_{yl}	20 mm
W_y	290 mm
H_y	150 mm (Small core) or 200 mm (Tall core)
T_y	Varies between 75 mm and 200 mm

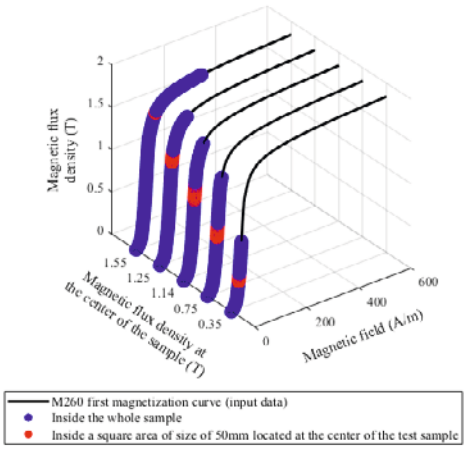

Fig. 2. Distribution of **H** and **B** inside different areas of the test sample.

that is the case in which the latter is magnetically excited along its diagonal, is considered and presented.

A. *Field homogeneity inside the test sample*

Fig. 2 shows the values of both **H** and **B** occurring in different areas of the test sample for different levels of magnetization and with $T_y = 200\,\mathrm{mm}$. The first magnetization curve of M260 steel is also shown for information purpose. It can immediately be noted on this figure that both **H** and **B** inside the whole test sample, shown in blue, are widely heterogeneous due its large size. One might consider that this is not so much an issue since an actual sensor would only cover a small area of the test sample. Indeed, the red marks in Fig. 2 show the values of **H** and **B** occurring in a square area with a size of 50 mm located at the center of the latter. It clearly highlights that even inside a limited are the heterogeneity is still noticeable. Moreover, the mean values of **H** and **B**, which correspond to the values that would be given by an actual sensor, do not match the ones at the center of the test sample.

B. *Influence of the core length T_y*

The values of **H** and **B** inside a square area with a size of 50 mm located at the center of the test sample with respect to T_y are represented as box and whisker plots in Fig. 3. T_y varies from 75 mm to 200 mm in increments of 25 mm and the magnetization level is such that $\|\mathbf{B}\| = 0.75\,\mathrm{T}$ at the center of the test sample. The first thing that can be noticed in this figure is that outliers are always present whatever the value of T_y. There is no doubt those outliers have an influence on the value given by actual sensors. The second thing is that the homogeneity of both **H** and **B** increases with T_y. Nevertheless, Fig. 3 also highlights that as soon as T_y is superior to half the width of the test sample the results are much the same.

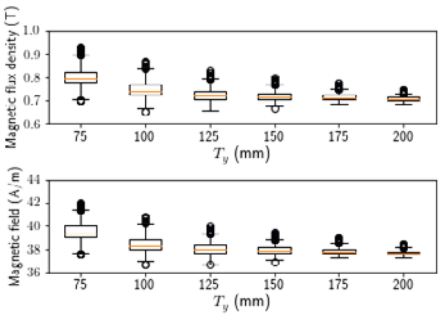

Fig. 3. The values of the potential vectors of **H** and **B** under the statistical box plot analysis, obtained by FEM simulation inside a square area of size of 50 mm located at the center of the test sample with respect to T_y. $\|\mathbf{B}\| = 0.75\,\mathrm{T}$ at the center of the test specimen.

IV. CONCLUSION AND OUTLOOKS

The accuracy of the results given by a vertical RSST largely depends on its dimensions as well as on the dimensions of the sensors used for the measurements. In the final paper, the study of the field homogeneity inside limited areas presented in Section III-A will be extended to different size and shape for the sake of comprehensiveness and relevance with respect to actual sensors. As an example, an H-coil is usually square but a B-coil is not. Moreover, the study of the influence of T_y will also be extended to different magnetization levels. It will be shown that the higher T_y the better the accuracy of the measurement has to be weighted to the magnetization level as well as the size of the sensors. Finally, the influence of drilled wholes, which are required to place a B-coil in the test sample, will also be addressed.

REFERENCES

[1] J. Sievert, H. Ahlers, M. Enokizono, S. Kauke, L. Rahf, and J. Xu, "The measurement of rotational power loss in electrical sheet steel using a vertical yoke system," *J. Magn. Magn. Mater.*, vol. 112, no. 1-3, pp. 91–94, Jul. 1992.

[2] K. Fonteyn and A. Belahcen, "Numerical and experimental results from a vertical yoke system for measuring magnetic properties of Fe-Si steel sheets," in *Proc. of the 11th Int. Conf. on Electr. Mach. and Syst. (ICEMS)*, Wuhan, China, Oct. 2008, pp. 434–438.

[3] A. Li, Y. Li, C. Zhang, Q. Yang, and J. Zhu, "Design of a novel high frequency 2-D magnetic tester with nanocrystalline material," in *Proc. Int. Conf. Electr. Mach. and Sys. (ICEMS)*, Oct. 2017, pp. 1–5.

[4] S. Yue, Y. Li, Q. Yang, K. Zhang, and C. Zhang, "Comprehensive investigation of magnetic properties for Fe-Si steel under alternating and rotational magnetizations up to kilohertz range," *IEEE Trans. Magn.*, vol. 55, no. 7, pp. 1–5, Jul. 2019.

[5] W. Brix, "Measurements of the rotational power loss in 3% silicon-iron at various frequencies using a torque magnetometer," *J. Magn. Magn. Mater.*, vol. 26, no. 1-3, pp. 193–195, Mar. 1982.

[6] O. de la Barriere, C. Appino, C. Ragusa, F. Fiorillo, M. LoBue, and F. Mazaleyrat, "1-D and 2-D loss-measuring methods: optimized setup design, advanced testing and results," *IEEE Trans. Magn.*, vol. 54, no. 9, pp. 1–15, Sep. 2018.

[7] N. Nencib, A. Kedous-Lebouc, and B. Cornut, "3D analysis of a rotational loss tester with vertical yokes," *J. Magn. Magn. Mater.*, vol. 133, no. 1-3, pp. 553–556, May 1994.

[8] ——, "Performance evaluation of a large rotational single sheet tester," *J. Magn. Magn. Mater.*, vol. 160, pp. 174–176, Jul. 1996.

[9] M. De Wulf, D. Makaveev, Y. Houbaert, and J. Melkebeek, "Design and calibration aspects of small size single sheet testers," *J. Magn. Magn. Mater.*, vol. 254-255, pp. 70–72, Jan. 2003.

[10] S. Tumanski, *Handbook of Magnetic Measurements*, 1st ed. CRC Press, 2011.

[11] "IEC60404: Magnetic materials - Part 3: Methods of measurement of the magnetic properties of magnetic sheet and strip by means of a single sheet tester," International Electrotechnical Commission, Tech. Rep., 1992.

HEATING OF FIBER-BASED MAGNETIC SCAFFOLDS FOR HYPERTHERMIA APPLICATIONS: MAINTAINING SIMULATION ACCURACY WITH REDUCED MODEL COMPLEXITY

Karl Schneider, Ioana Slabu

*RWTH Aachen University and University Hospital Aachen, Institute of Applied Medical Engineering
Pauwelstraße 20, D-52074 Aachen, Germany, e-mail: slabu@ame.rwth-aachen.de

***Abstract* – In this study, we analyze the heating of fiber-based magnetic scaffolds with two 3D simulation models. The scaffolds can be used in a myriad of clinical applications such as hyperthermia cancer treatment and targeted drug delivery. One model consists of a nanomodified polypropylene fiber with embedded magnetic nanoparticles as a volumetric heat source, while the other of a non-nanomodified fiber with a surface heat source significantly reducing simulation model complexity. We demonstrate that the two simulation approaches deliver similar results and that the error due to reduced complexity is less than the error due to uncertainty in the material property values.**

I. INTRODUCTION

Magnetic nanoparticles (MNPs) embedded in a polymer matrix, called magnetic scaffolds, enable a myriad of clinical applications hyperthermia cancer therapy or targeted drug delivery. MNPs exposed to an alternating magnetic field generate heat through non-linear magnetic relaxation processes. Accurate knowledge of temperature distribution around the magnetic scaffold is necessary for safe and effective therapy. Simulations of the heating process of the magnetic scaffolds allow a comprehensive study of the parameters influencing the heating process as well as a prediction of temperature distribution near the fiber-based magnetic scaffold.

In this study, we investigate the temperature distribution of a magnetic fiber using two different simulation approaches and analyze the potential loss of accuracy with a less complex simulation approach.

II. MATERIALS AND METHODS

Model A, as shown in Fig. 1, consists of a polypropylene (PP) nanomodified fiber ring with a circular cross-section and embedded MNPs. The fiber is fully covered in agarose. Compared to model A, model B consists a non-nanomodified PP fiber. For model A, the MNPs are modeled as homogenously distributed macroscopic clusters, which are placed equidistant along the centerline of the PP fiber. The characteristics of the modeled MNPs are based on [1, 2], table 1 summarizes the main parameters.

In model A, the MNPs are modeled as volumetric heat sources with the specific heating power given by the following expression:

$$Q_{volumetric} = \frac{SLP \cdot m_{Fe_3O_4}}{V_{MNP}} \quad (1)$$

where SLP [W g^{-1}] is the specific loss power, $m_{Fe_3O_4}$ [kg] the amount of magnetite per MNP cluster and V_{MNP} [m^3] the volume of the MNP cluster.

TABLE I
MAIN PARAMETERS OF THE MODELS

Parameter	value	unit
SLP	200	W g^{-1}
MNP volume	1,38·10^{-3}	mm^3
PP fiber radius	0,3	mm
PP fiber ring radius	2,8	mm
Agarose volume	619,23	mm^3

In model B, the volumetric heat source of the model A is replaced by a surface heat source of the PP fiber equal to the average heat flux through the surface of the PP fiber as calculated in model A. No further data from model A is necessary to compute model B.

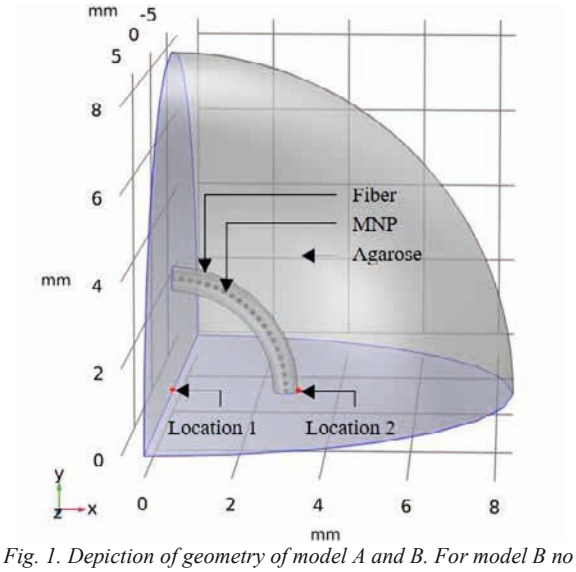

Fig. 1. Depiction of geometry of model A and B. For model B no MNPs are embedded in the fiber.

Heat transfer in both models is described by the following equation:

$$\rho c_p \frac{\partial T}{\partial t} + \nabla \cdot (-k \nabla T) = Q \quad (2)$$

where ρ [kg m^3] is the density, c_p[J kg^{-1} K^{-1}] the heat capacity at constant pressure, k [W m^{-1} K^{-1}] the thermal conductivity, T [K] the temperature, and Q [W] the heat input.

A Dirichlet boundary condition is used to set the temperature of the outer surface of the agarose to 37 °C. Symmetry conditions (equation 3) are applied on the boundaries along the x and y axis (highlighted in blue in Fig. 1).

$$-\vec{n} \cdot \vec{q} = 0 \quad (3)$$

where $\vec{n}$ is the outwards-facing normal vector, and $\vec{q}$ [W m^{-2}] the heat flux.

There is no reliable information available about the thermal conductivity of agarose in the literature. As such two values for the thermal conductivity of agarose are used, one linearly dependent on temperature and agar concentration, and one constant [2, 3].

The resulting temperature distributions are analyzed along the fiber surface for the stationary case as well as at two locations for the time dependent case. Location 1 is in the center of the nanomodified fiber ring and location 2 is on the surface of the fiber (highlighted in red Fig. 1).

Simulations were performed using the software COMSOL Multiphysics® version 5.6 with the *heat transfer in solids* module. Both models were meshed using a physics-controlled mesh with the extra fine element preset.

The resulting meshes have a minimum and average quality of 0.2017 and 0.662 (model A), and 0.2017 and 0.6712 (model B), respectively.

III. RESULTS AND DISCUSSION

Fig. 2 shows the temperature values for the locations 1 and 2 for the time dependent simulations. The average temperature differences between the models is only -0.0026 K ±0.012 K, demonstrating accuracy of model B.

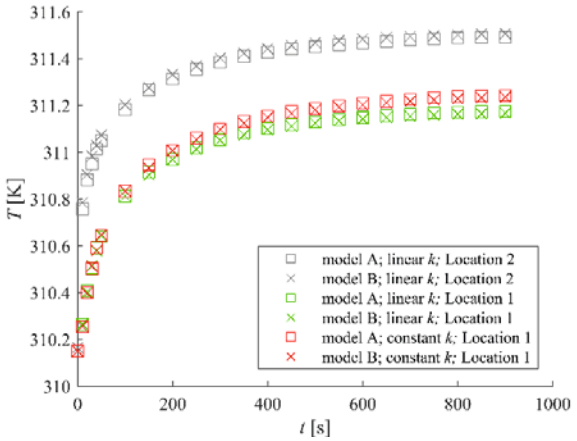

Fig. 2. Temperature over time of select points in both models

The minimum, maximum, mean, average, and interquartile ranges of the stationary surface temperature of the fiber for both models A and B are displayed in Fig. 3. With model A and for the linear thermal conductivity of agarose, the fiber surface temperature distribution resulted an interquartile range of 0.16 K from 311.52 K to 311.68 K, a maximum temperature of 311.72 K, and a minimum temperature of 311.49 K. Stationary simulations using the constant thermal conductivity resulted in an interquartile range of 0.17 K from 311.62 K to 311.79 K, a maximum temperature of 311.83 K, and a minimum temperature of 311.60 K.

The approximation of the volumetric heat source by a surface heat source (using the average heat flux through the surface of the fiber derived from model A of 740 W m^{-2}) results in a more homogenous temperature distribution. The interquartile range using the linear thermal conductivity of 0.14 K (first quartile: 311.54 K; second quartile: 311.67 K) is 0.02 K lower compared to model A. The maximum and minimum temperature is 0.02 K lower and higher, respectively. Resulting temperatures are close to experimental results independent of the model used [2]. For validation, experiments are envisaged.

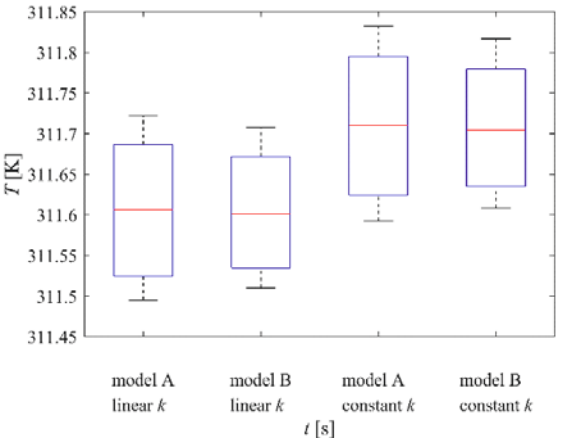

Fig. 3. Boxplot of the surface temperature of the fiber for stationary simulations with models A and B for different thermal conductivities of agarose.

IV. CONCLUSIONS

For calculation of the temperature distribution of a magnetic fiber, we showed that the accuracy can be maintained with limited model complexity. Fig. 2 and Fig. 3 demonstrate that the error due to the uncertainty in the thermal conductivity is larger than the error due to the reduction of model complexity. Therefore, the use of the less complex model is justified for future simulations.

V. ACKNOWLEDGMENTS

We would like to acknowledge and thank Lucas Theelen for preliminary simulations of heat generation with magnetic scaffolds.

REFERENCES

[1] Mues, B.; Bauer, B.; Ortega, J.; Buhl, E. M.; Teller, H.; Gries, T.; Schmitz-Rode, T.; Slabu, I. “Assessing hyperthermia performance of hybrid textile filaments: The impact of different heating agents.” *Journal of Magnetism and Magnetic Materials* 2021, Volume 519, 167486, DOI:10.1016/j.jmmm.2020.167486

[2] Mues, B.; Bauer, B.; Roeth, A. A.; Ortega, J.; Buhl, E. M.; Radon, P.; Wiekhorst, F.; Gries, T.; Schmitz-Rode, T.; Slabu, I. “Nanomagnetic Actuation of Hybrid Stents for Hyperthermia Treatment of Hollow Organ Tumors.” *Nanomaterials* 2021, 11 (3): 618. DOI: 10.3390/nano11030618

[3] Zhang, M.; Che, Z.; Chen, J.; Zhao, H.; Le Yang; Zhong, Z.; Lu, J. “Experimental Determination of Thermal Conductivity of Water−Agar Gel at Different Concentrations and Temperatures.” *J. Chem. Eng. Data* 2011, 56 (4), 859–864. DOI: 10.1021/je100570h

[4] Soto-Reyes, N.; Temis-Pérez, A. L.; López-Malo, A.; Rojas-Laguna, R.; Sosa-Morales, M. E. “Effects of shape and size of agar gels on heating uniformity during pulsed microwave treatment.” *Journal of food science* 2015, 80 (5), E1021-5. DOI: 10.1111/1750-3841.12854

POWER DENSITY IMPROVEMENT OF AXIAL FLUX PERMANENT MAGNET SYNCHRONOUS MOTOR BY USING DIFFERENT MAGNETIC MATERIALS

Mohamed Amine Hebri[1*], Abderrahmane Rebhaoui[1,2], Grégory Bauw[1], Jean-Philippe Lecointe[1], Stéphane Duchesne[1], Gianluca Zito[3], Abdenour Abdelli[3], Vincent Mallard[4] and Adrien Maier[5]

[1]Univ. Artois, UR 4025, Laboratoire Systèmes Electrotechniques et Environnement, Béthune, F-62400, France
e-mail: mamine.hebri@univ-artois.fr
[2]VEDECOM - Versailles, 78000, France
[3] IFP Energies Nouvelles, Rueil-Malmaison, 92852, France.
[4]CRITT M2A, Bruay-la-Buissière, 62700, France
[5]EREM - Etudes Réalisations Et Maintenance, Wavignies, F-60130, France

***Abstract* - This paper presents a power density improvement of a yokeless dual-rotor axial flux permanent magnet synchronous motor. This study is based on the use of different materials for the stator and rotor magnetic circuits: Si-Fe non-oriented grain electrical steel (NOES), Si-Fe grain-oriented electrical steel (GOES), and Iron-Cobalt permendur (Co-Fe) electrical steel. The aim is to use these magnetic materials at their maximum peak performance in terms of magnetization and losses with the aim to reduce the geometrical dimensions of the magnetic circuits, stator teeth and rotor yokes.**

I. Introduction

In the context of the strong development of electric vehicles, the objective is to improve the efficiency of the powertrain in order to increase the autonomy of full electric cars and to reduce the environmental impact of hybrid cars, in view of the new European regulations on the limitation of CO_2 emissions [1]. The efficiency improvement involves to reduce losses in each element of the traction chain, as well as reducing its mass. This paper is focused on the electric motor part by improving its efficiency and power to mass ratio.

In automotive traction applications, the radial flux Permanent Magnet Synchronous Motors (PMSMs) are generally used due to its high-power density, high efficiency, compact size, and manufacturing simplicity. Axial flux PMSMs are good candidate as their power density may be even higher.

To further improve the power density of the axial flux PMSMs [2], the current density can be increased but it is limited by the thermal constraints and the cooling system. Permanent magnets with very high energy density can also be used as well as new magnetic materials with high permeability and high saturation flux density [3-4].

In this paper, the modification of the magnetic circuit materials for a yokeless dual-rotor axial flux PMSM is studied. Conventionally, electric motors for automotive applications are designed with 3% non-oriented grain electrical steel (NOES), which are well suited for rotating field applications. In this paper, other magnetic materials is analysed as grain-oriented electrical steel (GOES) which is commonly used in the manufacture of power transformers [3], as well as Permendur FeCo, which is commonly used in aeronautical applications in order to take advantage of their high saturation flux density, about 2.2T. This high level of saturation allows to reduce the size of the stator tooth and rotor yoke. That leads to a power density gain for the motor at iso-torque.

II. Magnetic Materials

The Fig. 1 shows the B-H curves for the three magnetic materials used in this study: NOES, GOES and the Permendur Hiperco50, which thicknesses 0,20mm, 0,20mm and 0.15mm respectively. The measurements are obtained with a standardised Single Sheet Tester (SST) frame at 50 Hz.

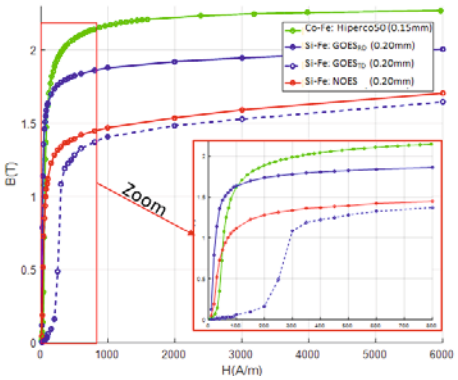

Fig.1. B-H curves of different magnetic materials

The curves show that the GOES sheet magnetized along the Rolling Direction (RD) has a very high permeability and a higher saturation knee, compared to the conventional NOES sheet. On the other hand, GOES is highly anisotropic, which means that the performances in the Transverse Direction (TD) are much less interesting. Furthermore, the Permendur Hiperco50 sheet has a very high saturation flux density value compared to the conventional NOES sheet and the GOES sheet (Table I).

TABLE I
MAGNETIC PROPERTIES

	Saturation flux density	Maximal relative permeability	Mass density
Si-Fe - NOES	1,8 T	14500	7650 kg/m^3
Si-Fe - GOES	2,0 T	31500	7650 kg/m^3
Co-Fe : Hiperco50	2,2 T	15600	8120 kg/m^3

III. Design Approach

The studied axial flux dual-rotor and yokeless PMSM is shown in Fig. 2. The general parameters are presented in Table II. The design concept of our motor is to saturate the tooth at the minimum radius during the rated operation point, subsequently

the whole teeth are magnetized in the highest part of BH knee during the peak operation point.

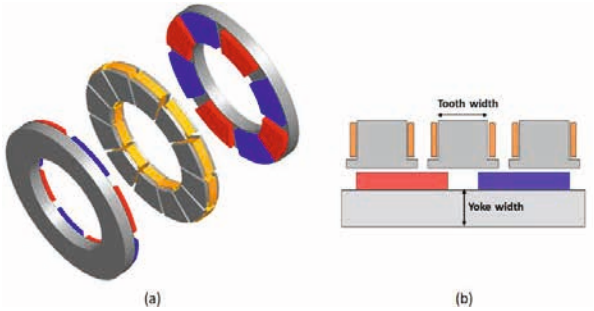

Fig.2. The PMSM structure studied: a) in 3D, b) in 2D at average radius

TABLE II
MOTOR PARAMETERS

Slot / Pole number	12 / 8
Inner / Outer radius	60mm / 100mm
Base rotational speed	10000rpm
Number of series turns per phase	60
Rated current	130Arms
Airgap	1.3mm
Magnet width	6.5mm

In order to simplify the study and the modelling, the authors use a 2D structure of the axial flux PMSM at the average radius. The 3 magnetic materials described above (Fig.1) are combined in the stator teeth and the rotor yoke, which lead to 9 configurations of magnetic circuits, as described in Table III.

TABLE III
COMBINATIONS FOR THE MAGNETIC CIRCUIT

Structures	Tooth material	Yoke material
Tn-Yn	NOES	NOES
Tn-Yg	NOES	GOES
Tn-Yh	NOES	Hiperco50
Tg-Yn	GOES	NOES
Tg-Yg	GOES	GOES
Tg-Yh	GOES	Hiperco50
Th-Yn	Hiperco50	NOES
Th-Yg	Hiperco50	GOES
Th-Yh	Hiperco50	Hiperco50

In the analyse, the yoke width and the tooth width are modified, respecting the necessary slot area for the conductor arrangement, as well as the saturation levels of the sheets. The aim is to find the optimal dimensions for a high-power density in the power range between 90kW and 105kW at the base rotational speed and the rated current.

IV. FEA-2D RESULTS

The power densities for four out of nine structures (Table III) are shown in Figure 3: full NOES reference structure, full GOES structure, full Hiperco50 structure, and a mixed structure with GOES teeth and Hiperco50 yoke. The maximum power density of the reference structure is 9.39kW/kg with a 24mm tooth width and a 12mm yoke width, considering only the active parts in the calculation of the weight.

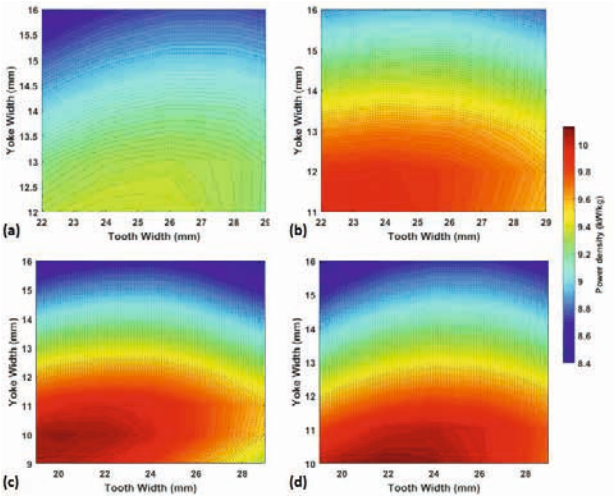

Fig.3. Variation of power density as a function of the tooth-width and the yoke-width for: a) Tn-Yn, b) Tg-Yg, c) Th-Yh, d) Tg-Yh

The results show that the full Hiperco50 structure improves the power density by 7.4%, compared to the reference structure. The full GOES structure, with RD according to the axial direction in teeth and tangential direction in yoke, also improves the power density by 5.8%, compared to the reference structure. In addition, the mixed structure with GOES teeth and Hiperco50 yoke offers a better gain in power density about 7.7%, compared to the reference structure, due to the very high permeability of the GOES sheet and the very high flux density of the Hiperco50.

V. CONCLUSION

This study shows that the use of non-conventional magnetic materials (Hiperco50 and GOES) in the different parts of the magnetic circuit (teeth and yoke) allows to increase the power density of our axial flux PMSM. The mixed structure (Tg-Yh) and full Hiperco50 structure (Tg-Yh) give the best results in terms of power density. In the full paper, the results about the nine possible combinations mentioned above will be presented with the calculation of the efficiency. In the next work, a FEA-3D study will be performed.

REFERENCES

[1] D. Auverlot, N. Meilhan, B. Mesqui and A. Pommeret, Les politiques publiques en faveur des véhicules à très faibles émissions, France stratégie, 2018, CID: 20.500.12592/35cbsx.
[2] J.Pyrhonen, T.Jokinen and V.Hrabovcova, Design of Rotating Electrical Machines (Second Edition), Wiley, 2014, DOI:10.1002/9780470740095.
[3] A. Rebhaoui, S. Randi, C. Demian and J.-P. Lecointe, «Analyse of Flux Density and Iron Loss Distributions in Segmented Magnetic Circuits Made with Mixed Electrical Steel Grades,» *IEEE Transactions on Magnetics (Early Access),* 2021, DOI : . 10.1109/TMAG.2021.3138984.
[4] A. S. Nagorny, N. V. Dravid, R. H. Jansen, and B. H. Kenny, "Design aspects of a high speed permanent magnet synchronous motor / generator for flywheel applications," in IEEE International Conference on Electric Machines and Drives, 2005, pp. 635–641, DOI : 10.1109/IEMDC.2005.195790.

DETERMINATION OF A DC MOTOR'S PARAMETERS BASED ON THE ANGULAR SPEED AND CURRENT RESPONSE

Marko Jesenik, Anton Hamler, Mislav Trbušić

Faculty of Electrical Engineering and Computer Science, University of Maribor
Koroška cesta 46, 2000 Maribor, Slovenia, e-mail: marko.jesenik@um.si

***Abstract* – A method is presented for the determination of the direct current (DC) motor and drive. The basis for the parameters` determination are speed and current startup responses. The method can be used in the case of controlled drive. Differential Evolution (DE) is used for the parameters` determination. The motor's model simulation, which is used for the Objective Function calculation, is described with two coupled Differential Equations. The Runge-Kutta fourth order method is used for the solving of the system of two cupled Differential Equations.**

I. INTRODUCTION

Drives with Direct Current motors (DC motors) are used widely in industrial applications. They are often used for industry control systems, because they are easy to control. Often DC motor's and also a drive's parameters are not known, or the motor's parameters provided by the motor manufacturer could have relatively large tolerances [1], especially for the cheaper DC motors. Also important are the drive's parameters, such as the inertia of the drive and friction. Usually the inertia and friction of all the drive's parts are not known.

II. DC MOTOR'S MODEL

The DC motor is presented schematically in Figure 1. A working machine may, or may not, also be connected to the motor.

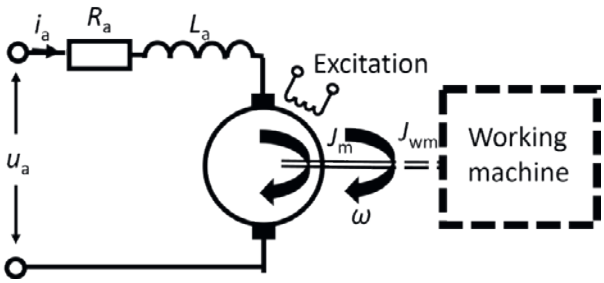

Fig.1. DC motor and working machine

R_a is the ohmic resistance of the DC motor, L_a is the inductance of the DC motor (we assume it is constant, which is a simplification of the model), u_a is the voltage at the DC motor, i_a is the current of the DC motor, J_m is the inertia of the motor ω angular speed at the axis of the motor, and J_{wm} is the inertia of the working machine.

Drive operation can be simulated using two coupled Differential Equations, written as (1) and (2). It is assumed that excitation is present before the connection of the motor's armature.

$$u_a = i_a \cdot R_a + L_a \cdot \frac{di_a}{dt} + e \tag{1}$$

$$T_m - T_{load} = J \frac{d\omega}{dt} \tag{2}$$

J is the inertia of all parts in the drive and e is the induced voltage. Equations (1) and (2) are coupled, because e depends on the angular speed ω and T_m depends on the current i_a, as written in (3) and (4).

$$e = c_m \cdot \omega \tag{3}$$

$$T_m = c_m \cdot i_a \tag{4}$$

c_m is assumed to be a constant, and it is called the motor's constant. T_{load} written in (2) is divided into more parts, written in (5).

$$T_{load} = T_{la} + T_{lb} \cdot \omega + T_{lc} \cdot \omega^2 \tag{5}$$

Rewriting (1) and (2), considering (3), (4) and (5), we obtain (6) and (7), which are the basis for the mathematical model.

$$u_a = i_a \cdot R_a + L_a \cdot \frac{di_a}{dt} + c_m \cdot \omega \tag{6}$$

$$c_m \cdot i_a - \left(T_{la} + T_{lb} \cdot \omega + T_{lc} \cdot \omega^2\right) = J \frac{d\omega}{dt} \tag{7}$$

Simulation of the motor's startup is made with numerical solving of the Differential Equations written in (6) and (7). A Runge-Kutta fourth-order method is used. Derivatives must be expressed for numerical solving. The current derivative is expressed from (6) and written in (8), and the speed derivative is expressed from (7) and written in (9).

$$\frac{di_a}{dt} = \frac{1}{L_a} \cdot \left(u_a - i_a \cdot R_a - c_m \cdot \omega\right) = f\left(t, i_a, \omega\right) \tag{8}$$

$$\frac{d\omega}{dt} = \frac{1}{J} \cdot \left[c_m \cdot i_a - \left(T_{la} + T_{lb} \cdot \omega + T_{lc} \cdot \omega^2\right)\right] = g\left(t, i_a, \omega\right) \tag{9}$$

III. METHOD FOR PARAMETERS` DETERMINATION

Parameters` determination (R_a, L_a, c_m, J, T_{la}, T_{lb} and T_{lc}) is based on the comparison of the measured current and speed response at startup with calculations based on the described mathematical model. We are using a direct approach for the inverse problem. Differential Evolution (DE) is used for parameters` determination [2,3]. The used strategy was DE/rand/1/exp, the used amplification of the differential variation was 0.6 and the used crossover probability was 0.8.

IV. RESULTS

The measured current and speed responses are made on a SIEMENS SIMOREG DC-Master drive. The measurement is made with the use of the "Trace" function, which is a part of the SIEMENS software. The startup of the motor is made using an n-control closed loop with the following data: t_{speed_up}=0 s, ω_{final}=126 s^{-1}, i_{a_limit}=11,44 A (110% of I_{a_rated}), no load, 87 measured points. To consider closed loop operation, voltage u_a is not a constant value, it is a measured value $u_a(t)$, which is used as input to the motor's model.

Different controller adjustments influence the motor's voltage, which represents input data to the motor model, with that in mind, the motor (drive) dynamic is fully considered by the presented model.

The Objective Function (OF) is defined as the square of differences between the input and simulated data written in (10).

$$OF = \frac{1}{N}\sum_{i=1}^{N}\left(\left(\frac{i_{a\_simulated\_i} - i_{a\_input\_i}}{i_{a\_input\_max}}\right)^2 + \left(\frac{\omega_{simulated\_i} - \omega_{input\_i}}{\omega_{input\_max}}\right)^2\right) \quad (10)$$

N is the number of points of the measured values.

The parameters` limits are set between 0 and 100 for R_a and L_a, between 0 and 5 for c_e, between 0 and 1 for J, between 0 and 20 for T_{la}, between 0 and $9.55\cdot10^{-2}$ for T_{lb} and between 0 and $4.56\cdot10^{-6}$ for T_{lc}. The population number is set to 70.

TABLE I
BEST (B), WORST (W), MEAN VALUE (M) OF THE OBJECTIVE FUNCTION AND STANDARD DEVIATION (SD) FOR THE 50 INDEPENDENT RUNS

OF	DE/rand/1/exp
B	$2.2531\cdot10^{-3}$
W	$2.2531\cdot10^{-3}$
M	$2.2531\cdot10^{-3}$
SD	0.0

Based on Table I, it can be seen that the calculation procedure is robust. The same results were obtained for each run of 50 independent runs.

The calculated parameters are presented in Table II.

TABLE I
KNOWN AND CALCULATED PARAMETERS

Parameter	Known value	Calculated value
R_a	5.66	5.06
L_a	not known	0.244
c_m	not known	1.369
J	≈ 0.04	0.0468
T_{la}	≈ 0.9	0.799
T_{lb}	≈ 0	$7.70\cdot10^{-18}$
T_{lc}	≈ 0	$8.00\cdot10^{-19}$

The measured and calculated responses are presented in Figure 2.

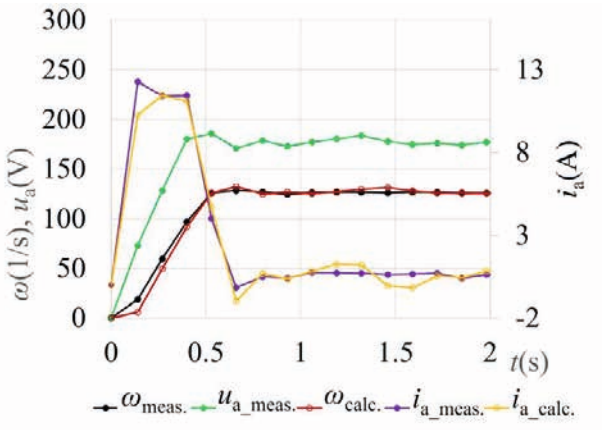

Fig.2. Measured and calculated values

V. CONCLUSIONS

From Table I it can be seen that chosen DE is a very robust and stabile optimisation method.

The calculated results presented in Table II show good agreement between the known and calculated parameters. The differences between the known and calculated values are approximately 11% in the case of R_a and T_{la}, and approximately 17% in the case of J. A good match between the measured and calculated time responses is evident in Figure 2, which confirms the quality of the presented method.

This work was supported by the Slovenian Research Agency under Grant P2-0114.

REFERENCES

[1] N.B. Shanmuga, A. Mythile, S. Pavithra, N. Nivetha, "Parameter Identification of A DC Motor", *International journal of scientific & technology research*, 2020, vol. 9 (2), pp. 5746-5755, 2020.

[2] R.J. He, Z.Y. Yang, "Differential evolution with adaptive mutation and parameter control using Levy probability distribution", *Journal of Computer Science and Technology*, vol. 27 (5), pp. 1035-1055, 2012.

[3] S. Chattopadhyay, S.K. Sanyal, "Optimization of Control Parameters of Differential Evolution Technique for the Design of FIR Pulse-shaping Filter in QPSK Modulated System", *Journal of* Communications, vol. 6 (7) pp. 558-570, 2011.

DESIGN AND ANALYSIS OF SIX-PHASE SYNCHRONOUS RELUCTANCE MOTOR

Cezary Jędryczka, Michał Mysiński

Poznań University of Technology, Institute of Electrical Engineering and Electronics
Piotrowo 3a, 61-138 Poznań, Poland, e-mail: cezary.jedryczka@put.poznan.pl, michal.mysinski@student.put.poznan.pl

***Abstract* - The paper presents research on the development of a six-phase synchronous reluctance motor (SynRM) based on the stator used in classical three-phase induction motors. In the design and calculation process, a extended Clarke-Park transform was developed for a six-phase asymmetrical system. To verify proposed design, a field-circuit model of electromagnetic phenomena in studied motor was developed. The conclusions resulting from conducted research as well as the goals of further work are discussed.**

I. INTRODUCTION

In this paper, an attempt has been made to develop a reluctance motor powered by a six-phase asymmetrical system. The stator core and a rotor with U-shaped flux barriers have been adopted from the four pole three-phase SynRM produced by ABB. Computer aided design tools were used to facilitate the analysis. The model developed in the Matlab Simulink environment allowed confirming the correctness of the modified space vector transformations while the numerical field-circuit model of the motor allowed for detailed analysis of the motor performance under assumed control strategy.

II. SYNTHESIS OF THE WINDING

A distributed six-phase winding of 36 slots forming a four-pole system was proposed. Due to the fractional number of slots per phase, a double layer winding was considered. The following figure shows the coils arrangement in one pole pitch.

Fig.1. Phase coils distribution on the pole pitch

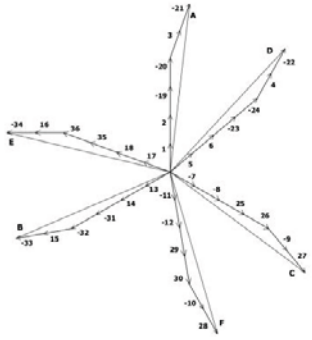

Fig.2. Phasor diagram

Arranging the coils according to proposed pattern allows one to determine the voltage star and the distribution of voltage vectors for each phase as in phasor diagram shown in Figure 2. With the above information, the winding diagram of the six-phase motor was determined [1].

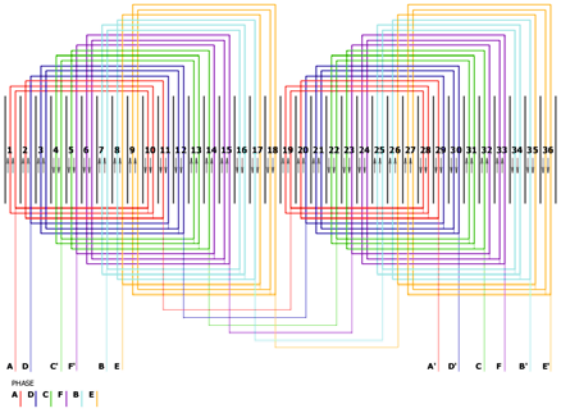

Fig.3. Diagram of the proposed six-phase winding

III. EXTENDED CLARKE AND PARK TRANSFORMATIONS

Working with three, or in this case six, currents complicates the control system considerably. However, a slight modification of the Clarke transform allows to obtain a classical representation of the system using space vector on the basis of which the motor control is performed. Figure 4 shows the phasor diagram of an asymmetrical six-phase system [2].

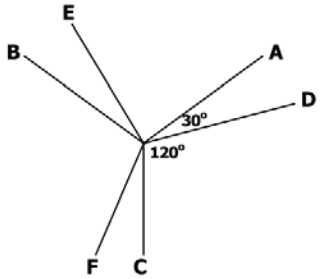

Fig.4. Phasor diagram of asymmetrical six-phase system

The phase shifts between vectors of above system determines the phase conversion matrix of the natural (*abc def*) system into orthogonal α and beta β rotating vectors. The inverse substitution has the similar form to equation (1).

To determine the *abc def* on the basis of α β the transform matrix is inverted.

$$\begin{bmatrix} a \\ b \\ c \\ d \\ e \\ f \end{bmatrix} = \begin{bmatrix} 1 & 0 \\ \cos\left(\frac{2\pi}{3}\right) & -\sin\left(\frac{2\pi}{3}\right) \\ \cos\left(\frac{4\pi}{3}\right) & -\sin\left(\frac{4\pi}{3}\right) \\ \cos\left(\frac{\pi}{6}\right) & -\sin\left(\frac{\pi}{6}\right) \\ \cos\left(\frac{5\pi}{6}\right) & -\sin\left(\frac{5\pi}{6}\right) \\ \cos\left(\frac{9\pi}{6}\right) & -\sin\left(\frac{9\pi}{6}\right) \end{bmatrix} \begin{bmatrix} \alpha \\ \beta \end{bmatrix} \quad (1)$$

The vectors thus determined can be transformed into rotating reference frame by standard Park transformation matrix [5]

$$\begin{bmatrix} d \\ q \end{bmatrix} = \begin{bmatrix} \cos(\theta) & \sin(\theta) \\ -\sin(\theta) & \cos(\theta) \end{bmatrix} \begin{bmatrix} \alpha \\ \beta \end{bmatrix} \quad (2)$$

$$\begin{bmatrix} \alpha \\ \beta \end{bmatrix} = \begin{bmatrix} \cos(\theta) & -\sin(\theta) \\ \sin(\theta) & \cos(\theta) \end{bmatrix} \begin{bmatrix} d \\ q \end{bmatrix} \quad (3)$$

where θ is rotor angular position

To validate the correctness of the extended transforms the circuit diagram model shown in Fig. 5 has been implemented Matlab Simulink environment. The above matrix calculations were included and *abc def,* α β, as well as *d q* waveforms were plotted.

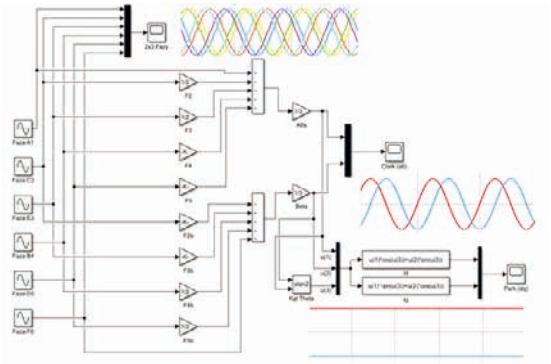

Fig.6. Clarke-Park transform scheme in Matlab Simulink environment

IV. FINITE ELEMENT ANALYSIS

Initially, to validate correctness of the proposed winding an induced voltage test was performed using a 4 pole rotor with permanent magnets.

After a positive result of test, i.e. obtaining six-phase system of induced voltage waveforms, a target reluctance rotor was implemented in the model (see geometry and mesh shown in Fig. 6) and the corresponding current excitations have been determined according to extended Clarke and Park transforms. Implementing the transforms into the model allow for arbitrary control of the *Id Iq* values [3].

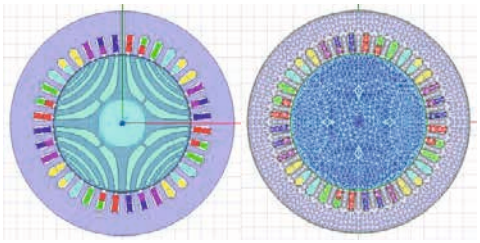

Fig.6. Model of the designed six phase SynRM

Development of the field model of studied machine allowed for an in-depth analysis of the operating states and the investigation of impact of control strategy on SynRM drive performance. An example of the torque by the motor and the magnetic flux distribution during operation are shown in Figs 7 and 8, respectively [4].

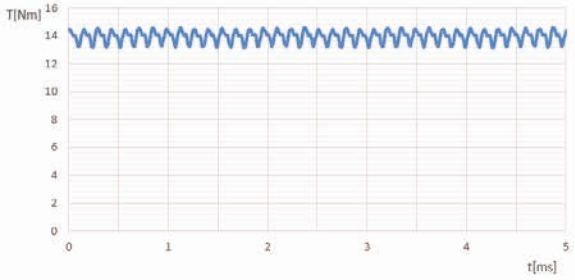

Fig.7. Example of the torque created by motor

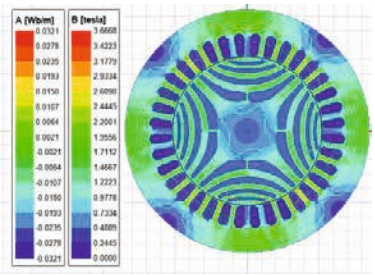

Fig.8. Magnetic flux distribution

IV. CONCLUSIONS

The paper deals with design and analysis of six-phase synchronous reluctance motor. The six phase winding layout has been determined based on phasor diagram, performed finite element analysis proves proper design of the motor. The detailed results will be discussed during the conference and included the scope of the full version of the paper.

REFERENCES

[1] L. Bojtor, I. Schmitd, "Simulation of controlled converter-fed synchronous motor", *Proc. of 4-th European Conference on Power Electronics and Applications*, Firenze, Vol.4, pp. 609-614, 1991.
[2] A. Bossavit, "How weak is the 'weak solution' in finite element methods", *IEEE Trans.Magn.,* Vol. 33, No. 5, pp. 2429-2432, 1998.
[3] C. Liaw, M. Lu, P. Jhou, and K. Chou, "Driving Control Technologies of New High-Efficient Motors", in Applied Electromechanical Devices and Machines for Electric Mobility Solutions. London, United Kingdom, doi: 10.5772/intechopen.88348
[4] C. Jędryczka, W. Szeląg, Z. J. Piech, "Multiphase permanent magnet synchronous motors with fractional slot windings: The future of low speed drives?", COMPEL, 2016, Vol. 35, No. 6, pp. 1937-1948

COMPARATIVE ANALYSIS OF THE MULTI-DRIVE POWERED SYNCHRONOUS RELUCTANCE MOTOR WITH THREE- AND SIX-PHASE WINDING UNDER DRIVE FAULT CONDITIONS

Michał Mysiński

Poznań University of Technology, Institute of Industrial Electrical Engineering
Piotrowo 3a, 61-138 Poznań, Poland, e-mail: michal.mysinski@student.put.poznan.pl

***Abstract* – The paper deals with analysis of the synchronous reluctance motor (SynRM) operation under fault conditions of multi-drive supply system composed of a two 3-phase drives. The two arrangements of 3-phase and one of 6-phase winding were investigated. The developed field models were used to calculate electromagnetic torque and radial magnetic forces occurring in the condition of the inverter failure. The selected research results have been presented and discussed.**

I. INTRODUCION

Due to low cost and high reliability the SynRM are becoming attractive alternative to the permanent magnet synchronous or squirrel cage asynchronous machines.

In order to increase the reliability and provide fault tolerance of the electric propulsion systems the multi-drive (i.e. composed of more than single 3-phase inverter or inverter of higher number of phases) supply systems are becoming in focus in the past [1, 3, 4].

II. CONTROL OF THE POWER SUPPLY

In order perform comparative analysis between studied 3-phase and 6-phase multi-drive systems the same power conditions must be ensured. Assuming similar value of the winding factor for studied windings the power equivalence can be achieved by ensuring the same magnetomotive force (*mmf*) in the slot. The phase current in the 6-phase winding was equal 120A. As it is a double-layer winding, the total *mmf* in the slot is 240A. The total *mmf* was used to calculate phase current of a 3-phase single-layer winding. The next step is to determine the maximum torque per ampere operation point. This was achieved through vector control and the use of Clarke-Park transforms. The optimal in terms of torque constant of the machine quadrature and direct axes currents I_q I_d [2, 3, 6].

$$I_{am} = \sqrt{I_d^2 + I_q^2} \tag{1}$$

where I_{am} is current amplitude

$$\begin{bmatrix}\alpha\\ \beta\end{bmatrix} = \begin{bmatrix}\cos(\theta) & -\sin(\theta)\\ \sin(\theta) & \cos(\theta)\end{bmatrix}\begin{bmatrix}d\\ q\end{bmatrix} \tag{2}$$

By determining the currents I_q I_d and then using Park's transform, the currents in orthogonal stationary frame α β are obtained. On this basis, the Clarke transform for a 3-phase winding is defined.

$$\begin{bmatrix}a\\ b\\ c\end{bmatrix} = \begin{bmatrix}1 & 0\\ \cos(\frac{2\pi}{3}) & -\sin(\frac{2\pi}{3})\\ \cos(\frac{4\pi}{3}) & -\sin(\frac{4\pi}{3})\end{bmatrix}\begin{bmatrix}\alpha\\ \beta\end{bmatrix} \tag{3}$$

The *a*,*b*,*c* currents for 3-phase machine have the same values of first D_1 and second drive D_2 by which machine is supplied. By modifying the Clarke transform, the matrix for the 6-phase winding can be similarly determined.

$$\begin{bmatrix}a\\ b\\ c\\ d\\ e\\ f\end{bmatrix} = \begin{bmatrix}1 & 0\\ \cos(\frac{2\pi}{3}) & -\sin(\frac{2\pi}{3})\\ \cos(\frac{4\pi}{3}) & -\sin(\frac{4\pi}{3})\\ \cos(\frac{\pi}{6}) & -\sin(\frac{\pi}{6})\\ \cos(\frac{5\pi}{6}) & -\sin(\frac{5\pi}{6})\\ \cos(\frac{9\pi}{6}) & -\sin(\frac{9\pi}{6})\end{bmatrix}\begin{bmatrix}\alpha\\ \beta\end{bmatrix} \tag{4}$$

This matrix is constructed for a 6-phase drive system. The 6-phase supply system can be composed of two 3-phase drives D_1 and D_2 ensuring that the phases of D_2 are shifted in phase by 30° in reference to D_1 [1].

III. STUDIED MACHINES

The studied two configurations of multi-drive 3-phase supply system are shown in Fig. 1

a) b)

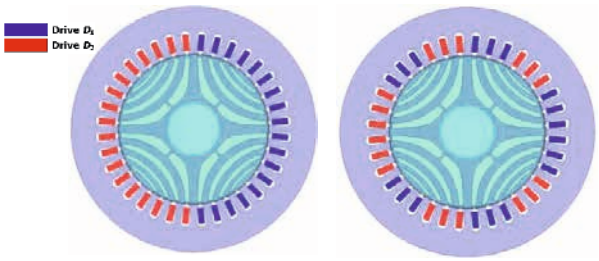

Fig. 1. Configurations of 3-phase multi-drive supply system

The 6-phase winding is double-layer. In this case, the distribution of the winding in one pole is as follows (AA|AD|DD|CC|CF|FF|BB|BE|EE). Fig. 2 presents the layout of a 6-phase multi-drive system [4, 5].

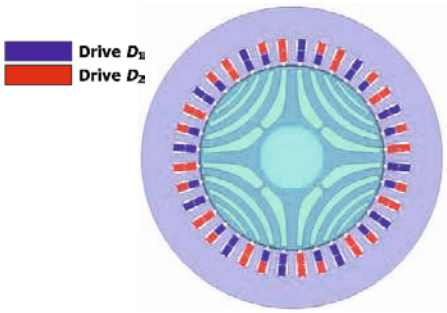

Fig. 2. The 6-phase multi-drive system

IV. RESULTS

The simulations of operation of the studied machines with different windings under normal and the drive fault conditions have been performed. The torque waveforms have been compared first. To compare torque value over different configurations the same *mmf* in slot has been ensured for all simulations. For clarity, multi-drive configuration from Fig. 1 a) will be called C_1, Fig. 1 b) C_2 and Fig. 2 C_3. The dotted lines shows the results for normal operation (i.e. drives D_1 and D_2 supply the machine according to (3) and (4)), while continuous lines represent torque waveforms assuming failure of one drive (currents in D_1 are zero).

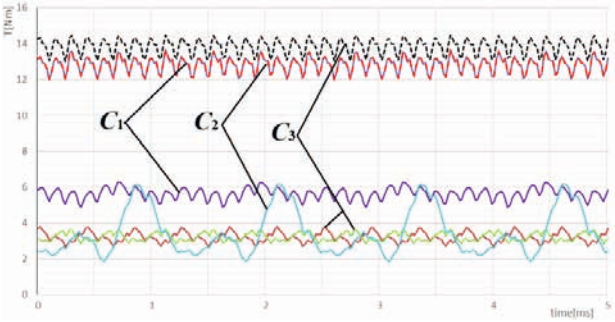

Fig. 3. Comparison of torque waveforms for operation under normal and fault conditions

It can be seen that, at normal operation, both configuration of 3-phase winding have the same torque waveforms. It should be noted that 6-phase machine provide 5-10% more torque than 3-phase machines. Analysing torque waveform for C_2 it can be stated that such configuration is not suitable for operation under drive fault because of very high torque ripples. Supplying machine according to case C_1 provide almost half of maximum torque. Different waveforms can be seen in C_3 depending on which drive fails (red and green waveforms). This is due to phase shift between D_1 and D_2. In case of C_3 a torque drop to 30% of nominal value can be observed.

Operation under drive fault create lack of the *mmf* in specific sections of the stator. This causes unbalance of magnetic radial forces and also global force acting on the rotor. This kind of forces are dangerous for the bearings life-time and significantly increase vibrations and noise of the machine.

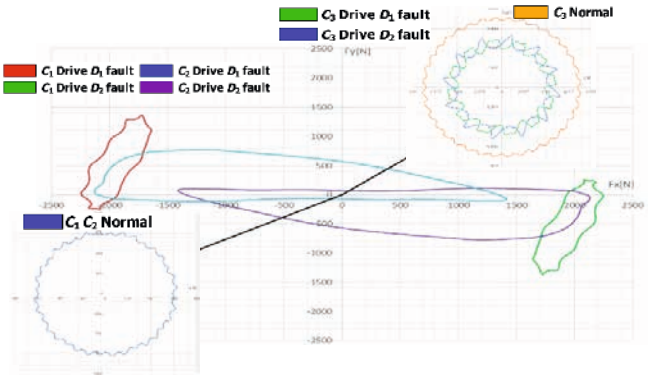

Fig. 4. Orbit diagrams of magnetic radial forces for C_1, C_2, C_3

The orbit diagrams presented above compare the action of magnetic radial forces occurring in particular configurations. The C_1 system in the state of failure of the driver, despite the maintenance of high torque, generates enormous radial forces exceeding 2kN in x-axis. It has been observed that the force is directed more towards the working inverter. The C_2 system generates high forces in both sides of the x-axis, creating ripple of the rotor. C_3 works best from the examples considered. Despite operating in the state of failure of the inverter, the favorable arrangement of the drivers causes the forces to be cancel as in the normal operation state and these forces assume negligible values.

V. CONCLUSIONS

The paper deals with comparative analysis of the multi-drive powered (SynRM) with 3-phase and 6-phase winding under drive fault conditions. Three configurations of the motor multi-drive supply systems were proposed and analysed. The waveforms of torque and radial forces under normal and single drive failure conditions were calculated. Conducted studies showed that only the 6-phase system can work properly in the drive fault condition, without generating unbalance of the radial forces. The detailed results will be discussed during the conference.

REFERENCES

[1] C. Jędryczka, W. Szeląg, "Analysis of the multi-drive powered permanent magnet synchronous motor under drive fault conditions", SME 2017 – Nałęczów, Poland : IEEE, 2017.

[2] Ren Yuan, Zhu Z. Q.: Reduction of Both Harmonic Current and Torque Ripple for Dual Three-Phase Permanent-Magnet Synchronous Machine Using Modified Switching-Table-Based Direct Torque Control. IEEE Transaction on Industrial Electronics, Vol. 62, No. 11, pp. 6671–6683, November, 2015

[3] Kontarcek A., Bajec P., Nemec M.: Cost-Effective Three-Phase PMSM Drive Tolerant to Open-Phase Fault. IEEE Transaction on Industrial Electronics, vol. 62, No 11, pp. 6708– 6718, November, 2015.

[4] Rolak M., Che H.S., Malinowski M.: Modeling and Fault-tolerant control of 5-phase induction machine. Bulletin of Polish Academy of Sciences, Technical Sciences, Vol. 63, No. 4, pp. 997–1006, 2015.

[5] Scuiller F., Charpentier J., Semail E., "Multi-star multi-phase winding for a high power naval propulsion machine with low ripple torques and high fault tolerant ability", Vehicle Power and Propulsion Conference (VPPC), IEEE, 2010.

[6] Heidari H., Rassolkin A., Kallaste A., Vaimann T., Andriushchenko E., Belahcen A., Lukichev D., "A Review of Synchronous Reluctance Motor-Drive Advancements", Mechatronics Technology and Transportation Sustainability, January, 2021

DESIGN ADVANTAGES AND ANALYSIS OF A NOVEL FIVE-PHASE DOUBLY-FED INDUCTION GENERATOR

Ryndzionek R., Michna M., Kutt F., Kostro G., Blecharz K.

Gdańsk University of Technology, Faculty of Electrical and Control Engineering
11/12 Gabriela Narutowicza Street, Gdansk, Poland, e-mail: roland.ryndzionek@pg.edu.pl

***Abstract* - This paper presents the research into the performance analysis of a novel five-phase doubly-fed induction generator (DFIG). The proposed solution aims at extending the range of possible modes of operation of an induction machine generation system. Modern doubly-fed induction generators are a dominating choice for wind energy conversion systems (WECSs). Because electrical failures are the most common failures in WECSs, the five-phase DFIG decreases the possibility of the system downtime due to increase fault-tolerant operation capability**

I. GENERAL INFORMATION

The doubly-fed induction generators (DFIG) have well-known advantages of simple constructions and low maintenance and are industrially applicable. They are mainly used in modern wind power plants instead of permanent magnet synchronous generators [1], [2].

Nowadays, when the industry market increases rapidly, semiconductors and converters are getting cheaper, and different and innovative solutions are being explored. Multi-phase machines have several advantages over three-phase systems, such as fault tolerance, higher torque density, and lower torque pulsation [3].

This paper presents a behavioral level model of a novel 5-phase DFIG based on the winding function approach (WFA). The main advantage of this approach is that the model description is based on actual machine winding distribution and the airgap geometry [4], [5]. However, this fault only applies to large airgap machines and is insignificant in induction machines [6], [7], [8].

The paper is organized as follows: the structure of the developed five-phase DFIG is introduced (Fig. 1), and its principle of operation and mathematical model is described in section II. The FEM simulation of the prototype is presented in section III. Section IV explains the manufacturing of the prototypes and experimental analysis. Finally, the paper ends with a summary of the obtained results.

II. MATHEMATICAL MODEL OF FIVE-PHASE DFIG

The specifications of the prototype DFIGs used in this study are shown in Table I. This generator has a six-pole, three-phase stator winding with one parallel branch and was constructed in a frame size of 132 mm. The generator has been developed using the original stator from a 5.5 kW Sg132m-6 induction motor. The five-phase rotor winding and core have been designed from scratch to fit and perform with the original core and winding of the selected induction motor.

The rotor was manufactured with a set of five slip-rings. The machine design was based on a predetermined minimum and maximum speed, the set output electric power, and the maximum rotor voltage (Ur < Us) corresponding with the operating speed range.

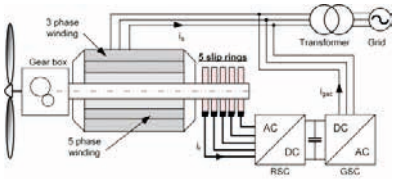

Fig.1. The scheme of the developed novel five-phase DFIG.

TABLE I
5-PHASE DFIG PARAMETERS

Parameter	Value	
Rated Power	Pn	4 kW
Voltage	Un	400V
Pair poles	p	3
Stator phases	ms	3
Rotor phases	mr	5
Stator slots	Qs	36
Rotor slots	Qr	30

A BASIC MODEL OF THE 5-PHASE DFIG

The stator and rotor voltage equation describe the general form of the voltage equation of the 5-phase DFIG model:

$$U_s = R_s I_s + \frac{d}{dt}\Psi_s \quad (1)$$

$$U_r = R_r I_r + \frac{d}{dt}\Psi_r \quad (2)$$

where: U_s, U_r – stator and rotor voltage vectors, I_s, I_r – stator and rotor current vector, R_s, R_r – stator and rotor resistance matrix, Ψ_S, Ψ_r – stator and rotor flux linkage.

The developed DFIG analytical model was used to simulate the generator's no-load and load state. The generator is driven at a constant speed and the rotor windings are supplied with alternating currents shifted in phase by 2/5π. The generator load level is controlled by changing the value of the resistance connected to the stator terminals. The amplitude and frequency of the rotor currents and rotor speed are adjusted to the measurement conditions. In the no-load state (Fig. 3a), the flux in the machine is excited by the flow of rotor currents. The no-load voltage amplitude (Us0m) induced in stator winding is defined by:

$$U_{s0m} = \frac{5}{2} L_{sr} I_{rm} (\omega_r + p\omega_{rm}) \quad (3)$$

where: *Lsr* - amplitude of the mutual inductance between stator and rotor windings, *Irm* - amplitude of rotor current, *fr* - frequency of rotor current, *ωrm* - Angular velocity of the rotor. Moreover, the load simulation has been developed. The result of the simulation has been presented in Fig. 3b. Finally, the analytical calculation from the model has been compared with the measurement results

(Fig. 4). The model shows very high convergence, and the other measurement results will be presented in Chapter IV.

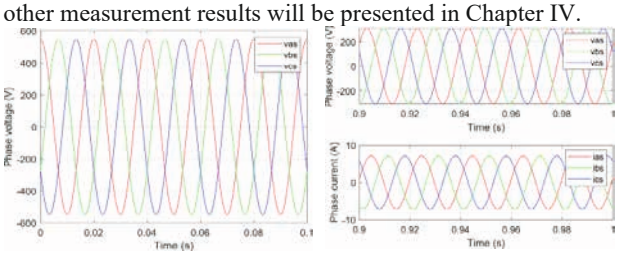

Fig. 3. a)The no-load voltage waveforms - simulation results. b) The voltage and current waveforms under resistive load - simulation results.

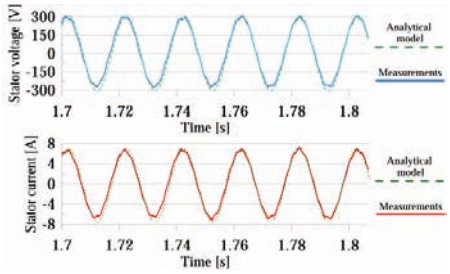

Fig. 4. The experimental and analytical calculation results under the resistive load

III. THE FEA ANALYSIS OF FIVE-PHASE DFIG

The 5-phase DFIG has been designed using the 3D CAD software also. The simulations were conducted to verify the analytical design calculated dimensions and parameters. The Ansys Maxwell and RMxpert Design have been used. Moreover, FEA validated the designed prototype's capability to perform in different operating conditions.

Fig. 5a shows the 2D and 3D FEM simulations of DFIG's flux density distribution. The maximum value of flux density is 1.4 T, and the results of both simulations are similar. However, the 3D simulations better represent the phenomenon of slots harmonics. The maximum value of flux density in the air gap is 0.75 T (Fig. 5b). The results fit in desired ranges. Moreover, the flux distribution corresponds to the stator and rotor slots distribution.

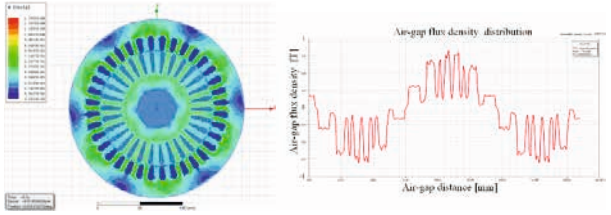

Fig. 5. a) The FEA 2D and 3D simulation of the stator and rotor core flux density distribution. b) The air gap magnetic flux distribution using FEA software.

IV. LABORATORY TESTS

The measurement was performed at a constant speed of 810 rpm without any load. The DFIG stator is star-connected, and the measurements have been made for different rotor currents. Those measurements have been compared with simulation results. Fig. 6 shows experimental test results. The rotor current exciting the machine is raised several times over the measurement period. These results have been compared with the FEA simulations (with the third and fourth/final steps in the rotor current rising sequence).

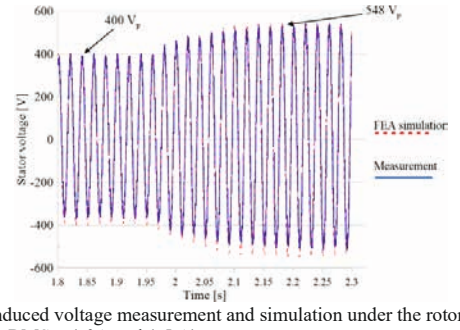

Fig. 6. Induced voltage measurement and simulation under the rotor current exciter (Ir RMS = 1.0A and 1.5 A).

The measurements and FEA simulation results are shown in Fig. 12a. The waveforms show good convergence between simulations and measurements, around 10-15V. The second measurements have been performed with different load conditions (resistive and inductive). In Fig. 12b, the mixed load has been performed. The active and reactive power was approx. 2 kW and 0.5 kVar.

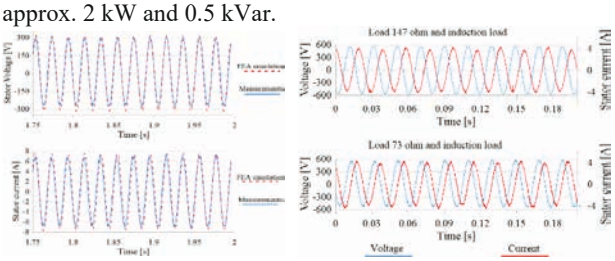

Fig. 12. The experimental and FEA simulation results under the resistive and mix load.

V. CONCLUSIONS

This paper proposes a novel five-phase DFIG dedicated to modern wind power plants. The proposed generator has been developed, and a prototype machine has been manufactured and tested under different operating conditions. Assumptions and calculations have been verified using FEM analysis and measurements performed on the prototype. The DFIG with five phase rotor can operate as a regular three-phase machine in an electric power generation system. Further investigation into the machine performance will focus on coping with output power quality during single or even dual rotor phase failures due to the inverter or the slip ring assembly fault. However, even with the standard motor stator, the machine could supply the load with both the active and reactive power.

REFERENCES

[1] P. Kumar and R. Choudhary, "Study of Doubly Fed Induction Generator Characteristics," *International Journal of Recent Research Aspects*, vol. 2, pp. 1–6, 2015.
[2] K. Protsenko and D. Xu, "Modeling and Control of Brushless Doubly-Fed Induction Generators in Wind Energy Applications," in *APEC 07 - Twenty-Second Annual IEEE Applied Power Electronics Conference and Exposition*. IEEE, 2 2007.
[3] M. Morawiec, P. Strankowski, A. Lewicki, J. Guzinski, and F. Wilczynski, "Feedback Control of Multiphase Induction Machines with Backstepping Technique," *IEEE Transactions on Industrial Electronics*, vol. 67, no. 6, pp. 4305–4314, 6 2020.
[4] M. Sartaj, M. R. Khan, and M. F. Khan, "Modelling of FivePhase Induction Generator Incorporating Magnetic Cross Saturation Effect," *Proceedings - 2019 International Conference on Electrical, Electronics and Computer Engineering*, UPCON 2019, 11 2019.
[5] Song Y., Wang X., Blaabjerg F., Doubly Fed Induction Generator System Resonance Active Damping Through Stator Virtual Impedance, IEEE Trans. Ind. Electron., vol. 64, no. 1, pp. 125–137 (2017), doi: 10.1109/TIE.2016.2599141.
[6] Maciejewski P., Iwański G., Six-phase doubly fed induction machine-based standalone DC voltage generator, Bull. Pol. Acad. Sci. Tech. Sci., vol. Vol. 69, no. nr 1, p. 135839 (2021), doi: 10.24425/BPASTS.2021.135839.
[7] Morawiec M., Blecharz K., Lewicki A., Sensorless Rotor Position Estimation of Doubly Fed Induction Generator Based on Backstepping Technique, IEEE Trans. Ind. Electron., vol. 67, no. 7, pp. 5889–5899 (2020), doi: 10.1109/TIE.2019.2955403.
[8] Paul Krause, Oleg Wasynczuk, Scott Sudhoff, and Steven Pekarek, Analysis of Electric Machinery and Drive Systems. John Wiley & Sons, Inc., 6 2013. [Online]. Available: https://onlinelibrary.wiley.com/doi/book/10.1002/9781118524336

INVESTIGATION OF IRREVERSIBLE AXIAL-STRAIN EFFECTS OF REBCO SUPERCONDUCTOR TAPES FOR ELECTRICAL MACHINES

Johannes Liebrich *, Christian Kreischer†

Helmut Schmidt University, Chair of Electrical Machines and Drive Systems,
Holstenhofweg 85 22043 Hamburg, Germany
Email: *j.liebrich@hsu-hh.de, †christian.kreischer@hsu-hh.de

***Abstract*—This paper investigates the critical temperature of a high temperature superconductor changes due to mechanical stress and whether the change is a reversible or irreversible effect. In order to achieve this, a static force is applied to the conductor and the exact critical temperature is measured using a multiphysical test bench. Subsequently, a new measurement is made at reduced force to investigate whether this displacement is reversible or not. For the design of applications it is of great importance to know the limit for the transition to the superconducting state.**

***Index Terms*—critical temperature, REBCO, axial tensile stress, HTS, reversible, irreversible**

I. Introduction

REBa$_2Cu_2O_{7-\delta}$ (REBCO, where RE=RARE EARTH) based second generation (2G) high temperature superconducting (HTS) wires are now used by a number of products. As an example for devices including magnets, superconducting fault current limiters (SFCL), superconducting magnetic energy storages (SMES), cables, etc. The mechanical and electromagnetical properties are one of the most important attributes of a 2G tape. Among these properties, the behavior of HTS tape under axial tension has attracted more investigations.

Previous investigations have shown that the magnitude of the critical current depends on the tensile strain. There is a reversible limit up to which the current does not decrease. If the reversible strain is exceeded, cracks occur in the superconducting REBa$_2$Cu$_2O_{7-\delta}$-layer and the critical current is irreversibly decreased [1], [2], [3].In this case the superconductor is damaged completely.

In this study, it is investigated in more detail how the critical temperature (T_c) of superconductors behaves after an axial stress is applied and afterwards is reduced. Is the conductor permanently damaged or do the original electrical properties return after a reduction. For this investigation, a sample is first cooled below the critical temperature under axial tension. The same measurement is then repeated with a reduced force to determine whether the electrical and mechanical properties have changed irreversibly. The purpose of this investigation is to systematically characterize a conductor material. Thus, the limits of superconductivity are characterized and models covering not only the electrical aspects but also the mechanical ones will be developed. This is especially important in the case of a failure, where high mechanical stresses can occur.

II. Experimental setup and procedure

The methodology according to which measurements are taken is presented below based on Figure 1. Two copper jaws (Pos. 1) are located between two thermally insulating holders (Pos. 2). These are thermally connected to a Sumitomo cold head (Pos. 3) and cooled. The superconductor sample (Pos. 4) to be tested is located between the upper and lower copper jaws. With three calibrated temperature sensors (Pos. 5) which operate down to 4.2 K with an accuracy of 10 mK, located at different points, a homogeneous temperature distribution can be ensured. At the upper and lower end of the superconductor there are two copper clamps each (Pos. 6). The two outer terminals are used to impress a small constant current of 1 A. The two inner clamps are connected to a Keysight 34470 multimeter with $7\,1/2$ digits. The multimeter thus measures the voltage drop between the two inner copper terminals. The whole setup is located inside a vacuum chamber to prevent convection. In order to be able to exert the necessary mechanical force on the conductor, the ends of the clamp jaw holders are coupled to a electrical actuated universal tensile testing machine. With the help of the machine, previously defined loads can be imprinted. In order to be able to carry out the necessary tests, the specimen is slowly cooled down at a constant current. The critical temperature can be recognized by a rapid drop in resistance. In the case of superconductors of the second type, the transition to the superconducting state is not abrupt, but is defined by a temperature window ΔT. During the cooling process, different forces are applied to the conductor, and the behavior to the critical temperature T_c is investigated. The results of the measurement can be found in the following section IV.

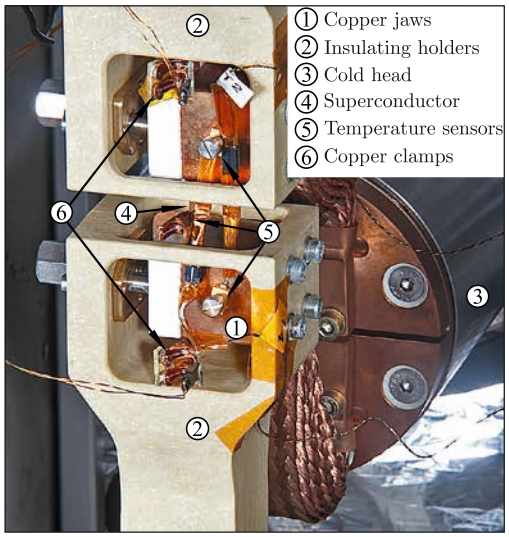

Fig. 1: Measurement setup

III. Samples

The architecture of the investigated REBCO tape is illustrated in Figure 2. This type has a substrate layer of Hastelloy C276 with a thickness of $50\,\mu$m. The subsequent layers consisting of a diffusion barrier (MgO $\sim$ $0,3\,\mu$m), ISD layer (MgO $\approx$ $3\,\mu$m), GdBaCuO coating film ($\approx$ $3\,\mu$m) and Silver cap layer ($\approx$ $2\,\mu$m). Type TPL 4120 is thermally, electrically and mechanically stabilized by a copper surrounding. This has a thickness of $\approx$ $20\,\mu$m, with the result that the tape reaches a total thickness of $\approx$ $100\,\mu$m [4].

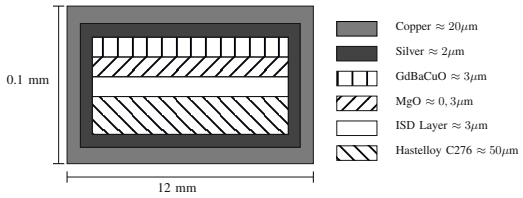

Fig. 2: Layered structure of the samples of type Theva TPL 4120 (not to scale) [5]

IV. Measurement results

Figure 3 shows the recorded temperature profile and the mechanical stress acting on the conductor in MPa. As can be seen from the figure, four measuring points with increasing stress were recorded first. Subsequently, the stress is reduced for the same sample. In the meantime, the critical temperature of the sample is measured in order to investigate this effect for reversibility. As depicted in Figure 4, the critical temperature decreases when the force is increased. Much more interesting is the fact that a subsequent reduction of the axial stress does not result in a shift of the critical temperature. Thus, it can be concluded that this effect is irreversible and the tape does not return to its original electrical properties even if the tape has not been completely damaged through the mechanical tension.

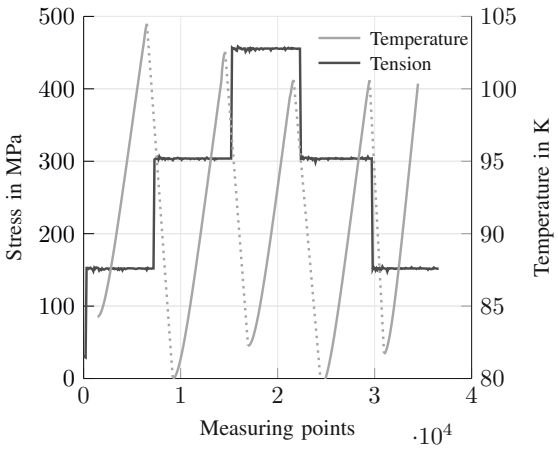

Fig. 3: Temperature and tension profile

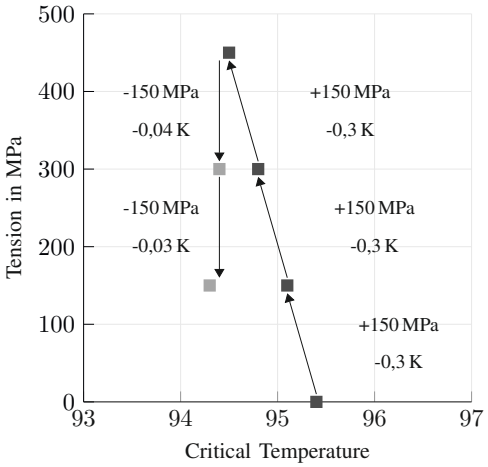

Fig. 4: Change of the critical temperature with the force curve applied from Fig. 3

V. Conclusion

The measurement results show that mechanical stresses on conductors have a negative influence on the critical temperature. Moreover, this effect can be declared as irreversible. In the full paper, the measurement methodology, the results with different measurements and an analytical approach to describe the effects are discussed in detail. In addition, a more detailed consideration is provided whether the mechanical stress causes a voltage drop along the conductor.

References

[1] D. C. van der Laan und J. W. Ekin, “Large intrinsic eff ect of axial strain on the critical current of high-temperature superconductors for electric power applications,” Applied Physics Letters 90.5 (2007), pp. 052506.
[2] S. Ochiai, H. Okuda, M. Sugano, K. Osamura and W. Prusseit, ”Influences of Electroplated Copper on Tensile Strain and Stress Tolerance of Critical Current in DyBCO-Coated Conductor”, IEEE Transactions on Applied Superconductivity, vol. 22, no. 1, pp. 8400607-8400607, Feb. 2012, Art no. 8400607.
[3] N. Cheggour, J. W. Ekin, and C. C. Clickner, “Reversible axial-strain effect and extended strain limits in Y-Ba-Cu-O coatings on deformation-textured substrates, Applied Physics Letters 83, 4223 (2003).
[4] W. Prusseit, R. Nemetschek, C. Hoffmann, G. Sigl, A. Lümkemann, H. Kinder, ”ISD process development for coated conductors”, Superconductivity and its Applications, Volumes 426–431 (2005),pp 866-871.
[5] Theva Website, THEVA Pro-Line General Properties.

IMPROVED METHODS FOR STATOR END WINDING LEAKAGE INDUCTANCE CALCULATION

Kostro Grzegorz, Michna Michał, Kutt Filip, Ryndzionek Roland

Gdańsk University of Technology, Faculty of Electrical and Control Engineering
11/12 Gabriela Narutowicza Street, Gdansk, Poland, e-mail: grzegorz.kostro@pg.edu.pl

***Abstract* - This paper proposes improved methods for calculating the value of the stator end winding leakage inductance of an induction machine. The forms were based on the stored magnetic energy, calculated by 3-D finite element analysis. In these methods, the rotor has been considered in the simulated machine's model. The analysis results show that the stator end winding leakage inductance value is a significant part of the value of the total leakage inductance. Therefore, considering end winding leakage inductance in a dynamic induction machine model improves the model accuracy.**

I. INTRODUCTION

The magnetic flux produced by the currents flowing through the windings of the electric machine can be divided into two components. The first magnetic flux component produced by the currents flowing through the end windings is usually termed end winding leakage flux. The main flux is the second component produced by the currents flowing through conductors placed in the machine's active part. Although the end winding leakage flux is small in comparison with the main flux, it may cause some harmful phenomena such as magnetic forces on the end winding [1],[2],[3],[4], and the eddy currents in the conductive parts on the end region [5], [6] and in the core end [7]. Besides, the accurately determined value of the leakage inductance is essential when calculating the induction motor's starting torque and current.

The geometry of the end part is more complex than the geometry of the active part. In the active part, the magnetic flux density vector may be represented by a 2-D vector rotated in the plane of magnetic core laminations [8]. However, the magnetic flux density distribution in the machine's end part is always 3-D. Therefore the analysis of this part is more complex and more time-consuming.

II. SURVEY OF RELATED WORKS

Mainly there are two approaches to calculating the value of end winding leakage inductance. One approach is based on the magnetic energy stored in the end region [9], [10], [11], [12], and the other is based on the flux leakage linking with the end winding [13], [14], [15]. Numerical methods, such as the finite element method (FEM) and two analytical methods, e.g., equivalent magnetic circuits [14], and Neumann integral [16],[17], have been used to calculate the above quantities.

An analytical calculation presented in [15] is based on solving the flux linkage. The geometry of the end winding was modeled as a semicircle, the method gave the rough value of the end winding inductance, but it was fast

Another analytical approach [16], using the method of images, took into account the influence of the iron core. The end winding was modeled by 3-D diamond winding to solve the problem.

In [11], [12], the end winding inductance was calculated using 2-D and 3-D models. The 2-D model calculated the end ring inductance under different boundary conditions. The leakage inductance calculations with different degrees of coupling between rotor and stator were based on the energy calculated utilizing the 3-D model.

The 3-D finite element analysis (FEA) gives accurate results. However, it is very time-consuming and requires many computation steps. The analyzed model has to be reduced to make it less time-consuming. It is necessary to assume that the machine is axis-symmetric. In addition, a quasi-3-D FEA requires the assumption that the field variables are sinusoidally distributed along the circumferential direction.

This paper proposes improved methods for calculating the stator end winding leakage inductance.

III. RESEARCH METHODS

Calculate the stator end winding leakage inductance considering that the rotor is rugged due to the irregular shape of end winding, end winding leakage, which may distribute at the end of the active part, and the fringing flux of the air gap. The fringing flux belongs to the main flux but goes into the end winding region. Then, not all the magnetic flux occurring in the end region is the end winding leakage flux. Therefore, it is essential to find a method to separate the leakage from the total flux accurately.

In this paper, two methods based on energy calculation are presented. Both methods require the assumption that the machine is symmetrical.

The first method, which will be called method A is based on the dependence between the total leakage inductance and the length of the machine's active region, and it can be written as follows:

$$L_{\sigma} = L_{active} + L_{\sigma end}. \tag{1}$$

L_{active} is proportional to the axial length of the active motor part (l_{Fe}), and $L_{\sigma end}$ remained constant, is independent of l_{Fe}.

The leakage inductance is calculated for a few lengths of the active region. The leakage inductance is divided into two parts using extrapolation of the leakage inductance value into the iron length equal to zero. The method is similar to the method presented in the literature [13]. The currents applying to the model produce fluxes in opposite directions in neighboring winding; the energy stored in the volume of the model is proportional to the total inductance. Then, the inductance can be calculated from the formula:

$$L_{tot} = \frac{4 \cdot E_{tot}}{3 \cdot I_{ph}^2}. \tag{2}$$

Where: L_{tot} total inductance, E_{tot} energy stored in the volume of the model, I_{ph} current flowing through the windings.

The second method will be called method B based on the energy stored in the end region of the machine. In this case, removing the energy produced by the fringing flux of the air gap is necessary. The model should have a volume closing fringing flux to remove the part of energy belonging to the end of the air gap. The authors assumed that the volume has a ring shape. The dimensions of the ring can be obtained from formulas:

$$D_{in} = D_r - h_r. \tag{3}$$

$$D_{out} = D_s + h_s. \tag{4}$$

$$h = (D_s - D_r) \cdot k_c. \tag{5}$$

Where: D_{in} inner diameter of the ring, D_r diameter of the rotor, h_r high of rotor slot opening, D_{out} outer diameter of the ring, D_s stator inner diameter, h_s high of stator slot opening, h high of the ring, k_c Carter coefficient. The dimensions of the ring were determined on the base of magnetic flux density analysis in the volume where the fringing flux is present. The view of the motor model with the ring mentioned above is shown in Fig. 1.

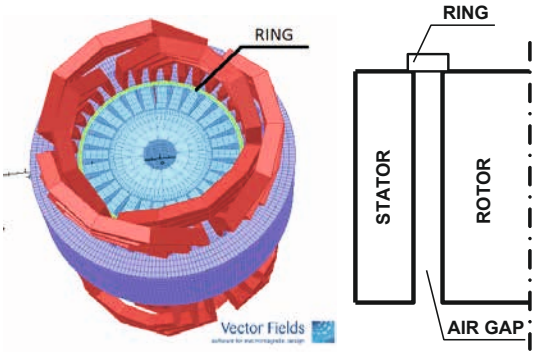

Fig.1. View of the 3D motor model with ring used in method B and sketch of its cross-section

Method B is less time-consuming than method A because the value of end winding inductance is calculated directly from energy. Method B does not require additional calculations or different mathematic operations like method A. Both presented methods can be used to improve the accuracy of a dynamic model of an induction machine.

Energy calculation for both methods was made using VECTOR FIELDS software called OPERA 3D. It required 3D windings and magnetic core models.

III. FINITE ELEMENT MODEL OF THE MOTOR

Using the coil models from the standard library of OPERA to build the stator winding with a significant filling factor can cause dimensional conflicts in the end-winding part (coils in the end-winding part overlap each other). Therefore such models lead to changes in the flux density distribution in the end-winding region. The consequence of this is erroneous in specifying the value of end-winding inductance. Therefore, it is necessary to develop models of coils that allow the construction of a winding without dimensional conflicts.

It should be noted that constructing coil models of any shape is possible in Opera 3D. For this purpose, the standard conductors from OPERAs library (bricks described by 8 and 20 nodes elements) can be used. The computer program was developed to automate the process of building the AC machine's stator windings. The program uses the 8-node elements to construct stator winding. The geometric model of the considered coil is defined by two basic objects (Fig. 2): a longitudinal coil axis and a set of cross-sections corresponding to the number of points defining a longitudinal axis of the coil.

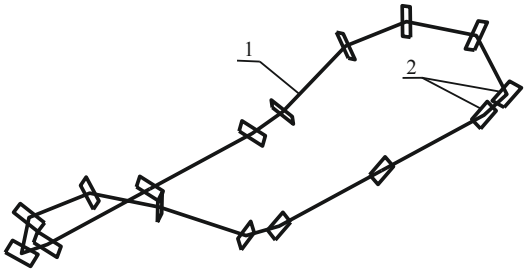

Fig. 2. Model 3D of a stator winding coil of an electric machine: 1 – longitudinal coil axis, 2 – set of transverse coil cross-section

Fig. 3 shows an example of a complete stator winding model built using the developed program.

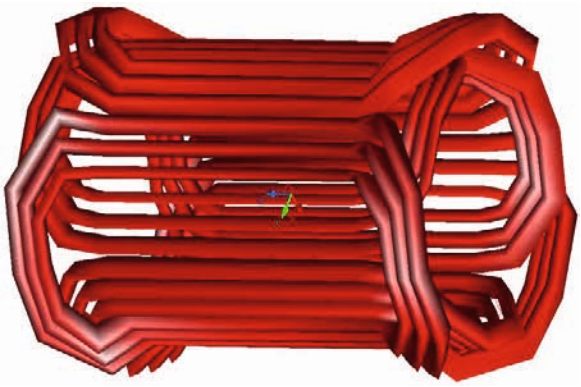

Fig. 3. Model 3D of single layer stator winding of an electric machine with concentrically wound coils

It should be noted that the construction of the model coil using the library 8-node elements requires the assumption of appropriate current density in the individual segments of the coil. The total current of the modeled coil in 3D Opera is a product of the assumed value of the current density and the area of the bottom base of the 8-node element (rectangle defined as the first). The direction of current flow determines the vector acting at the geometric center of the bottom base and directed to the geometric center of the upper base of the 8-node element.

The current density has the same value in each segment of the coil will cause the values of total currents in each of these elements to be different since the total current for the elements having the same cross-sectional area and the same density may take different values depending on the value of the bottom base area. It results in errors in induction distribution calculation.

The OPERA 3D has two modules for constructing a geometric model of the analyzed object: the modeler module and the Pre-Processor module. Due to the greater possibility of changing the mesh density in the analyzed object author has used the Pre-Processor module. However, it should be noted that the construction of a discrete model of the motor using this module is very time-consuming and requires much work. In order to shorten the construction time of a discrete model of the machine author developed a unique computer program. This program can build a model based on basic geometric dimensions (slot dimensions, stator outer diameter, the inner diameter of the stator, rotor diameter, the length of the active part, etc.) and the number of slots. A discrete model of the 3D motor used to calculate its windings inductance is shown in Fig. 4.

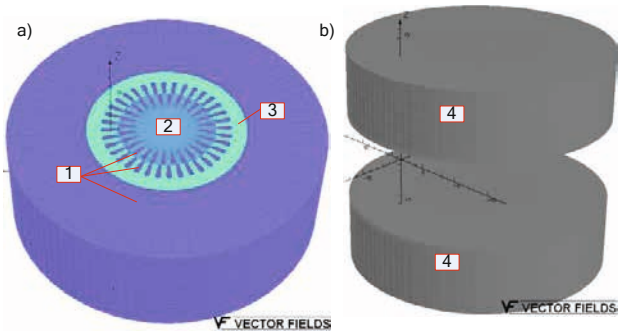

Fig. 4. Geometrical model of the considered motor made utilizing OPERA Pre-Processor: a) 3D model of the machine active part, air (1), rotor (2), stator (3), b) model of the end-winding background, air (4)

IV. STATOR END-WINDING LEAKAGE INDUCTANCE

The value of the end-leakage inductance was calculated for a 2.2 kW squirrel cage asynchronous motor. The main specification of the simulated machine is listed in Table I.

Calculations were carried out using the TOSCA module. In the calculations was assumed linear magnetic circuit of the motor and the currents value were as follows: the current in the first phase was equal to I_{ph}, and in the other two phases was equal to $-0.5I_{ph}$.

TABLE I
MAIN SPECIFICATION OF SIMULATED MACHINE

Name	Value
Rated power (kW)	2.2
Rated frequency (Hz)	50
Total length of stator iron core (mm)	100
Outer diameter of stator iron core (mm)	97
Inner diameter of stator iron core (mm)	47
Thickness of air gap (mm)	0.15
Number of pole pairs	2
Number of stator slots	36
Number of rotor slots	28
Number of parallel branches	1
Number of turns in series in a stator coil	39
Coil span of a stator coil (stator slot pitches	7, 9, 11

The total energy calculated using method A for different lengths of active machine parts is listed in Table II.

TABLE II
THE ENERGY OF SIMULATED MACHINE – METHOD A

Active part length (mm)	Stored Energy (J) [a]
100	0.37693
90	0.33961
80	0.30229
70	0.26497
60	0.22765

The dependence of the total inductance on its active part length is shown in

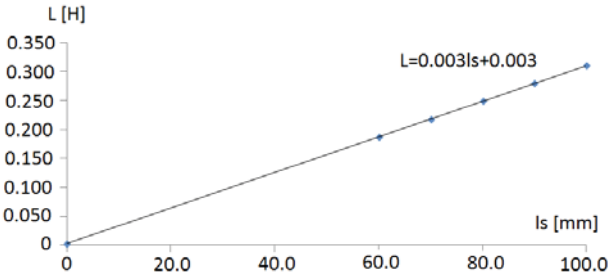

Fig. 1.

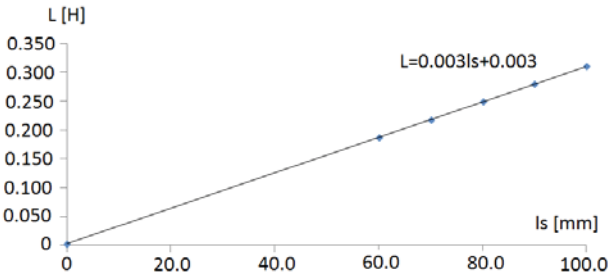

Fig. 1. The dependence of the total inductance from its active part length l_s

The value of the end-winding leakage inductance was calculated using the least mean square method on the base of

energy values presented in Table II. Method A gives the value of the end-winding leakage inductance equal to 3.06mH.

The energy value stored in the simulated model's end region calculated using method B for l_{Fe} equal to 100mm is 4.32mJ, and the corresponding end-winding leakage inductance calculated using equation (2) is 3.5mH.

To verify values of end-winding inductance calculated by methods A and B author compared these values with the inductance value calculated based on the method with removed rotor [10], [11], [12]. The value of the end-winding leakage inductance for the model with a removed rotor is equal to 3.6mH.

Method A requires significant accuracy in energy calculation due to the big difference between energy stored in the active part and the end-winding part of the machine.

V. CONCLUSIONS

This paper proposes improved methods for calculating the end-winding leakage inductance of a rotating electric motor. The stator end-winding leakage inductance of the 2.2-kW induction motor was computed based on the proposed methods. The method presented in the paper does not require rotor removal. The values of the end-winding leakage inductance computed based on the proposed method were compared with values computed using the method with the removed rotor. The computations show that method B is closest to the results obtained from the method presented in the literature.

The difference between end-winding leakage inductance calculated using methods A and B is less than 20%.

Results obtained in method A show that rotor influence on the value of end-winding leakage inductance exists. The difference between end-winding leakage inductance calculated using method A and the method that requires rotor removal is 17%.

The model of the stator end-winding described in the paper is general. Therefore the proposed methods are suitable for calculating the end-winding leakage inductance of other radial flux electric machines.

REFERENCES

[1] K.-C. Kim, H.-W. Lee, Y.-D. Chun, and J. Lee, "Analysis of electromagnetic force distribution on end winding for motor reliance," *IEEE Trans. Magn.*, vol. 41, no. 10, pp. 4072–4074, October 2005.

[2] Y. Fang, Q. Lv, X. Cheng, and X. Bao, "Analysis of stress distribution on end winding of large water filling submersible motor during steady-state operation," in *2013 5th International Conference on Power Electronics Systems and Applications (PESA)*, 2013, pp. 1–6.

[3] R. Lin and A. Arkkio, "3-D Finite Element Analysis of Magnetic Forces on Stator End-Windings of an Induction Machine," *IEEE Trans. Magn.*, vol. 44, no. 11, pp. 4045–4048, November 2008.

[4] R. D. Stancheva and I. Iatcheva, "3-D Electromagnetic Force Distribution in the End Region of Turbogenerator," *IEEE Trans. Magn.*, vol. 45, no. 3, pp. 1000–1003, Mar. 2009.

[5] Y. Yao, H. Xia, G. Ni, X. Liang, S. Yang, and P. Ni, "3-D eddy current analysis in the end region of a turbogenerator by using reduced magnetic vector potential," IEEE Trans. Magn., vol. 42, no. 4, pp. 1323–1326, Apr. 2006.

[6] R. Lin, A. Haavisto, and A. Arkkio, "Analysis of Eddy-Current Loss in End Shield and Frame of a Large Induction Machine," IEEE Trans. Magn., vol. 46, no. 3, pp. 942–948, Mar. 2010.

[7] K. Yamazaki, S. Tada, H. Mogi, Y. Mishima, C. Kaido, S. Kanao, K. Takahashi, K. Ide, K. Hattori, and A. Nakahara, "Eddy Current Analysis Considering Lamination for Stator Core Ends of Turbine Generators," IEEE Trans. Magn., vol. 44, no. 6, pp. 1502–1505, Jun. 2008.

[8] Y. Guo, J. G. Zhu, J. Zhong, H. Lu, and J. X. Jin, "Measurement and Modeling of Rotational Core Losses of Soft Magnetic Materials Used in Electrical Machines: A Review," IEEE Trans. Magn., vol. 44, no. 2, pp. 279–291, February 2008.

[9] A. Brahimi, A. Foggia, and G. Meunier, "End Winding Reactance Computation Results Using a 3D Finite Element Program," in Digest of the Fifth Biennial IEEE Conference on Electromagnetic Field Computation, 1992, 1992, pp. TP23–TP23.

[10] W. M. Arshad, H. Lendenmann, Y. Liu, J.-O. Lamell, and H. Persson, "Finding end winding inductances of MVA machines," in Industry Applications Conference, 2005. Fourtieth IAS Annual Meeting. Conference Record of the 2005, 2005, vol. 4, pp. 2309–2314.

[11] R. De Weerdt, E. Tuinman, K. Hameyer, and R. Belmans, "Finite element analysis of steady state behavior of squirrel cage induction motors compared with measurements," IEEE Trans. Magn., vol. 33, no. 2, pp. 2093–2096, Mar. 1997.

[12] R. De Weerdt and R. Belmans, "Squirrel cage induction motor end effects using 2D and 3D finite elements," in Electrical Machines and Drives, 1995. Seventh International Conference on (Conf. Publ. No. 412), 1995, pp. 62–66.

[13] R. Lin and A. Arkkio, "Calculation and Analysis of Stator End-Winding Leakage Inductance of an Induction Machine," IEEE Trans. Magn., vol. 45, no. 4, pp. 2009–2014, Apr. 2009.

[14] K. J. Meessen, P. Thelin, J. Soulard, and E. . Lomonova, "Inductance Calculations of Permanent-Magnet Synchronous Machines Including Flux Change and Self- and Cross-Saturations," IEEE Trans. Magn., vol. 44, no. 10, pp. 2324–2331, October 2008.

[15] M.-F. Hsieh, Y.-C. Hsu, D. G. Dorrell, and K.-H. Hu, "Investigation on End Winding Inductance in Motor Stator Windings," IEEE Trans. Magn., vol. 43, no. 6, pp. 2513–2515, Jun. 2007.

[16] D. Ban, D. Zarko, and I. Mandic, "Turbogenerator end winding leakage inductance calculation using a 3-D analytical approach based on the solution of Neumann integrals," in Electric Machines and Drives Conference, 2003. IEMDC'03. IEEE International, 2003, vol. 3, pp. 1576–1582 vol.3.

[17] A. Schramm and D. Gerling, "Analytical calculation of the end winding leakage inductance based on the solution of Neumann integrals," in Proceedings of the IEEE International Symposium on Industrial Electronics, 2005. ISIE 2005, 2005, vol. 2, pp. 851–855 vol. 2.

NON-LINEAR EFFECTS OF OPERATION TEMPERATURE ON A FIELD- COUPLED CURRENT-CONTROLLED INDUCTANCE

Guido Schierle, Michael Meissner, Klaus F. Hoffmann

Helmut Schmidt University, Germany

Corresponding author: Guido Schierle, guido.schierle@hsu-hh.de

Topic: Nonlinear Coupled Electromagnetic Phenomena
Preferred presentation form: Poster Presentation

Abstract

In this publication the effect of the operation temperature on the effective inductance of a controllable inductor is analysed. The main difference compared to a coil with a simple single core lies in the current-controlled inductance-value. This is achieved by a second core implemented perpendicular upon the load-toroid effecting the saturation within a limited shared volume. The dependencies on the core-temperatures are investigated by measurement.

1 Introduction

Inductivities are widely used for lots of different purposes. Energy storage for buck- or boost-converters, resonant tank elements for different types of resonant converters and inductors for filters should be mentioned as typical examples. Often, fix optimal values can be found and corresponding devices can be implemented. In some cases the availability of wide ranges of input- or output-parameter and a possibility to change on-the-fly would be desirable. This results almost always in a suboptimal compromise, because effects like saturation and losses must be taken into account. Especially in suction circuits for filters or resonant tank applications with changing parameter sets adaptable inductivities may be a promising alternative.

For this publication, a setup is used consisting of two intersecting toroid cores with a control- and a load-winding. This is depicted in Figure 1. In a previous publication the effect of the control winding on the measurable inductivity of the load winding is presented [1]. However, magnetic materials are known for a temperature dependence with the most significant effect of loosing all properties at the Curie-temperature. The connection between magnetic field strength and flux changes already before, resulting in a distortion of the original BH-curve. This is investigated in the presented paper with its effect on the usability of the mentioned setup for measurements in laboratory environments.

2 Operation principle

As described the setup consists of two intersecting toroid-cores with one winding each. The control winding is used to purposefully saturate the intersecting volume and therefore affect the inductivity of the load winding. An detailed explanation of the used measurement method can be found in [2].

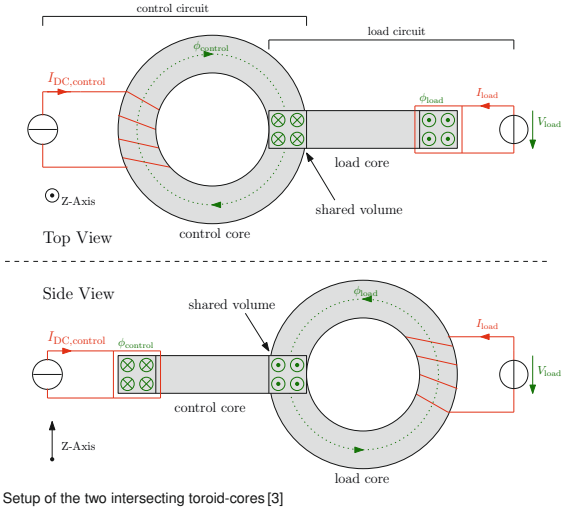

Fig. 1: Setup of the two intersecting toroid-cores [3]

3 Temperature dependency

In order to describe the temperature dependency the setup has been implemented within an climate chamber and measured at three different ambient temperatures, which are -20 °C, 25 °C and 100 °C, giving a maximal temperature interval of 120 °C. At each temperature a series of measurements is conducted giving a set of curves characterising the setup. The change of these curves indicates the temperature dependency. Control currents up to 30 A were applied, using the E-6 series assuming a non-linear behaviour of the investigated effective inductance and the BH-characteristics.

4 Measurement results and further research activities

For investigation a ferrit of the company TDK, made from the material N30, was used. One of the most important characteristic for this setup at 25 °C is a saturation flux density of 380 mT for 10 kHz [4]. For the presented measurements only dc-voltage and -current will be used, which must be considered in evaluation. Fig. 2 shows the effect of the control current on the effective inductance and the BH-characteristics at 25 °C. It can be seen that the effective inductance decreases with rising control current. Furthermore, the characteristic curve starts to flatten, which is expectable considering the shared volume of both cores as a variable air gap. A more detailed analysis of this behaviour is given in [2].

For the chosen 100 °C the stated saturation flux density drops to 240 mT for 10 kHz and the BH-characteristic flattens significantly, which is observable in [4]. The transition to a fully saturated

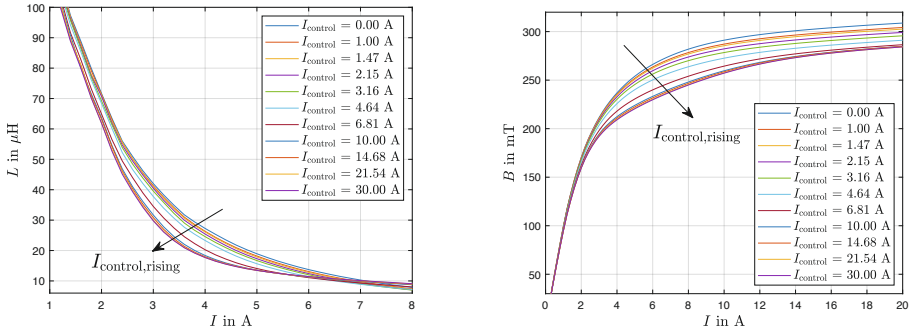

(a) Dependency of effective inductance on control current at 25 °C

(b) $B - H$ characteristics with applied control current at 25 °C

Fig. 2: Exemplary impact of control current on effective inductance and $B - H$ characteristics at 25 °C

core material seems to be reached faster and more sudden, which could open up the setup for a wider use in applications. Additionally, an analysis could present interesting results, because 100 °C is not an unusual operating temperature. On the contrary, there are no information given about the behaviour of the flux density for a temperature below 25 °C. Again, the examination of the chosen minimal value of -20 °C could display further insights on the characteristics of the presented setup. It will be interesting to see if there are any advantages which could prevail the need of cooling the system down. Both conditions will be investigated by measurement and presented in the full paper.

An analysis of possible effects of the rise of the temperature could allow assumptions about the characteristics of the setup right after switching it on and after a certain runtime.

References

[1] S. Brandt, M. Meissner, N. Polap, G. Schierle, and K. F. Hoffmann, “A survey on adjustable inductances for power electronic circuits,” in *PCIM Europe digital days 2022; International Exhibition and Conference for Power Electronics, Intelligent Motion, Renewable Energy and Energy Management*, 2022.

[2] G. Schierle, M. Meissner, and K. F. Hoffmann, “Analysis and discussion of a concept for an adjustable inductance based on an impact of an orthogonal magnetic field,” Unpublished Paper, Review Process Pending, expected in European Conference on Power Electronics and Applications, EPE 2022 ECCE Europe, 2022.

[3] D. Magel, “Implementation, analysis and comparison of different prototypes of current controlled inductors for power electronic applications,” in *Bachelor Thesis*, 2022.

[4] TDK, “Siferrit material n30,” in *Ferrites and accessories*, 2017.

CURRENT ANALYSIS OF LOW-LEVEL, ASYMMETRICAL INTER-TURN SHORT-CIRCUIT IN THE STATOR OF AN INDUCTION MOTOR

Konrad Górny, Mikołaj Marczak, Wojciech Pietrowski

Poznan University of Technology, Institute of Industrial Electrical Engineering
Piotrowo 3a, 61-138 Poznań, Poland, e-mail: {konrad.gorny, wojciech.pietrowski}@put.poznan.pl

Abstract – The paper presents current analysis of multi-phase, asymmetrical inter-turn short-circuits in a squirrel-cage induction motor. The test object was the motor: Celma Inducta 3SIE100L4B. Measurements of the phase current of the tested object were used in the diagnostic process. Due to the nature of the failure like inter-turn multi-phase short-circuits and their impact on the current waveforms, the frequency analysis of the diagnostic signal was used.

I. INTRODUCTION

Due to the development of new technologies, and hence the increasing popularity of electronic systems, low production costs and satisfactory operating properties, induction motors continue to lead the way in drive systems used in industry [1-3]. It should be noted that induction motors are successfully used in the dynamically developing in recent years electric car industry [4, 5]. The growing interest in induction motors and an increasing emphasis on ecology and environmental protection [6, 7] around the world consequently translates into the ever-growing demand for efficient and precise diagnostics of these machines [2].

The research carried out over the last few years has proved that one of the most common causes of failure of induction motors are the inter-turn short-circuits occurring in the stator circuit [2, 8, 9], caused by damage of the insulation of individual turns of the coil. An inter-turn short-circuit as a result of damage propagation can lead to a short circuit in more than one phase of the machine.

In the article, the second chapter presents the diagnostic data acquisition method, the third chapter contains the description and results of the signal analysis, while the fourth chapter presents the conclusions resulting from the analysis of current of low-level inter-turn short-circuits.

II. MEASUREMENT

Contrary to the research on the early stage of a inter-turn short-circuit of stator winding, the presented test results concern a coil short circuit with a small number of short turns. In the presented research, measurements were made for an undamaged winding and for the number of shorted turns from 1 to 5, i.e. low level damage.

In order to obtain diagnostic data, tests were carried out. The tests were carried out on a real object and the measuring station consisted of: 3SIE100L4B motor rewind in such a way as to make it possible to perform low-level, inter-turn short-circuits under controlled conditions, data acquisition system including measurement cards enabling measurement of phase currents, voltages, torque, speed as well as the laboratory meters used for control purposes. The measuring system is shown in the Fig 1, while the rated data of the tested machine are presented in Table 1. On the other hand, Fig. 2 shows the selected results of measurements of the winding current in which the turn short-circuit occurred.

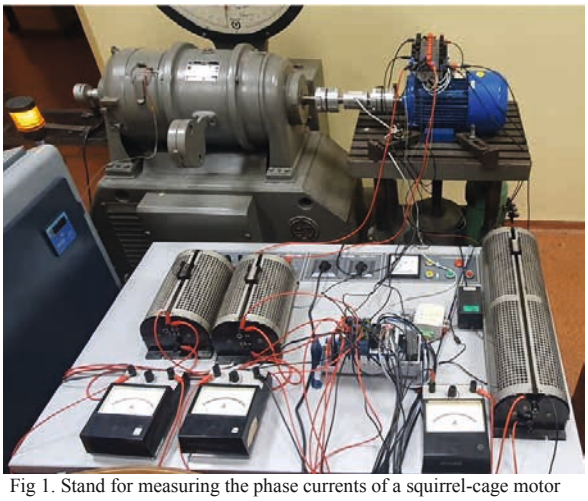

Fig 1. Stand for measuring the phase currents of a squirrel-cage motor

TABLE I. RATED PARAMETERS OF THE MOTOR

	Parameter	Rated Value
1	Power	3 kW
2	Current	6,3 A
3	Frequency	50 Hz
4	Voltage	400 V
5	Torque	19,56 Nm
6	Speed	1465 RPM

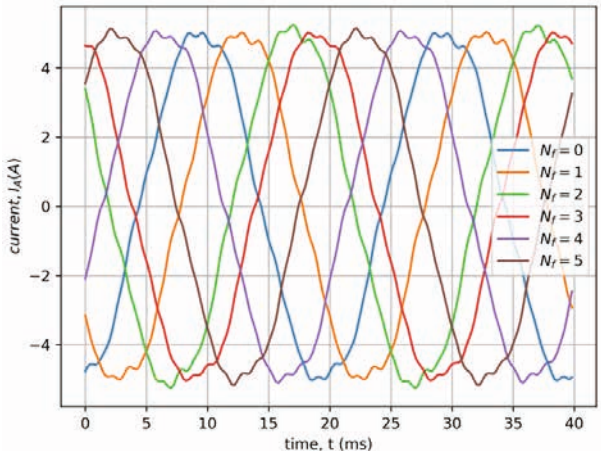

Fig 2. Current waveforms of a healthy and faulty machine at load torque T_L= 0 Nm

III. SELECTED RESULTS OF THE DIAGNOSTIC SIGNAL ANALYSIS

The obtained waveforms of phase currents were subjected to spectral analysis. The results of this analysis are shown in Fig. 3. On the other hand, Fig. 4 shows the graph of the maximum current value depending on the number of short circuits for selected values of the torque load. The comparison of the influence of 5 shorted turns on the current values in all phases depending on the torque is presented in Fig. 5.

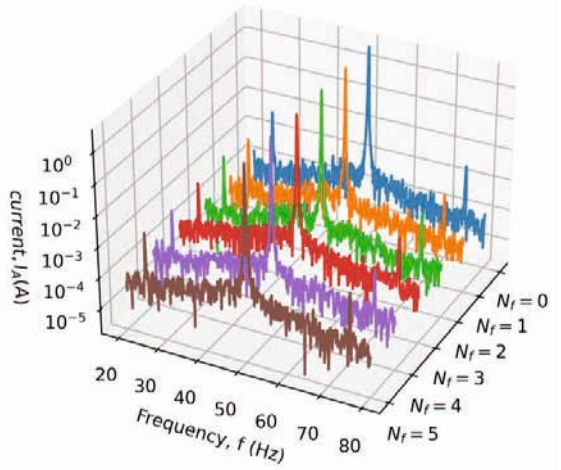

Fig 3. Spectral analysis of current a healthy and faulty machine at load torque $T_L = 0$ Nm

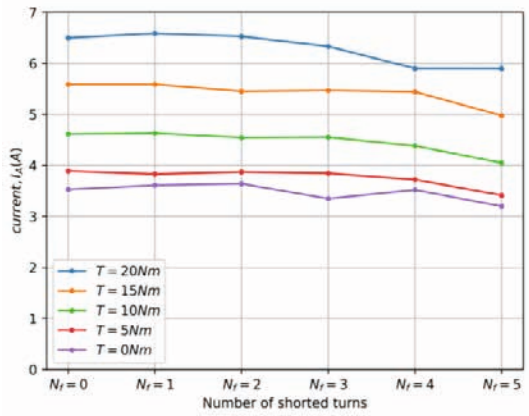

Fig 4. Current as a function of number shorted turns for a healthy and faulty machine

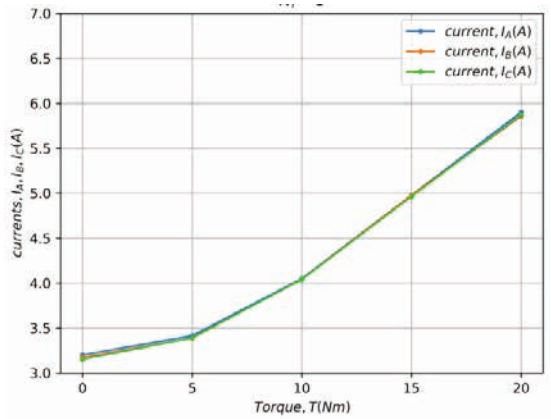

Fig 5. Currents as a function of torque for the number of shorted turns $N_f = 5$

IV. CONCLUSIONS

Detecting inter-turn faults at an early stage of their formation is a very important task. Thanks to effective methods of their detection, it is possible to plan the repair of the machine, prevent emergency shutdowns of the machine, etc. The purpose of the research was to present selected results of the spectral analysis of the stator current.

The measurements were carried out for a small number of shorted turns in one phase of the stator winding for the torque load in the range from the rated value to the no-load operation.

On the basis of the obtained results, it can be observed that in the case of a constant load torque, the value of the current in the damaged winding decreases with increasing the number of shorted turns. However, when comparing the current of a damaged winding with the currents of undamaged windings, it is difficult to conclude about the damage. Therefore, it is better to use machine learning methods to interpret the obtained measurement results.

REFERENCES

[1] *Elbouchikhi, E.; Amirat, Y.; Feld, G.; Benbouzid, M. "Generalized Likelihood Ratio Test Based Approach for Stator-Fault Detection in a PWM Inverter-Fed Induction Motor Drive", IEEE Trans. Ind. Electron. 2019, 66, 6343–6353, doi:10.1109/TIE.2018.2875665.*

[2] *Górny, K.; Kuwalek, P.; Pietrowski, W. "Increasing Electric Vehicles Reliability by Non-Invasive Diagnosis of Motor Winding Faults", Energies 2021, 14, 2510, doi:10.3390/en14092510.*

[3] *Ojaghi, M.; Mohammadi, M. "Unified Modeling Technique for Axially Uniform and Nonuniform Eccentricity Faults in Three-Phase Squirrel Cage Induction Motors", IEEE Trans. Ind. Electron.2018, 65, 5292–5301, doi:10.1109/TIE.2017.2760280.*

[4] *S. S. Babu and A. Sukesh, "Current Programmed Controlled DC-DC Converter for Emulating the Road Load in Six Phase Induction Motor Drive in Electric Vehicle", 2020 International Conference on Power Electronics and Renewable Energy Applications (PEREA), 2020, pp. 1-6, doi: 10.1109/PEREA51218.2020.9339779.*

[5] *M. Bagheri, E. Farjah and T. Ghanbari, "Selective Utilized Phase Number of Multi phase Induction Motors Strategy to Enhance Electric Vehicles' Drive Range", 2021 12th Power Electronics, Drive Systems, and Technologies Conference (PEDSTC), 2021, pp. 1-5, doi: 10.1109/PEDSTC52094.2021.9405866.*

[6] *J. M. Tabora et al., "Induction Motors Assessment: A Substitution Case Analysis", 2021 14th IEEE International Conference on Industry Applications (INDUSCON), 2021, pp. 783-789, doi: 10.1109/INDUSCON51756.2021.9529738.*

[7] *S. Rachev, D. Stefanov, L. Dimitrov and D. Koeva, "Evaluation of Electric Power Losses of an Induction Motor Driving a Compact Electric Vehicle at Change of Parameters and Loads", 2019 Electric Vehicles International Conference (EV), 2019, pp. 1-5, doi: 10.1109/EV.2019.8893057.*

[8]*Dhamal, S.S.; Bhatkar, M.V. "Modelling and Simulation of Three-Phase Induction Motor to Diagnose the Performance on Inter-Turn Short Circuit Fault in Stator Winding", In Proceedings of the 2018 International Conference on Computing, Power and Communication Technologies (GUCON), Greater Noida, India, 28–29 September 2018; pp. 1166–1172.*

[9] *Berzoy, A.; Mohamed, A.A.S.; Mohammed, O. "Impact of Inter-Turn Short-Circuit Location on Induction Machines Parameters Through FE Computations", IEEE Trans. Magn. 2017, 53, 1–4.*

ASYNCHRON MACHINE WITH POLE-CHANGING WINDING

Makhsud Bobojanov

Tashkent State Technical University named after Islam Karimov,
Department of Electrical Energy supply
University str.2, 100077, Tashkent, Uzbekistan, e-mail: mbobojanov@yahoo.com

Abstract **-** In this paper, the possibilities for constructing pole-changing windings with a ratio of poles 3:4 and improved electromagnetic properties are investigated. The results of experimental research work on two-speed machine with a new winding are presented, too.

I. Introduction

Two-speed electrical machines can be carried out both with two separate windings or with one pole-changing winding (PCW). Undoubtedly, the second kind of construction has a lot of advantages in view of the smaller slot area which is occupied with a winding that allows improved utilisation an active part of the electrical machine, to enhance power parameters, to simplify manufacturing and shorten repairing times.

Many scientists from different countries of the world were engaged with the problem of PCW development and as a result of these researches, a great number of schemes for pole-changing windings on different ratio of poles and phases has been developed.

However, the majority of these schemes have not found industrial application, since existing principles of PCW design do not currently allow the fabrication of a winding for a wide spectrum of ratios of numbers of poles and phases, that are coming nearer to manufacturing technologies of conventional windings of serial ac machines.

At the same time, PCWs should have a structure close to the structures of conventional windings with a width of the phase zone of 60 and 120 degree (2*m*-zone and *m*-zone windings). Here, the corner between the coils, belonging to different phases and laying in the next slots should be equal 60 degree ($\pi/3$) or 120 degree ($2\pi/3$), respectively. The deviation from these values will be defined as difference between the shear angle of conventional and new windings: $|\Delta\varphi| = |\varphi_{usual} - \varphi_{new}|$. Concerning the difference $\Delta\varphi$ between corners, it is better to take it in absolute values, since the deviation from normal shift to the left or right should be estimated equally.

II. New Method

The development of schemes for PCWs with a close structure to normal windings, i.e. with improved electromagnetic properties is possible, using the modernised method DSSF (discretely specified spatial function). This method has been developed by the chair "Electrical Energy Supply" of the Tashkent State Technical University [1,2,3].

On a basis of this method, the new principle for current or phase distributions of two simple lap windings of normal execution with the number of pole pairs p_1 and p_2 and phases m_1 and m_2 can be developed. They are simultaneously used in the process of winding design. Thus the winding scheme is not accepted as being ready and is formed in the process of construction, taking into account pictures of distribution of phase currents in slots of the machine for every pole.

III. Development of PCW using of new Method

One of the most common speed ratios in two-speed motors used on drives of mechanisms with a fan type of load is a ratio of 3:4.

At the same time, the first speed of 1000 rpm is the main one at which the electric machine will work in case of full loading of the mechanism, and the second speed (750 rpm) – auxiliary and is used to regulate performance for the responsible use of electricity and natural resources in underloading modes, and can also serve as the first stage in a step-by-step start-up.

With this in mind, a winding scheme of PCW for a ratio of poles 3:4 in the number of slots 72 was developed using a new method.

As a basic scheme for this PCW is suitable PPO scheme "three three-phase stars with additional branches", which is shown in Fig.1.

To receive accordance of the above-stated winding with the diagram shown in Fig.1, it is necessary to take out some coils in additional branches from the big pole side, removing two coils from the $2p_1$ pole side from each phase zone.

These coils are deduced in additional branches and, being redistributed on phases, contribute to build up a magnetic field of $2p_2$ pole [5].

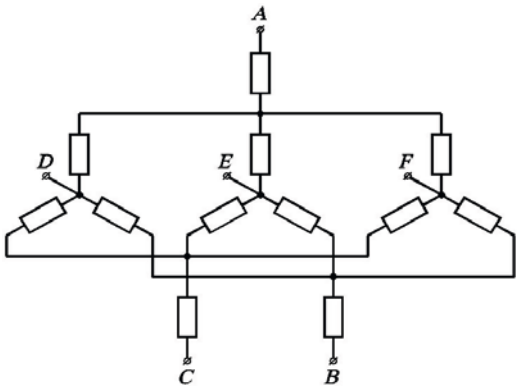

Fig.1. Bacis scheme "three three-phase stars with additional branches"

At the same time, the resulting (total) values of electromotive forces (EMF) should be equal to zero in an additional branch from the $2p_1$ pole side, and as a whole, they should have no influence on the functioning of the motor. Mutual compensation EMF of additional branches is carried out by a consistent connection of coils of additional branches and a circular distribution of the magnet core, while the relation to

each other on the corner of shift is equal to 120 electrical degrees and the winding in the magnetic field has a small number of poles.

For the coils of additional branches, it is expedient that the wire has a three times larger cross-section and accordingly a three times less number of turns than in other coils. In this case, practically full coordination of the magnetic inductance in the air gap is achieved by gaining the same performance:

$$\frac{w_1 \cdot \xi_1}{w_2 \cdot \xi_2} = \frac{p_1}{p_2} = \frac{3}{4} \qquad (1)$$

There might be a small deviation in the magnetic inductance, which can be provoked by various winding factors.

IV. Development and Test of New Machines

At the Tashkent State Technical University (TSTU), a sample model of the new two-speed machine was designed, having a PCW with a speed ratio of 1000/750 rpm. It is based on a magnetic core of a common 6-pole squirrel-cage motor AGM100L6 with an output power of 1.5 kW and a nominal speed of 925 rpm [5,7].

This machine was tested in the electromechanical laboratory of the chair "Electrical energy supply" at the TSTU. The results of experimental researches of the new machine in motor duty have shown the following: For 6 poles, the useful power of the new motor reaches 1200 W, efficiency and cos φ corresponding to this power amount to 76.9 % and 0.722, the nominal stator current is equal to 3.7 A, and the slip s is equal to 3.9 %.

For 8 poles, the value of useful power of the two-speed motor almost amounts to 982 W, the values for efficiency, the power factor and the slip corresponding to this power are equal to 73 %, 0.663 and 5.6 %.

The mechanical characteristics have a smooth appearance. The starting torque for 8 poles is higher and the starting current is less than for 6 poles, which allows using such motors for drives with heavy conditions during start-up and in areas with a weak power line. Due to a low starting current, the power line loading by a starting current will be the least.

The experimental tests in generator duty were carried out at direct connection of the two-speed induction machine to the network, and in an independent mode with connection to condenser batteries.

The shape of the voltage obtained is close to a sine wave, the harmonic content in a voltage curve changes minimally, i.e. the shape of the voltage is very close to a sine wave.

Analysing the received experimental test results, it is possible to say, that the new two-speed induction generator has weight-dimensional and power parameters similar to the parameters of the usual induction generators.

Thus, there is a real opportunity of creating new types of compact and reliable induction generators which can be used in wind installations or in separately standing hydrostations.

Reduction of weight in wind devices, except for consideration of economy of material means, would simplify processes of manufacturing, transportation and installation of wind installations.

As a whole, it can be noticed, that thanks to new PCWs with improved electromagnetic properties, it is possible to realise two-speed machines having weight-dimension and power parameters, as much as possible approached to parameters of normal one-speed electrical machines [6-10].

The use of such machines as motors allows to modernise existing electric drives with two-speed motors and to replace some conventional one-speed motors by two-speed pole-changing motors for the purpose of energy saving in small loading duty, in connection with technological or seasonal changes of loading and also to facilitate start-up processes for powerful motors.

V. Conclusion

1. The new method allows the design of PCWs of different ratios of pole pairs and phase numbers, whithout differing by their manufacturing and repairing technology from usual two-layer windings.
2. The offered PCWs do not have switching devices and possess improved electromagnetic characteristics and energy parameters in comparison with windings obtained by other methods.
3. Two-speed electrical machines with PCWs differ only marginally from usual serial one-speed induction machines and can perfectly substitute them with respect to energy saving.
4. Two-speed machines with pole-changing winding are adouble nonlinear system, which also needs to bestudied.

REFERENCES

[1] Karimov Kh, Bobojanov M (1996) New design of pole-changing windings for induction Motors for intense operating conditions. Electrical Technology pp.:19-28.

[2] Karimov Kh, Bobojanov M (2010) Methods of construction of windings for multi-speed electrical machines. "Fan va texnologiyalar markazi", Taschkent

[3] Kh.G. Karimov, Yu.A. Tupoguz, Method of constructing electrically aligned alternating current windings // Electricity. - Moscow, 1987. - No. 9 - pp. 29-38.

[4] Kh.G. Karimov, Methods of obtaining pole- changing windings for motors of variable electric drives of wide application // Uzbek journal "Problems of Informatics and Energy" - 1992, No. 3/4. - pp. 41-47.

[5] Bobojanov M. (2012) Electrical machines with pole-changing windings using with aim of energy and resource saving. "Fan va texnologiyalar markazi", Tashkent, p.179.

[6] M. Bobojanov, D. Rismuxamedov, F. Tuychiev, K. Shamsutdinov, K. Magdiev, Pole-changing motor for lift installation. E3S Web of Conferences 216, 01164 (2020) RSES 2020 doi.org/10.1051/e3sconf/202021601164.

[7] D.Rismuhamedov, F.Tuychiev, S.Rismuxamedov, Pole-changing windings for turbomechanism engines. IOP Conf. Series: Materials Science and Engineering, 2020, 883(1), 012140. doi:10.1088/1757-899X/883/1/012140.

[8] M.K.Bobojanov, D.A. Rismukhamedov, F.N. Tuychiev, H.F. Shamsutdinov and H.G. Magdiev, Construction and analysis of the pole-changing windings for the pole pairs ratio 5/6 by method discretely specified spatial function// International Journal of Advanced Science and Technology, Vol. 29, No. 11s (2020), pp. 1410-1415.

[9] D. Rismukhamedov, M. Bobojanov, F. Tuychiev, Kh. Shamsutdinov, Development and research of pole-changing winding for a close pole ratio// E3S Web of Conferences 264, 03057 (2021) CONMECHYDRO – 2021, doi.org/10.1051/e3sconf/202126403057.

[10] D.A. Rismukhamedov, H.G. Karimov, Zh.M. Mavlonov, F.N. Tuychiev, Pole-switchable winding for two-speed electric machine. Patent No. IAP 05385, 23.03.2017

INVESTIGATION OF THE INFLUENCE OF THE GAP WIDTH ON THE ACHIEVABLE TORQUE OF FLUX-SWITCHING MACHINES

[1]Lucas Steinacker, [1]Christian Kreischer, [2]Oliver Woywode

[1]Helmut-Schmidt-University, Chair of Electrical Machines and Drive Systems
Holstenhofweg 85, 22043 Hamburg, Germany, e-mail: lucas.steinacker@hsu-hh.de

[2]Philips Medical Systems DMC GmbH

***Abstract* - This paper investigates the influence of the air gap width on the achievable torque of a flux switching machine with permanent magnet excitation. For some applications, an increased air gap width of the electric machine is necessary. Therefore, the aim of this work is to investigate different air gap widths and to derive design guidelines for electrical machines with large air gaps. For the investigation, several geometries with different air gap widths are optimised. For the engineering of applications, it is essential to know the impact of the gap width.**

I. INTRODUCTION

Some applications require an increased air gap for electrical machines in order to maintain the necessary insulation clearances or to operate the rotor and stator in different media. Examples for this are pumps or X-ray tubes. From a structural point of view, larger gap widths are usually preferred, as these allow higher insulation voltages or thicker-walled vessels in the air gap. However, the achievable torque decreases with increasing gap width, so a compromise has to be found. Machines with an output up to 30 kW usually have air gap widths smaller than 1 mm. For larger machines, literature data are available for air gap widths up to 3mm. For air gap widths greater than 3 mm, there is almost no data available, especially for the FSPM.

In order to determine the optimal machine geometry for different air gap widths, a parameter variation was done and the optimum was selected manually.

Starting from a stator geometry optimised for an air gap of 3 mm width, the height of the rotor teeth is adjusted so that the desired air gap is achieved. The optimum rotor tooth width for the respective air gap widths is then determined by means of an evolutionary algorithm.

II. STATE OF THE ART

In [2] a comparative study between a flux switching machine (FSPM) and an interior permanent magnet machine (IPM) is presented. The design of the FSPM was optimized stepwise on the basis of a given IPM. The investigated FSPM has an air gap length of 0.73 mm. The outcome of this study is a more sinusoidal back-EMF, a smaller torque ripple and better mechanical integrity in the case of the FSPM. On the other side it has disadvantages due to a low magnet utilization and high material cost.

In [3] ferrite magnets are utilized rather than NeFeB magnets as in the other publications. The paper presents the general structure of the FSPM and presents a sizing study.

In [4] a technique is proposed to significantly reduce the cogging torque in FSPM with a negligible small reduction of the average torque. In this paper the form of the tooth tip was optimized. The investigated air gap lengths are 0.35 mm and 1 mm. 2D finite element analysis was applied to take the magnetic saturation into account. The optimized designs show a torque ripple to average torque ratio in the range from 6.8% to 13%.

III. OPTIMIZATION METHOD

The optimization bases on the method of differential evolutionary algorithm in combination with the simulation software FEMM which can be utilized via Matlab scripts.
A parameterizable geometry for a C-Core FSPM is scripted in Matlab. A C-Core machine is chosen because the copper content in the stator can be higher here, resulting in a higher power density. The publication by Linder and Hahn [1] was used for orientation. Fig. 1 shows the geometry generated by the script in FEMM.

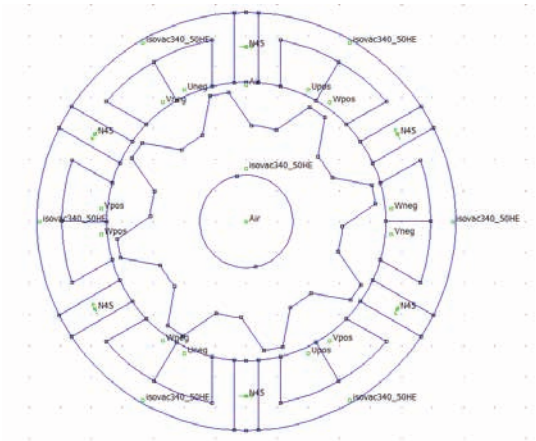

Fig.1. Generated FEMM model

A separate FEMM instance is opened for each simulation step (rotor rotation by 1 degree over one pole width) and assigned to a separate processor core. The number of parallel processes that can be realized depends on the available IT infrastructure. At the professorship for Electrical Machines and Drive Systems, the simultaneous use of 40 processor cores has proven to be stable. A separate geometry is generated for each simulation step, whereby these only differ in the rotor angle within one variant. For each simulation step, the torque acting on the rotor is evaluated and saved in a matrix.

Some of the parameters are set to a fix value. The outer diameter of the stator is 135 mm. The maximum rotor outer radius was set to 42 mm.

A value of 65% copper filling factor is assumed. Due to an active cooling of the outer stator region, a value of 10 A/mm² is assumed for the current density J.

The machine operates with a rotating three-phase system.

A value of 8mm is assumed for the yoke.

Due to the high operation frequencies of up to 2 kHz in the stator and rotor, the magnet width of 8mm is selected in order to achieve a large selection of potentially usable magnet sizes. The chosen value of 8 mm wide magnets represents a good compromise between torque and iron content. Furthermore, the shaft radius of 15 mm and the axial machine length of 40mm are freely chosen.

The inner and outer tooth width of the rotor teeth and that of the stator teeth are varied within this analysis. To reduce the number of variations, the stator tooth width (szb) is kept constant over the radius. The following tables provide an overview of the simulation parameters used.

For the manual optimization 1089 variants were simulated. The required simulation time was around 10 hours.

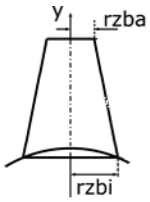

Fig.2. Definition of rotor parameters

IV. ANALYSIS RESULTS

In Fig. 3 results are shown for the simulated variants with 9mm air gap. The chosen optimum is indicated in orange.

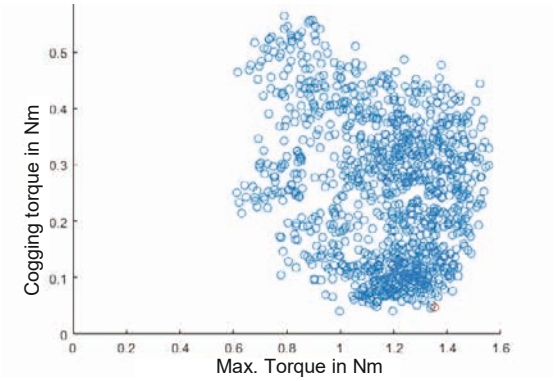

Fig.3. Results for variant calculation with 9mm air gap

Table I shows the chosen variants with low cogging torque and a high maximum torque.

As the air gap increases, the maximum torque and the cogging torque decrease.

To verify the results of the simulation, a C-Core FSPM is simulated in ANSYS. The same geometry parameters are used as in FEMM.

TABLE I
CHOSEN VARIANTS WITH VERY LOW COGGING TORQUE AND HIGH MAXIMUM TORQUE

Air gap (mm)	rzbi (mm)	rzba (mm)	szb (mm)	max. Torque (Nm)	Cogging torque (Nm)
3	8	3	11	4.97	0.33
6	2	3	12	2.46	0.07
9	2	3	13	1.35	0.05
12	3	3	14	0.79	0.03

In order to also be able to simulate different variants in ANSYS, the model is structured in a parameterizable manner. Due to the different procedures for creating the geometry, the resulting geometries differ slightly from each other. The average torque for the variant with 3mm air gap simulated with ANSYS is around 5Nm and is therefore around 0.3Nm above the torque determined with FEMM. In addition, the cogging torque is around 0.62 Nm. This means that the cogging torque is around 0.3 Nm higher in comparison. However, the shape of the two torque curves is very similar. The reason for the different simulation results can be the slightly different geometry. But the mesh also differs between the two simulations and cannot be exchanged between FEMM and ANSYS. There are also small differences in the simulation accuracy of the models. Overall, the ANSYS simulation can be used to verify the results generated with FEMM. The torque determined with FEMM is slightly smaller, so there is no risk that the torque will ultimately be too low. The detent torque is to be optimized in the further course.

V. CONCLUSION

In this publication, the rotor tooth geometry was optimized for FSPM with different gap widths. The focus here was on the lowest possible cogging torque with a high average torque. the respective optimum was selected manually on the basis of extensive variant calculations.

With increasing gap width, the achievable torque decreases significantly.

For machines with a small stator length a 3D simulation of the final design should be done in a final step.

REFERENCES

[1] A. Lindner and I. Hahn, "Design of an E-core flux-switching permanent magnet machine with large air-gap", 2015 IEEE International Electric Machines & Drives Conference (IEMDC), 2015.

[2] R. Cao, C. Mi and M. Cheng, "Quantitative Comparison of Flux-Switching Permanent-Magnet Motors With Interior Permanent Magnet Motor for EV, HEV, and PHEV Applications", in IEEE Transactions on Magnetics, vol. 48, no. 8, pp. 2374-2384, Aug. 2012.

[3] E. Hoang, H. Ben Ahmed, J. Lucidarme, "Switching flux permanent magnet polyphased synchronous machines", EPE 97, Trondheim, Norway, 1997.

[4] X. Zhu,W. Hua,Z. Wu, " Cogging torque minimisation in FSPM machines by right-angle-based tooth chamfering technique", IET Electric Power ApplicationsVolume 12, Issue 5 p. 627-634, 2018.

Acknowledgments: *This work has been supported by the Federal Ministry of Education and Research of Germany (BMBF grant FKZ 13GW0326E). The responsibility for the content of this paper lies with the authors.*

ELECTROMAGNETIC PROPERTIES OF AN INDUSTRIAL BILLET FURNACE WITH HIGH-TEMPERATURE SUPERCONDUCTOR COILS

Darian Wiegard, Sven Exnowski*

Bültmann GmbH
Hönnestraße 31, 58809 Neuenrade, Germany, e-mail: dw@bueltmann.com

*South Westphalia University of Applied Sciences, Department of Electrical Engineering and Information Technology
Haldener Straße 182, 58095 Hagen, Germany, e-mail: exnowski.sven@fh-swf.de

***Abstract* - In the context of this work, the technical aspects of a new type of billet furnace based on high-temperature superconductor technology were examined in detail. The focus of the analysis was essentially on the electromagnetic properties. For this work, a FEM model was developed with the help of which the electromagnetic field could be visualised and analysed to gain a deeper insight into the heating process.**

I. INTRODUCTION

The global striving for the optimum affects all areas. Hot forming technology, which is one of the most energy-intensive production processes, still has a lot of potential for improvement [1]. Currently, the German aluminium industry heats more than 800,000 tonnes of aluminium per year from approx. 20 °C to an average forming temperature of 480 °C. This corresponds to a supplied heat quantity of approx. 330 TJ per year, without taking losses into account. Since conventional induction heating only has an efficiency of about 50 %, a total of 184 GWh per year must be used for the continuous operation of the plants. Magnetic heaters based on high-temperature superconductors can achieve a significantly higher efficiency of about 70%. This can reduce the energy required from 184 GWh/a to 128 GWh/a, resulting in an energy saving of 56 GWh/a. The aim of this research is to develop a robust and low-maintenance magnetic heater with high-temperature superconductor coils that meets industrial requirements for efficiency and cost-effectiveness to be able to hold its own well on the global market in the future. Basically, a distinction is made between convective heating by means of fossil fuels and heating in magnetic fields [2], whereby the energy transition is increasingly moving away from the combustion of coal and gas. These points alone give an idea of where the trend is heading in the future.

II. TECHNICAL SPECIFICATIONS

The high-temperature superconducting billet furnace or induction heater is a new type of magnetic heater specially developed for non-magnetic materials that can achieve the special temperature profiles required for extrusion. The magnetic DC field generated in a high-temperature superconductor coil is guided via the yoke into two heating chambers. In the heating chambers, the workpiece rotates in the DC fields, whereby a voltage is induced by the change in flux density over time. The eddy currents flowing as a result run axially along the surface in the billets. At the end faces, they change the side of the billet to flow back on the opposite side. They thus form a circuit and the ohmic losses that occur cause the billet to heat up. These eddy currents flow on the surface due to the skin effect but also penetrate the material significantly due to the low rotational frequency. According to Lenz's law, the internal magnetic field built up by the eddy currents counteracts the cause, so that the magnetic fields in the gap and inside the billet are displaced and counteract the torque applied by the motor. The torque applied by the motor, in conjunction with the speed, contributes the energy for heating. Fig. 1 shows the overall construction of the system with the two heating chambers and the drive machines, and Fig. 2 visualises the three-dimensional CAD model for the necessary finite element calculations.

Fig.1. Construction of the system

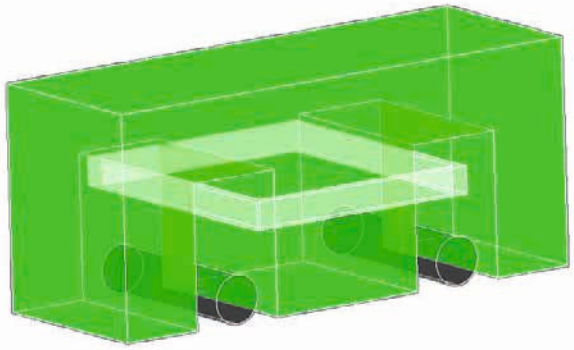

Fig. 2. Three-dimensional CAD model

In addition to specifying the rotation speed of the billets in the field, the so-called yoke adjustment can also be used to

influence the losses in the billets - and thus the heating. Here, the complete yoke is rotated around three different axes, which leads to the billets being moved out of the field or to a predefined angle to the field being set over the rotation axis. With the latter approach, a defined temperature profile can be set over the length of the billets. The operating current in the superconducting coil is continuously kept at a value of 505 A.

III. RESULTS

The heating of the billets in the billet furnace is achieved by rotating them around the cylinder axis. The resulting eddy currents heat the workpiece. In counteraction, the eddy currents have a braking effect on the rotation. Depending on the speed of rotation and the position of the billet in the field, eddy currents of different strengths occur. For example, peak current densities of up to 51 A/mm^2 are achieved with a full positioning of the billet in the field and a rotation speed of 1200 rpm, see Fig. 3.

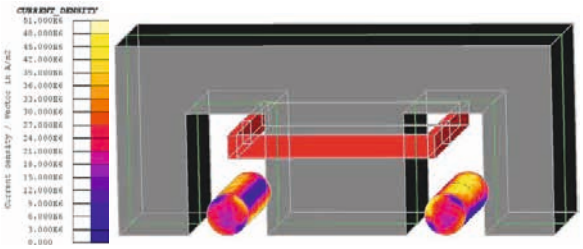

Fig. 3. Current density in the billets

Within the scope of this study, detailed observations were made on the power loss converted in the billet as a function of the speed and the position in the field. The speed was varied from 0 to the maximum possible speed of 1200 rpm and the billet was moved up to 250 mm out of the field. From this, a functional equation was determined for the power converted in the billet, the result of which is illustrated in Fig. 4. The power converted in the billet is shown as a function of the speed and the position of the billet in the field.

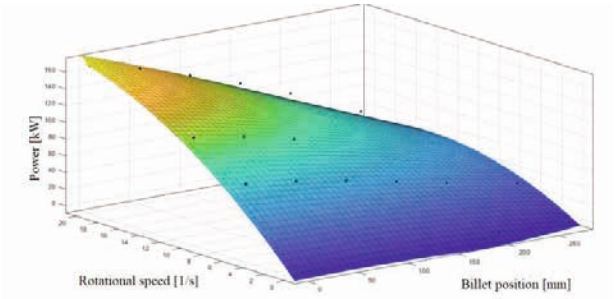

Fig. 4. Power converted in one billet

The results are also used to optimise the geometry of the yoke. Depending on the dimensions of the workpiece to be heated, pole shoes can be used in the lower area of the yoke, which have a significant influence on the converted power and thus on the duration of the heating. Assuming adiabatic heating of the billets, Fig. 5 shows a comparison of the heating durations without and with additional pole shoes.

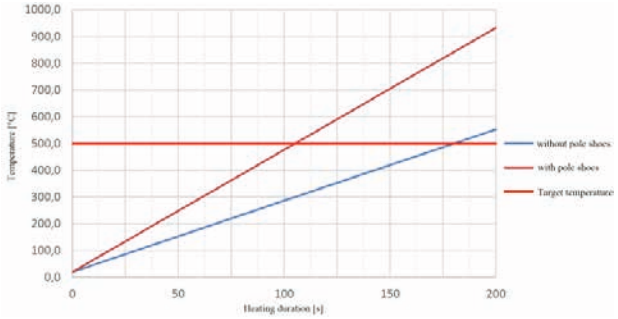

Fig. 5. Heating process without and with pole shoes

Another interesting parameter is the energy stored in the magnetic field. If, for example, an emergency shutdown occurs, the entire energy stored in the field must be dissipated almost instantaneously. The following applies to the energy E stored in the field:

$$E = \frac{1}{2} L I^2 \qquad (1)$$

The energy here corresponds to a value of around 270 kJ. The discharge resistance of the high-temperature superconductor coil must accordingly be dimensioned in such a way that it can absorb this energy completely, as it would otherwise be released in the form of heat in the superconductor and thus lead to irreparable damage.

IV. SUMMARY

The new industrial billet furnace with superconductor coils, which is specially designed for non-magnetic materials, is a complex machine with many special features. Although the process appears to be quite simple, it requires a great deal of sensitivity in its implementation, be it in the mechanical construction, the electrical and thermal design or the process programming and automation. The results presented here show that the system is ideally suited to meet the requirements of the industry. The calculation results provide valuable information for further geometry optimisation and the definition of an optimal heating process.

REFERENCES

[1] V. R. Gandhewar, S. V. Bansod, A. B. Borade, “Induction Furnace – A Review”, *International Journal of Engineering and Technology*, vol.3 (4), 2011.
[2] B. Sinafar, A. R. Ghiasi “Power and Frequency Control of Induction Furnace Using Fuzzy Logic Controller”, *arXiv*, 2015.

LIST OF AUTHORS

Duchesne, S.	Univ. Artois, Laboratoire Systèmes Electrotechniques et Environnement, Béthune, France	42
Ducreux, J.-P.	EDF R&D, ERMES, Palaiseau, France	10
Exnowski, S.	South Westphalia University of Applied Sciences Hagen, Department of Electrical Engineering and Information Technology, Germany	66
Frivaldsky, M.	University of Zilina, Faculty of electrical engineering and information technologies, Slovakia	16
Garmut, M.	University of Maribor, FERI, Institute of Power Engineering, Slovenia	12
Górny, K.	Poznan University of Technology, Institute of Industrial Electrical Engineering, Poland	60
Hameyer, K.	RWTH Aachen University, Institute of Electrical Machines (IEM), Germany	34
Hamler, A.	University of Maribor, Faculty of Electrical Engineering and Computer Science, Slovenia	44
Haussmann, N.	University of Wuppertal, Chair of Electromagnetic Theory, Germany	36
Henneron, T.	Univ. Lille, Arts et Metiers Institute of Technology, Centrale Lille, Junia, France	10
Hensel, H.	University of Wuppertal, Chair of Electromagnetic Theory, Germany	36
Hetmanczyk, J.	Faculty of Electrical Engineering, Silesian University of Technology, Gliwice, Poland	8
Hoffmann, K.	Helmut Schmidt University Hamburg, Germany	58
Hreczka, M.	Institute of Non-Ferrous Metals, Gliwice, Poland	8
Ispirli, M. M.	Marmara University, Electrical-Electronic Engineering Department, Maltepe, Turkey	32
Jędryczka, C.	Poznań University of Technology, Institute of Electrical Engineering and Electronics, Poland	46
Jesenik, M.	University of Maribor, Faculty of Electrical Engineering and Computer Science, Slovenia	44
Kalenderli, Ö.	Marmara University, Electrical-Electronic Engineering Department, Maltepe, Turkey	32
Kolano, R.	Institute of Non-Ferrous Metals, Gliwice, Poland	8
Kolano-Burian, A.	Institute of Non-Ferrous Metals, Gliwice, Poland	8

Simcak, M.	University of Zilina, Faculty of electrical engineering and information technologies, Slovakia	16
Slabu, I.	RWTH and University Hospital Aachen, Institute of Applied Medical Engineering, Germany	40
Späck-Leigsnering, Y.	Institut für Teilchenbeschleunigung und Elektromagnetische Felder und Graduate School Computational Engineering, Technische Universität Darmstadt, Germany	26
Steinacker, L.	Helmut-Schmidt-University Hamburg, Electrical Machines and Drive Systems	64
Stroka, S.	University of Wuppertal, Chair of Electromagnetic Theory, Germany	36
Taha, H.	Univ. Lille, Arts et Metiers Institute of Technology, Centrale Lille, Junia, France	10
Tang, Z.	Univ. Lille, Arts et Metiers Institute of Technology, Centrale Lille, Junia, France	10
Tolentino, G. C. A.	Univ. Artois, UR 4025, Laboratoire Systémes Électrotechniques et Environment (LSEE), Béthune, France	38
Trbušić, M.	University of Maribor, Faculty of Electrical Engineering and Computer Science, Slovenia	44
Vuckovic, A.	University of Nis, Faculty of Electronic Engineering, Department of Theoretical Electrical Engineering, Serbia	14
Wiegard, D.	Bültmann GmbH Neuenrade	66
Wojciechowski, R. M.	Poznań University of Technology, Institute of Electrical Engineering and Electronics, Poland	18
Woywode, O.	Philips Medical Systems DMC GmbH	64
Xiao, X.	RWTH Aachen University, Institute of Electrical Machines (IEM), Germany	34
Yazici, M.	Istanbul Technical University, Electrical Engineering Department, Turkey	32
Zagirnyak, M.	Kremenchuk Mykhailo Ostrohradskyi National University, Ukraine	22
Zang, M.	University of Wuppertal, Chair of Electromagnetic Theory, Germany	36
Zellmer, F.	French-German Research Institute Saint Louis, Electromagnetic Acceleration Group (ERG), France	20
Zito, G.	IFP Energies Nouvelles, Rueil-Malmaison, France	42